6-1-2016

Computational modeling of nanodrug-induced effects on cardiac electromechanics

Noha Mahmoud Shalaby

The American University in Cairo
School of Sciences and Engineering

COMPUTATIONAL MODELING OF NANODRUG-INDUCED EFFECTS ON CARDIAC ELECTROMECHANICS

A Thesis Submitted to

Program of Nanotechnology

in partial fulfillment of the requirements for
the degree of Master of Science

by Noha Shalaby

Under the supervision of: Dr. Khalil Elkhodary
Mechanical Engineering Department,
The American University in Cairo

Co-advisor: Dr. Nejib Zemzemi
Carmen Group, INRIA,
France

April/2016

ACKNOWLEDGEMENTS

I would like to acknowledge and thank the following people and organizations for making the completion of this project possible:

My advisor, Dr. Khalil Elkhodary, Assistant Professor of Mechanical Engineering at The American University in Cairo, who deserves my deepest gratitude for his invaluable help, unwavering support and constant motivation throughout this research work.

My co-advisor Dr. Nejib Zemzemi, member of the CARMEN team at INRIA, for his guidance with experience and extensive knowledge in the electrophysiology of the heart and for sharing with us the meshes used in this study.

EuropeAid for supporting this project under the Scheme 2 Innovation related action, grant (RDI2/S2/189).

The Magdi Yacoub Foundation, for their cooperation and for kindly sharing their knowledge and data.

My amazing family, for their patience, care and support.

And God, who made all things possible.

ABSTRACT

Noha Shalaby, The American University in Cairo
Advisor: Dr. Khalil ElKhodary, The American University in Cairo
Co-advisor: Dr. Nejib Zemzemi, Carmen Group, INRIA, France

Computational Modeling of Nanodrug-induced effect on Cardiac Electromechanics

This work generally aims to promote the use of computational models for predicting side effects of nanodrugs under development, as a means to speed up the cycle of drug development, with potential savings on testing, and reduction in the need for animal or human testing.
The specific objective of this thesis has been to accurately model a single ventricular contraction-relaxation cycle, and monitor the effects induced by nanodrugs on the electro-mechano-physiology of the left and right ventricles.
Nanodrug interaction with ion channels located on cardiac cell membranes, such as those for sodium, potassium and calcium, can distort an electrical wave propagating through the tissue and can affect cardiac macroscale functions. In this study, a material model after Holzapfel and Ogden was developed to account for the anisotropic hyperelastic behavior of cardiac tissue, which was implemented on the open source software library Chaste. A coupled drug-electro-mechano-physiological system was then set up, also on Chaste, where a nanodrug effect was introduced into the cellular structure (nanoscale) as an ion channel inhibitor, and its influence then solved for, with respect to resulting electro-mechanical ventricular behaviors. Using quantifiable biomarkers, these effects were compared to the literature and clinical data.
In this work we identified the following main results. Nanodrugs causing sodium channel blockage were found to produce the anticipated delays in electro-mechanics. Our study further predicted additional effects on LV twisting and LV & RV strain. On the other hand, nanodrugs causing potassium and calcium channel blockage revealed that cardiac mechanics is less responsive to mild alterations in electrophysiology, than electrophysiology is to ionic changes. Nonetheless, it is important to quantify these changes, as even a very small deviation from normal could accumulate over multiple cardiac cycles, and lead to adverse consequences on cardiac health in the long term.

TABLE OF CONTENTS

FIGURES

TABLES

ABBREVIATIONS AND ACRONYMS

AgNPs	Silver Nanoparticles
AP	Action Potential
Au1.4MS	Ultrasmall gold nanoparticles with 1.4 nm diameter
AuNPs	Gold Nanoparticles
Ca^{2+}	Calcium ion
Chaste	Cancer, Heart and Soft Tissue Environment
CuO	Copper Oxide
ECG	Electrocardiogram
EF	Ejection Fraction
FEM	Finite Element Method
IC_{50}	Half maximal inhibitory concentration
K^{+}	Potassium ion
LV	Left Ventricle
Na^{+}	Sodium ion
ODE	Ordinary Differential Equation
PDE	Partial Differential Equation
PK2	Second Piola-Kirchhoff stress
QT interval	Time interval between the Q wave and the T wave in the ECG
RV	Right Ventricle
TP06	TenTusscher and Panfilov human action potential model
ZnO	Zinc Oxide

LIST OF SYMBOLS

$[Ca^{2+}]$	Intracellular Calcium concentration
C	Right Cauchy-Green strain tensor
D_M	Monodomain conductance tensor
E	Green-Lagrange strain tensor
$\mathbf{f}_0$	Initial fiber direction
F	Deformation gradient tensor
h	Hours
I	Identity tensor
J	Jacobian / Determinant
m	Minutes
ms	Millisecond
mS/cm	Milli Siemens per centimeter
$\mathbf{s}_0$	Initial sheet direction
T	Second Piola-Kirchhoff stress
μA	Microampere

1) Introduction

The objective of this study is to model a single ventricular contraction-relaxation cycle and monitor the nanodrug-induced effect on their electro-mechano-physiology. The introduction is divided into subsections. First, the structure and function of the heart will be briefly stated to clarify the terminology that will be used throughout the thesis. Next, *nanomedicine* is introduced and how its use can affect the heart's functionality. After that, the motivation for testing nanoparticles for cardiotoxicity is justified by pointing to a number of studies that have thus far shown how certain nanoparticles under investigation for nanomedical research can cause unwanted biological interactions. The following section goes through how cardiotoxicity is quantified. Following that is a review of how research has been gauging the risk of drugs being cardiotoxic and the evolution into computational models for predicitive assessment. Next, the objectives of this thesis are stated in more detail and the software package chosen to build the problem is presented. Finally, there is a quick run through the organization of the thesis sections.

A) The Structure and Function of the Heart

The heart is a muscular electromechanical organ that pumps blood through the body. It consists of four chambers; two atria that act as reservoirs for two ventricles. The *endocardium* is the innermost lining of the chambers, the outer layer of the cardiac muscle is the *epicardium* with the *myocardium* cardiac tissue in between. The whole organ is covered with a layer called *pericardium*.[1]

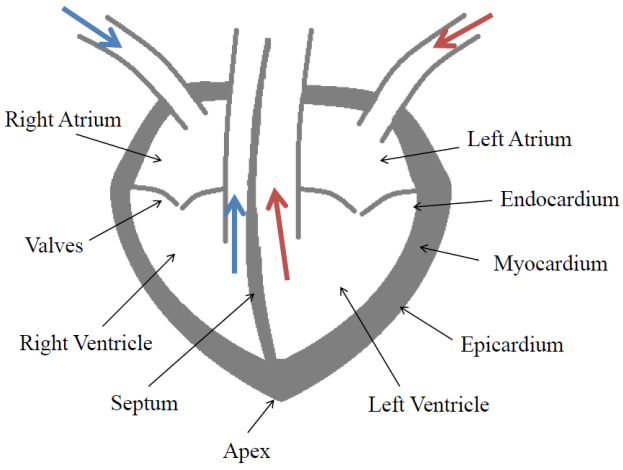

Figure 1: A schematic of the heart's structure. Red arrows indicate oxygenated blood and blue arrows indicate deoxygenated blood

A cluster of cells located above the right atrium, between the myocardium and the epicardium, called the sinoatrial (SA) node, acts as the heart's *pacemaker*,

producing regular electrical signals. The signal travels down the atria causing their contraction and depolarizes the atrioventricular (AV) node, which is another cell cluster in the center of the heart, between the atria and the ventricles. The electrical signal activated in the AV node travels down the wall of muscle between the right and left ventricles, known as the *septum*, through a bundle of fibers. At the *apex* of the heart, which is the very bottom of the heart, the bundle splits into left and right bundle branches that depolarize the left and right cardiac ventricles from the bottom-up, and cause their contraction[1], as indicated in the schematics of Figure 1.

At the start of a cardiac cycle, the ventricular chambers are in their relaxed phase, known as ventricular *diastole*. Blood low in oxygen, collected from the body, pours from the right atrium into the right ventricle. The ventricular contraction phase (*systole*) pumps blood from the right ventricle through the lungs, to obtain oxygen and to release carbon dioxide. Oxygenated blood returns to the left atrium and passes to the left ventricle (LV) in ventricular diastole. During systole, the oxygenated blood is pumped through the circulatory system to the rest of the body to circulate oxygen, nutrients, and hormones, and to collect waste. Blood flow direction is regulated by valves.[1]

Cardiac muscle cells are among a class known as *excitable cells*, i.e. they actively respond to an electrical stimulus that initiates the heartbeat, and causing the flow of ions. Specifically, sodium (Na^+), potassium (K^+) and calcium (Ca^{2+}) ions flow via cardiac cell trans-membrane ion channels.[2] In a resting heart, the difference in ion concentrations between the interior and exterior of the cardiac cell maintains a negative trans-membrane potential.[3] Chemicals or drugs interacting with these channels could cause partial or full ion flow inhibition, thus disturbing the electrophysiology and mechanical function of the heart.[3]

B) Nanomedicine and the Heart

Nanoparticles, which are nanomaterials of less than 100 nm in at least one dimension, are currently a very interesting area of scientific research. With their small size comes a multitude of highly desirable mechanical, optical, electrical and chemical properties, lending them well to being used in a variety of fields, including the biomedical field.[4] In particular, nanoparticles have great potential in

nanomedicine, which can be defined as the diagnosis, treatment or prevention of diseases using nanoscale tools, such as sensors, imaging agents, drug delivery systems or the drug product itself.[5] Of special interest is the use of nanoparticles as a drug delivery system (i.e. *nanocarriers*) to offer enhanced targeting of diseased tissues, increased permeability into diseased cells and controlled drug release.[6] However, nanoparticles at times become a likely cause for unwanted toxicological reactions.[4] Their high surface area to volume ratio increases their reactivity, which can cause undesired biological interactions, while their small size allows them to cross biological barriers with ease, risking their translocation to unplanned targets, e.g the heart.[7]

In fact, one of the foremost reasons for drug discontinuation at all phases of development is *cardiotoxicity*, in both cardiac and non-cardiac pharmaceuticals.[8] Cardiotoxicity can be defined as the occurrence of an electrophysiological dysfunction of the heart or a mechanical abnormality of cardiac muscular behavior as a result of the intake of a toxic matter.[9] Cardiovascular safety concerns have been responsible for almost 19% of drug withdrawals in the United States alone, over the past 40 years, and for 9% of worldwide withdrawals.[8]

Drug development and approval takes extensive time, money and effort, and is subject to high failure rates.[8] In fact, many promising drugs pass the initial cytotoxicity (toxic to regular cells) screening only to turn out to be highly cardiotoxic in preclinical trials.[10] Often, adverse drug effects on cardiac function appear only after completion of clinical trials, or after drug release in the market.[11] Detecting adverse drug interactions at such a late stage could undoubtedly cause a negative impact on a patient's health and general consumer confidence. Thus, there is increasing interest to better understand drug-induced cardiovascular complications, and to predict undesirable side effects at as early a stage in the drug development process as possible.

C) Nanoparticles Can Cause Cardiotoxicity

Various nanoparticles, used as nanocarriers, have been associated in the literature with cardiotoxicity. The most commonly used materials for inorganic nanoparticles are metals and their compounds,[6] where gold nanoparticles (AuNPs) are

one of the most extensively researched.[12] Their easy fabrication, tunable size and shape, and ready functionalization endow them with unique physical, chemical and optical properties that render them attractive candidates for many diagnostic and theraputic applications[13]. Such applications include their use as nanocarriers for target-specific delivery, and controlled and sustained release of drug molecules[14] . AuNPs are particularly attractive in cancer research,[15] especially ultrasmall AuNPs, as they are able to access cancer cell nuclei causing more damage.[16] Problems of toxicity appear according to the size of the AuNPs and their applied functional groups.[7] Several studies in the literature have identified that triphenylphosphine monosulfonate capped ultrasmall AuNPs of 1.4 nm diameters (Au1.4MS) are highly cardiotoxic, due to the irreversible binding and blockage of K^+ channels.[7,10,17]

Similarly, silver nanoparticles (AgNPs) also play a part in nanomedicine, in areas such as biosensing and wound dressing, for their antibacterial properties. Increasing concentration of AgNPs was tested for its effect on excitable cells, and concentrations of 10^{-5} g/ml or higher were shown to have an inhibitory effect on the Na^+ channel altering cellular electrophysiology.[18] Quantum Dots are another widely researched material on the nanoscale that exhibit excellent imaging and cell tracking properties, but have a negative effect on the Na^+ and Ca^{2+} channel functionality.[19] It has also been found that yttrium released from the growth catalyst of carbon nanotube has an inhibitory effect on Ca^{2+} channels.[20]

On the other hand, oxide nanoparticles are widely used in production leaving the end user of the product subject to accidental exposure to the nanoparticles through, for example, inhalation or skin contact.[21] Certain oxide nanoparticles have also been associated with cytotoxicity. Copper Oxide (CuO) nanoparticles have had their biological effects tested, where they were found to influence the K^+ current in cells, and in turn induce cell inactivation.[22] In a later study, CuO nanoparticles were found to also affect cellular Na^+ concentrations, due to their inhibitory effect on the Na^+ channels.[23] Furthermore, zinc oxide (ZnO) nanoparticles, have shown great potential for many applications, including electrical, environmental and, more recently, *biosensing*[24]. However, a concentration of 10^{-4} g/ml or more has been shown to activate Na^+ channels, thus affecting intracellular ion concentrations and cell excitability.[25] ZnO nanoparticles have also been found to have an inhibitory effect on Ca^{2+} entry into the cell.[21]

D) Typical Quantifiers of Cardiotoxicity

We note that most of nanomaterials have been tested for their effect on excitable neural cells, but not yet for their effect on excitable cardiac cells, which this study aims to do.

For an electrophysiological assessment of risk from new drugs, in general, the most commonly used biomarkers are based on *electrocardiogram* (ECG) measurements, especially the *QT interval* shown in Figure 2. ECG refers to electrode readings over time of the electrical activity of the heart, measured off the body surface. The QT interval is then the time interval between ventricular excitation (Q-wave) and end of repolarization (T-wave). The QT interval should be less than or equal to 400 ms for an average heart rate of 72 beats per minute.[26]

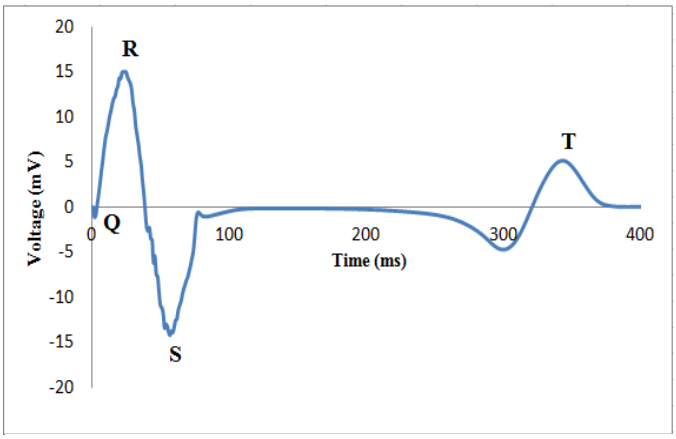

Figure 2: Pseudo ECG of normal heart

Drugs that prolong or shift the QT interval are considered especially risky and their development is generally discontinued.[27] This is because QT interval alteration induces disturbances in ventricular contraction patterns and blood *Ejection Fractions* (EF), both which compromise heart function. Ventricular strain and EF are thus the commonly observed biomarkers for drug development and identification of cardiotoxicity.[28]

E) Assessing the Risk of (Nano-) Drug Cardiotoxicity

Many experimental studies have been carried out to investigate cardiotoxicity induced from ion channel blockage. Preclinical studies of drug candidates have evolved over the years to include in-vitro assessment of their electrophysiological effect on cardiomyocytes, using a voltage-clamp or patch-clamp technique, which is a lab technique that measures electric current of single or multiple cell membrane ion channels.[10,29,30] Animal test subjects have also been used for in-vivo assessment of blood pressure, heart rate and ECG.[11,31] However, it has been determined that ion

channel currents in cardiomyocytes and their response to drugs is *species-specific*, and that even subtle changes in the elctrophysiological response to drugs between human and nonhuman cells can lead to different organ behaviors, due to the nonlinearity of the systems.[32]

To minimize potential risks from cardiotoxicity, much research has focused of recent on cardiac *modeling and simulation*, which are becoming an increasingly popular alternative to clinical and experimental (in-vitro) studies on the human heart. Modeling and simulation, or *in-silico* testing, promise a new *predictive* capability of biomarkers, for the rigorous evaluation of cardiotoxicity. In-silico methods are especially sought for, due to their greater safety and their ability to shed light on basic phenomena, which arise from the chemistry, biology, electrophysiology and mechanics of the heart, as well as their prediction of the overall behavior of the heart resulting from the multiscale and multiphysics interactions between such basic phenomena.[33] The Food and Drug Administration (FDA) listed the need for the development of mathematical and computational models as risk-benefit predictive tools for nanomedicine research.[34] Such models can however only be valuable, when their predictions compare closely to clinical data and biomarkers.

F) Computational Methods for Predictive Assessment

Toward achieving such close comparison between in-vivo and in-silico, a number of human *action potential models* have been put forward in the literature, each aiming to accurately describe the cycle of depolarization and repolarization of single human cardiac cells. Common to these models is that they lay coupled systems of ordinary differential equations (ODEs), for a description of ionic channels, exchangers and pumps, which collectively cause an action potential and regulate cellular sodium, potassium and calcium concentrations and fluxes.[35–37]

Such single cell models alone have been found inadequate for the prediction of clinically accurate ECG measurements. This is because single cell models necessarily ignore cardiac muscle fiber (myofiber) orientation, and surrounding tissue conductance, in generating and controlling the action potential. Multi-cell models have thus been developed, which combine single cell models as one, two or three

dimensional fibers and sheets, so as to better simulate the effect of single or multiple ion channel blocks.[38,39]

More recently, advanced models have been introduced to relate drug effects on cardiac electro-physiology. For instance, the *Cardiac Safety Simulator* (CSS) is a commercial tool, made available from Certara, developed for the testing of ion channel activity, with population variability which adds the likely impact of age, ethnicity and gender. It has been found to be able to predict the average effect of drugs on ECG and QT change. However, insufficient studies have been carried out using this tool to accurately confirm its predictive performance.[28,40,41] Nonetheless, evidence suggests cardiac electro-physiological models are rapidly advancing, having evolved from single cell predictions, to large scale models embedded in the torso, or even whole body geometries with body surface potentials, where single and multiple channel blocks can be recorded, analyzed and compared.[26,42–44]

Very recently, these sophisticated electro-physiological models have been integrated with cardiac mechanics simulators, in a *multiphysics* computational framework. This effort has been motivated by a need to investigate drug-induced changes to cardiac muscle intractability, which can have dangerous repercussions for patients. These changes are particularly difficult to measure clinically, making in-silico testing especially relevant. A few studies have been published, aiming to capture the multiscale interactions that characterize human cardiac electromechanics, from the drug and cell levels to the organ level.[33,45] Some studies are now focused on building a model for the complex fiber orientation of the cardiac walls, in order to properly capture that rotation and twist of the LV, and use the quantification and interpretation of LV torsion as a potential clinical tool.[46,47] In fact, LV twist is an important phenomenon that plays a significant role in blood ejection, and has, until recently, been somewhat neglected in the field of cardiac mechanics.[48] Fewer models have been built for both right and left ventricles.[49–51] Other models aim to develop the most accurate material law describing the material properties of cardiac tissue, both active and passive (with respect to electrical excitation), and to accurately predict corresponding stresses, strains and volume change from cardiac contraction.[52,53]

The largest ongoing cardiac electromechanical modeling project is the *Living Heart Project*[1]. It is a whole heart model developed by *Simulia*, through a consortium of researchers, clinicians and international industries, to create a unified foundation of cardiac electromechanical modeling and simulation. Their successful combination of accurate heart geometry and material properties in a multiscale/multiphysics framework is beginning to produce rather realistic predictions in normal and abnormal cardiac behavior.[50,51] This project, however, has not yet included drug interaction effects in their electrophysiological models.

In a parallel vein, the challenge of constructing patient-specific geometric models of the heart, capturing any abnormalities in form, from medical images and clinical data, is also receiving much research attention.[54,55] This effort aims to improve diagnosis of cardiac diseases, understand the variation of disease across patients, and predict patient-specific response to alternative interventions and medical treatments.

Such advances in electromechanical modeling are thus increasingly becoming an asset to the field of cardiac surgery, by reproducing the effects of heart diseases, simulating surgeries, predicting stress and strain, and quantifying changes in tissue material parameters.[56] Nevertheless, linking these state-of-the-art electromechanical methods, mostly available as research codes in testing, to drugs and the assessment of drug-safety has not taken root yet.[28] This points to a fertile ground for a computational multiphysics exploration, to lend its reliable hand to the safe advancement of nanomedicine.

G) Objectives of this Thesis

It is the objective of this work to link a detailed account of cardiac myofiber mechanics to drug-induced electro-mechano-physiology. Specifically, this study aims to setup a computational model of the human ventricles, which integrates nanoscale ionic flow from myocytic currents, exhibits the chemical interference of drugs and nano-drug carriers, captures resulting macroscale electrical propagation across ventricular tissue and resulting tissue contractile behavior, and accurately predicts associated electrical and mechanical biomarkers. In order to do so, a material law that

[1] http://www.3ds.com/products-services/simulia/solutions/life-sciences/the-living-heart-project

governs orientation-dependent tissue deformation is developed, based on the Holzapfel and Ogden[53] model, and is programmed in this study on the open source software package *Chaste*.

H) Why Chaste?

Chaste[2] (Cancer, Heart and Soft Tissue Environment) is a C++, object oriented library developed by the Computational Biology Group in the Department of Computer Science at the University of Oxford. It incorporates a broad set of numerical solvers and state-of-the-art algorithms for the service of biological modeling.[57,58] Its ionic and reaction-diffusion models have been verified and extensively used for cardiac electrophysiological modeling.[26,38,39,42,44,59] As it is an opensource software, its components are in a constant state of development.

The selected material law we developed on Chaste describes *hyperelastic* tissue properties that incorporate myofiber and sheet directions in the passive stress tensor. The material model is herein extended to implicit time integration by formulating an appropriate Jacobian (fourth-rank elasticity tensor). Coupling between the ionic, electrophysiological and mechanical models is then implemented on Chaste's multiphysics solver, as discussed in[57,60], to unveil new insights into the influence of drugs on the heart, ultimately advancing the field of computational nanomedicine.

I) Organization of the Thesis

This thesis is organized as follows. In section 2, we go through the methodology starting with the electrophysiological models in Chaste that are used in the simulations describing the electrical activity in a single cardiac cell and in the whole organ. After that we move on to the mechanical response discussing the fiber orientation in more detail as well as the active contraction model and passive material models of the mechanical behavior followed by how the coupling of these different components is carried out in Chaste. In section 3, the results of the electrophysiological simulations on an anatomically detailed ventricular mesh and the results of the coupled models are presented under normal conditions, under the effect

[2] http://www.cs.ox.ac.uk/chaste/

of a Na^+ channel blocker , under the effect of ultra-small gold nanoparticles on the K^+ channel and under the effect of a Ca^{2+} channel blocker. We conclude by summarizing our current findings and discussing potential future research directions in section 4.

2) Methodology

A) Electrophysiology

The flux of ions and associated electrical activity of an individual myocyte are essential phenomena to be modeled in cardiac electrophysiology; these may in general be well characterized by the various *cell models* available in literature.[35–37,61,62] Cell models must then be linked to governing differential equations that are responsible for the propagation of electrical activity across cardiac tissue.[63]

i) Cellular Level Models of Electrical Activity

Embedded protein structures on cell membranes form *channels*, *exchangers* and *pumps* responsible for the passage of ions in and out of the cell. Each protein structure is specific to one or two ions, responding to changes in potential across the cell membrane known as *trans-membrane potential*. Balancing the flow and intracellular concentrations of sodium (Na^+), potassium (K^+) and calcium (Ca^{2+}) ions is regulated by the opening and closing of these channels, and their generation of an *action potential.* The cardiac action potential is the sharp activation and the slow repolarization of the cardiac cell membrane.[63] The normal cycle shown in Figure 3 consists of 5 phases. The rapid depolarization (Phase 0), the early/rapid repolarization (Phase 1), the plateau (Phase 2), the late repolarization (Phase 3) and the resting phase (Phase 4).[2] In particular, in resting tissue the difference in intracellular and extracellular ionic concentrations amounts to a *negative* trans-membrane potential. Application of a significant electrical stimulus (e.g. incoming from pace-maker cells) then leads to the *depolarization* of the trans-membrane potential, by activating the Na^+ channels, which allow Na^+ into the cell. A positive trans-membrane potential, on the other hand, activates the Ca^{2+} and K^+ channels, which pass Ca^{2+} into the cell and K^+ out of the cell, resulting in a plateauing of the action potential. A rise in intracellular Ca^{2+} concentration instigates myocytic contraction, while the fall in intracellular K^+ concentration *repolarizes* the trans-membrane potential back to its negative resting value.[3]

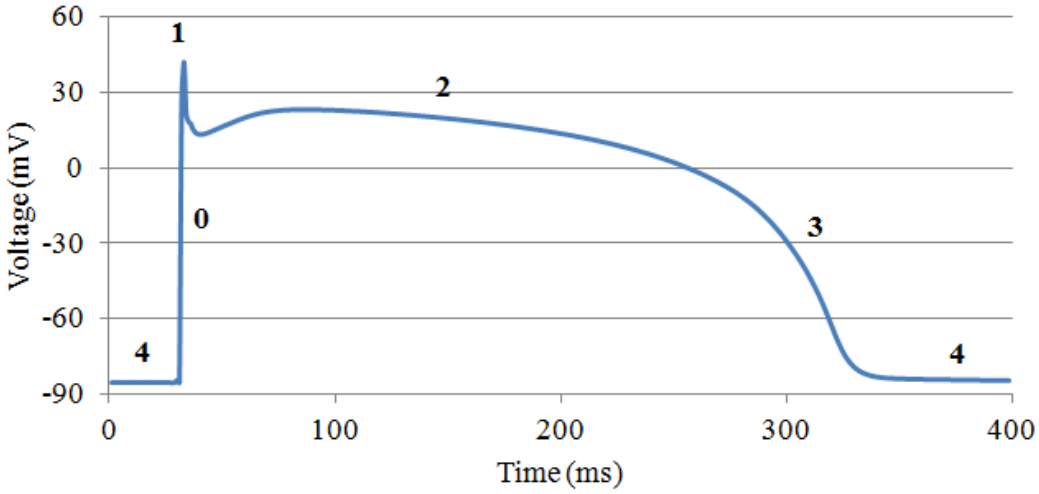

Figure 3: Normal action potential generated by membrane currents

Corresponding mathematical descriptions of this electrical activity in myocytes are all based on the work introduced by Hodgkin and Huxley[61] in the 1950s, where they described the trans-membrane potential and the cell membrane permeability, using just four ODEs. Models incorporating more cell properties and variables were later developed to increase their accuracy and strengthen their impact. In general, an ionic model needs to be detailed enough to model the properties of a single myocyte, but maintain computational efficiency, which is required for large scale simulations (of the whole heart).[63]

One of the most extensively used ionic models in literature[26,39,41,43,64,65] is the TenTusscher and Panfilov human action potential model.[35,66] It has been verified as an efficient model with reliable results based on experimental data.[36,67] It combines the 15 major ionic channels of the human ventricular cardiac myocyte, which consist of 10 transmembrane channels, 3 intracellular calcium channels, 1 sodium-potassium exchanger (I_{NaK}) and 1 sodium-calcium pump (I_{NaCa}) as shown in Figure 4. The cell membrane ionic currents modeled are the fast Na^+ current (I_{Na}), the L-type Ca^{2+} current (I_{caL}), the background Na^+ and Ca^{2+} leakage currents (I_{bNa}, I_{bCa}), the plateau Ca^{2+} and K^+ currents (I_{pCa}, I_{pK}), the slow delayed rectifier current (I_{Ks}), rapid delayed rectifier current (I_{Kr}), the inward rectifier K^+ current (I_{K1}) and the transient outward current (I_{to}). Differences in the I_{ks} and the I_{to} differentiate between epicardial, endocardial and mid-wall cells giving more accurate electrical conduction patterns.[35,63] The intracellular Ca^{2+} dynamics, which are a crucial link between the electrical activity and the cell contraction, are modeled by the leakage current from

the sarcoplasmic reticulum (I_{leak}), the calcium-induced Ca^{2+} release current (I_{rel}) and the pump current taking up Ca^{2+} into the sarcoplasmic reticulum (I_{up}).[35] We will use the TenTusscher and Panfilov human action potential model[66] (TP06) in the simulations of this study which is a reduced, more efficient version derived from the original model. The sum of all the trans-membrane ionic currents (I_{ion}) computed from TP06 will then be passed on to solve the electrophysiological field equation.

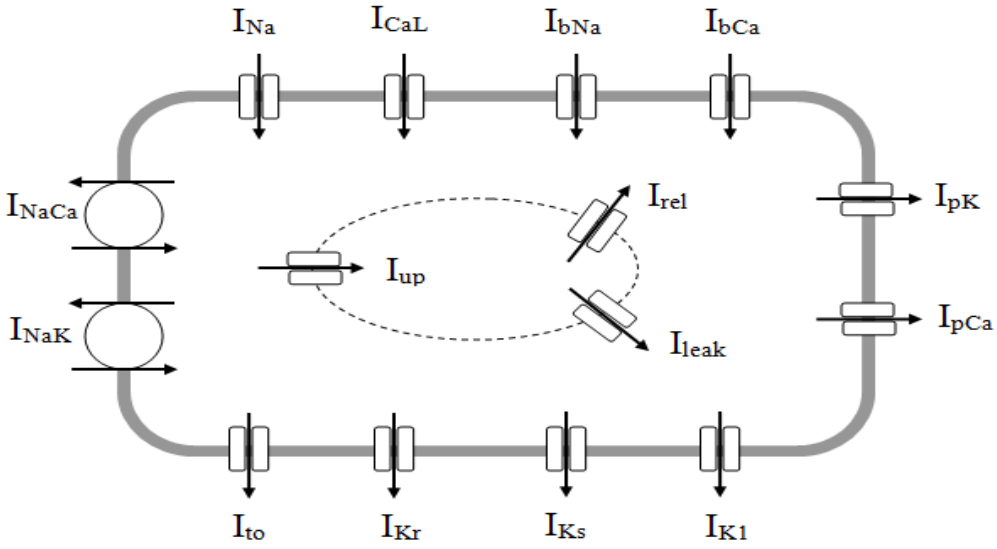

Figure 4: Diagram of ion movement across cardiac cell membrane and sarcoplasmic reticulum as described by the Ten Tusscher and Panfilov model

ii) Capturing Drug Interaction

There are two basic ways certain drug molecules can cause ionic flow inhibition by binding to ion channels. The first is when binding occurs near a channel's opening, which results in a physical barrier in the path of ionic flow. The second is a structural change induced in ion channel proteins due to drug binding, which also leads to ionic flow restriction.[3] In both cases a modification may be imparted to the TP06 action potential to model the inhibitory effect on Na^+ and K^+ channels of drugs in relation to dosage, half maximal inhibitory concentration (IC_{50}), and the Hill coefficient.[26] Hill coefficient is a quantification of the affinity of molecules or ions to bind to an already bound receptor. A value of more or less than one indicates that molecules or ions bound to a receptor increase or decrease, respectively, the likelihood of other molecules or ions to bind to that receptor, while having a Hill coefficient of one means the binding affinity is unaffected by the receptor's state, bound or unbound.[3] In particular, for the TP06 *ionic* model, the effect

of an investigated drug will be accounted for by altering ionic conductances (g) in the action potential model. The following formula is often used, with Hill coefficient n = 1;[42]

$$g_j([D]) = g_j\left(\frac{1}{1+\left(\frac{[D]}{IC_{50}}\right)^n}\right) \quad (2.1)$$

In equation (2.1) the degree of channel blockage is made dependent on the dosage [D] and IC_{50} of the drug. Index j represents the targeted ion channel.[26]

iii) Computational Implementation

CellML was used for the implementation of the aforementioned cell model. CellML is an XML-based language developed to provide a defined form and common basis for the development of mathematical cell models, with an aim to avoid errors that might arise in the exchange channel between researchers, during translation from one programming language to another, or from poor documentation. CellML facilitates the process of integrating selected cell models with different simulation environments. In particular, *PyCML* is a Python CellML tool integrated in *Chaste* that generates C++ classes from cardiac cell models linked to the electromechanical solver in *Chaste*.[68]

As the system of ODEs representing the cardiac cell has a '*stiff*' nature, due to the very fast upstroke of the action potential compared to the remaining simulation activities, a special solver is required.[68] CellML does not specify how the system of ODEs should be solved, leaving the choice to the users. In Chaste, the user could either code their own solvers or use PyCML to link to the CVODE library provided by Sundials3 to solve stiff ODE systems.[69]

iv) Tissue Level Models for Electrical Excitation and Recovery

Modeling the entire organ (the heart) cell by cell would be too computationally expensive, so a *continuum* approach is usually adopted to conduct simulations on this physiological scale. The idea is to avoid modeling the cellular scale explicitly by instead studying volume averaged quantities for cells, which are small enough compared to the overall heart domain, and may thus be treated as *points* in a continuum.[63] The corresponding continuum field equations which need to be

[3] https://computation.llnl.gov/casc/sundials/main.html

solved (numerically integrated) to simulate electrical excitation and recovery across ventricular tissue go by the name the *bidomain model*.[70]

The bidomain model was developed in the 1970s[71] and set the benchmark for studying electrophysiology of the heart. It divides the ventricular system into intracellular and extracellular domains. Cardiac cells are then assumed to be electrically connected to allow an electric stimulus to propagate throughout the heart via a *gap-junction* mechanism.[63]

We note that cardiac tissue is microstructured, so that corresponding electrical properties are in general anisotropic. The microstructure of ventricular tissue is discussed later in fuller detail. Nonetheless, we here must recognize that cardiac tissue is in fact organized in lateral sheets of fibers, and that tissue conductivity is higher when stimulated parallel to the alignment of its myocytes than when perpendicular. As such, at each given *point* three distinct values for conductivity are assumed; along the fibers (σ_f), along the sheets but perpendicular to the fibers (σ_s), and perpendicular to both the fiber and sheet directions (σ_n). This assumption gives rise to *two* diagonal conductivity tensors, one for intracellular conductance (D_i) and one for extracellular conductance (D_e), of the form:[63,70]

$$D_B = \begin{pmatrix} \sigma_f & 0 & 0 \\ 0 & \sigma_s & 0 \\ 0 & 0 & \sigma_n \end{pmatrix} \tag{2.2}$$

The bidomain model can be significantly simplified into the *monodomain model* by addressing the trans-membrane potential on the whole, and assuming anisotropy between intracellular and extracellular conductances are related by the equation $\sigma_e = \lambda\sigma_i$, where λ is a scalar constant. An *effective* conductivity for the monodomain equation thus substitutes the two conductivities of the bidomain equation as follows:

$$\sigma = \frac{\lambda}{1+\lambda}\sigma_i \tag{2.3}$$

Furthermore, extracellular applied current $I^e_{applied}$ from the bidomain equation also changes in the monodomain equation to[70]:

$$I^m_{applied} = I^e_{applied}\frac{\sigma^i_f}{\sigma^e_f+\sigma^i_f} \tag{2.4}$$

For the simulations herein, the monodomain equation was selected to provide the electrical image of cardiac tissue over a cardiac cycle. It is less computationally demanding than the bidomain model, and gives sufficiently accurate results with respect to electrical propagation and ionic channel blocking[72]. It is thus also assumed adequate to drive the associated cardiac mechanical cycle, which is the focus of the modeling effort developed in this work. The governing monodomain equation can be expressed as:

$$\chi \frac{\partial V_m}{\partial t} = \nabla . (D_M \nabla V_m) - \frac{\chi I_{ion} + I_{applied}}{C_m} \tag{2.5}$$

where χ is the surface-area-to-volume ratio, V_m is the trans-membrane voltage, t is the time, C_m is the capacitance across the membrane, D_M is the effective conductance tensor, $I_{applied}$ is the applied stimulus and I_{ion} is the value passed on from the TP06 ionic model, representing sum of all the trans-membrane ionic currents.[73]

v) Computational Implementation

As a parabolic partial differential equation (PDE), equation (2.5) requires a *simple linear parabolic solver*, which is predefined on Chaste. The solver employs the *finite element method* (FEM). The weak form of the monodomain equation is obtained by multiplying it by basis functions (ϕ), one for each node of the cardiac model, such that these functions satisfy the *Neumann boundary condition*, which for the case of the monodomain equation requires that their derivatives on the heart surface be *zero*, i.e. that no electrical flux out of the heart would be permitted.[74]

The discretized form of the problem becomes[74] *find* V^{m+1} where;

$$(\frac{\chi C}{\Delta t} M + K) V^{m+1} = \frac{\chi C}{\Delta t} M V^m - M F^m + c^{surf} \tag{2.6}$$

M is the mass matrix and K is the conductance dependent stiffness matrix given by;

$$M_{ij} = \int \phi_i \phi_j d^3x, K_{ij} = \int \nabla \phi_i . (\sigma \nabla \phi_j) d^3x \tag{2.7}$$

F^m is a vector of body current and stimuli for each node, and c^{surf} is a vector of surface stimuli for each node, which in this case is set to *zero*. These vectors are defined as follows:

$$F_i^m = (I_{applied})_i + \chi (I_{ion})_i, c_i^{surf} = \int_{\partial \Omega^{neu}} I^{surf} \phi_i dS \tag{2.8}$$

vi) Cell-level and Tissue-level Model Coupling

Once an external stimulus is applied to the cardiac tissue, the corresponding change in trans-membrane potential is communicated to the ionic model to solve for the associated ionic flow through the myocyte channels, pumps and exchangers. In the subsequent timesteps there is a back and forth relationship between the two models, as shown in Figure 5. The current (I_{ion}) calculated by the ionic model is fed to the monodomain reaction-diffusion equation, and the voltage and calcium concentration are updated as state variables which affect the ionic concentrations and current flow on the cellular level.

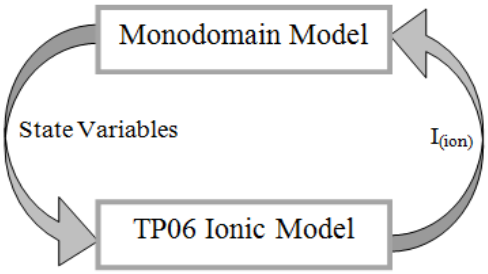

Figure 5: Excitation/Recovery model and ionic model coupling

B) Tissue Mechanics

i) Ventricular Fiber Structure & Relevance to Tissue Mechanics

Modeling living soft tissue mechanics is a topic of interest in much ongoing international research for a variety of reasons. If we confine our vision to *cardiac* research, however, a rigorous investigation of tissue mechanics holds promise in the prediction of ventricular volume changes between cardiac contraction and relaxation, a monitory of cardiac wall thickness variation, a quantification of ventricular twist and other related phenomena, all which will enable a deeper understanding of the different mechanisms that govern healthy and unhealthy heart functions.[75]

The heart however has a complex structure, composed of a multitude of fibers laid out along different orientations, which are crucial to defining electrical propagation[76] and mechanical contraction patterns.[49] Fiber distribution in general evolves smoothly from a right-handed helix structure in the sub-endocardium (Figure 6A) to a left-handed helical structure in the sub-epicardium (Figure 6B). The opposition in fiber direction between the sub-epicardium and the sub-endocardium compels them to contract in different directions. The larger radius of rotation of the outer epicardial layer dominates the direction of rotation causing twisting and shearing in the endocardium fibers where strain energy is thus stored and which, when released, serves for diastolic recoil.[77]

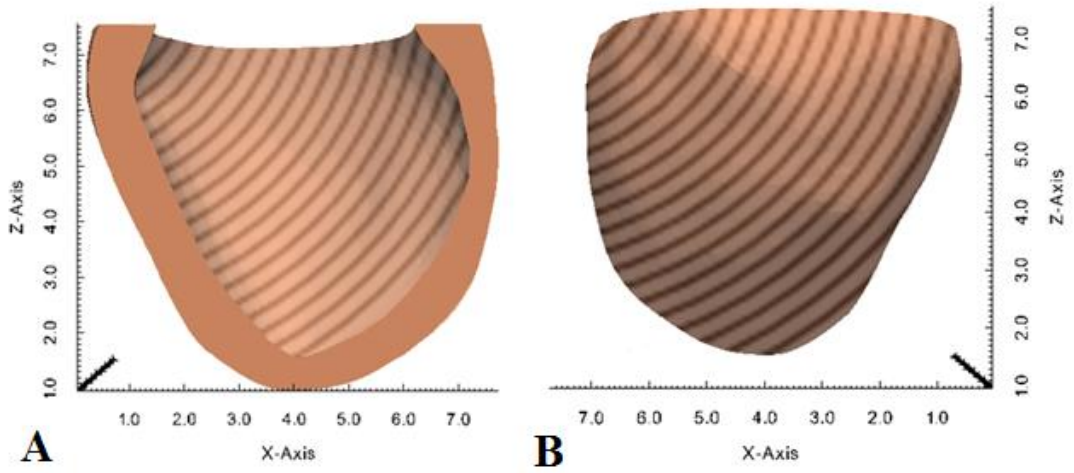

Figure 6: Fiber distribution evolve from a right-handed helical structure in the subendocardium (A) to a left-handed helical structure in the subepicardium (B)

Models of the ventricles that do not capture fiber direction have been found to lead to a misdistribution of stresses and strains, a decrease in cardiac energy efficiency, and an overall compromise in the accuracy of the predicted cardiac electromechanical phenomena.[75,77] Hence, proper myofiber orientation modeling has been a main focus of this work.

ii) Myofiber Orientation Modeling

The first to analyze the continuous change of fiber angle through the ventricular wall and the alterations in the fibers between systole and diastole were Streeter, et al.[78] Their model was built from histological datasets, relating well to the observed physiology of the ventricles, thus remains to date the most widely used fiber orientation model in cardiac simulations, in spite of its simple form.[79] In this model, a fiber axis is assigned to each element in the ventricular mesh by means of helix angle, α, according to the following[80];

$$\alpha = R * sign(1 - 2d) \, |1 - 2d|^{n} \tag{2.9}$$

where d is transmural depth and ranges from 0 to 1 from endocardium to epicardium; R is maximum absolute value of α depending on *heart region* (see next paragraph), such that α ranges between R at the epicardium and $-R$ at the endocardium of a given region, n modulates the transmural variation of α, e.g. linear (n=1) or cubic (n=3). The sheet axis is then defined as lying in the perpendicular plane to the fiber axis assigned, and the normal axis is finally defined as the direction orthogonal to them both.[53]

Simple *heart region* models merely differentiate between the left ventricle (LV) and the right ventricle (RV); while more accurate models could differentiate between 16 myocardial regions of the LV on one hand, and the apical, mid and basal regions of the RV on the other.[46]

In this work we thus employed the Streeter model to generate fiber orientations in the LV and RV, as indicated in Figure 7, having only distinguished two heart regions: the LV (Figure 7A, 7B) and RV (Figure 7C, 7D) for simplicity.

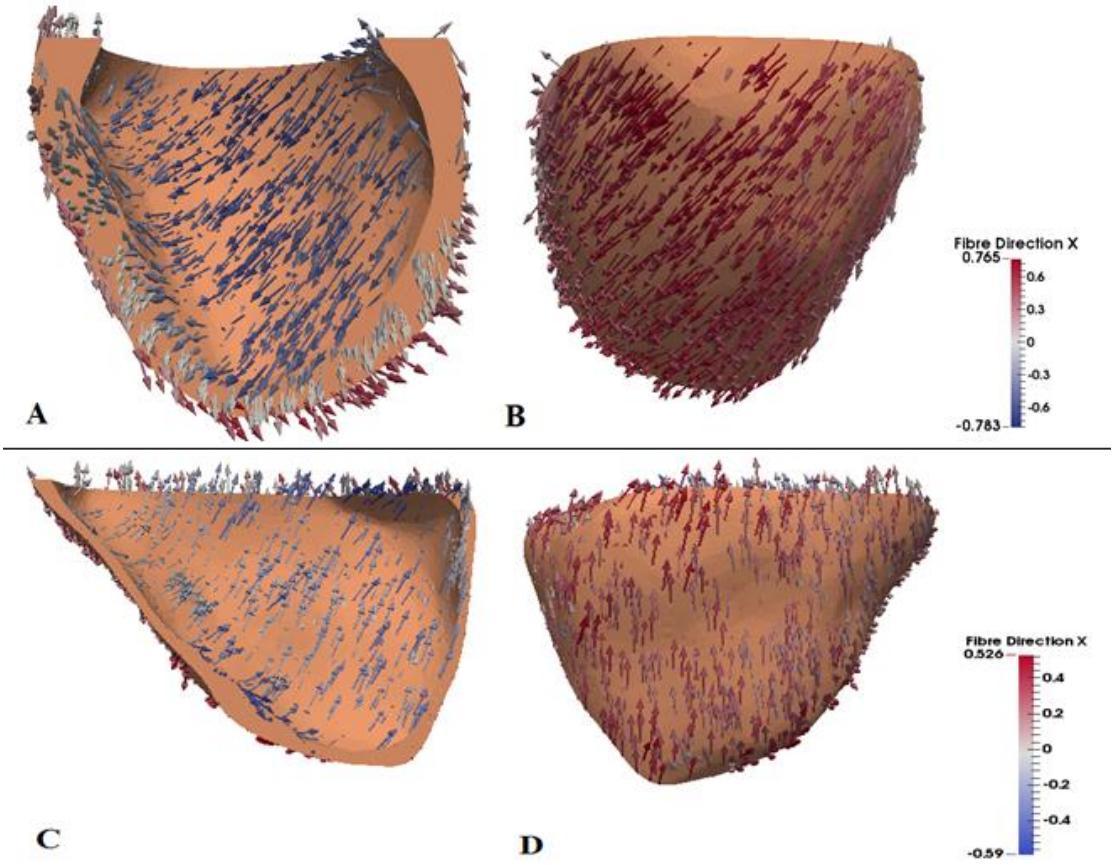

Figure 7: Fiber Orientations generated by the Streeter model. A) LV endocardium, B) LV epicardium, C) RV endocardium, D) RV epicardium

iii) The Mechanical Behavior of Myofibers

Modeling living soft tissue mechanics is a topic of interest to help monitor the change in cardiac wall thickness, myofiber structure and ventricular volume between contraction and relaxation to enable deeper understanding of the different mechanisms that govern behavior of healthy and unhealthy hearts.[75]

Two components are necessary to understand the electromechanical deformation of myofibers accurately. The first component is due to an *active* cellular contraction, i.e. an electrically excited contraction, which is responsible for the generation of an *active tension* in the myofibers. The second component, on the other hand, characterizes a *passive* myofiber mechanical response[60], i.e. one intrinsic to myofiber protein elasticity.

Under a microscope, a muscle fiber can be seen to be composed of many *myofibrils*, each consisting of repeated cylindrical sarcomeres, as summarized in

Figure 8A. A sarcomere is comprised of contractile proteins, bounded by Z-disks (Figure 8B). In particular, *thin filament proteins*, which are made up of helically arranged actin monomers (tropomyosin and troponin) project from both sides of Z-disks. Furthermore, myosin *thick filament proteins* are located in the middle of the sarcomere, connected to Z-disks via very thin, elastic filaments. In a contracting muscle fiber, an interaction between thick filament myosin and thin filament actin binding sites leads to a sliding action.[81]

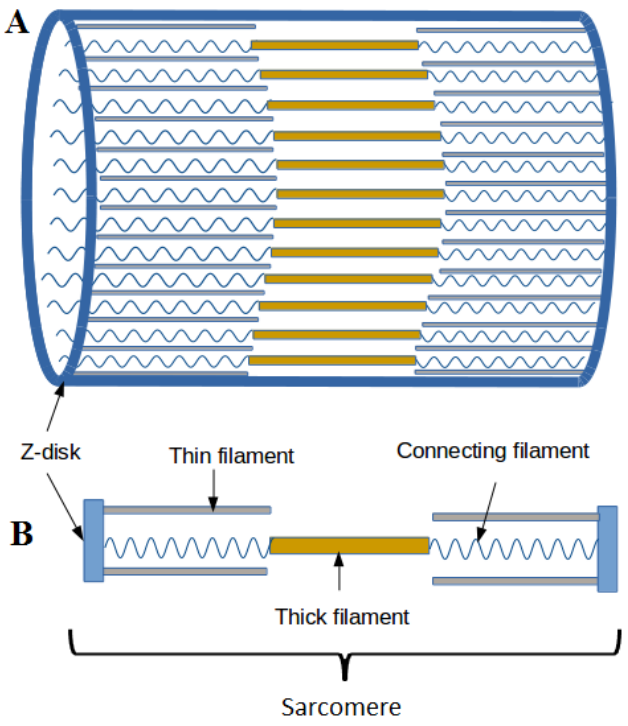

Figure 8: A) Muscle fibre composed of repeating myofibrils, B) Cylindrical Sarcomere

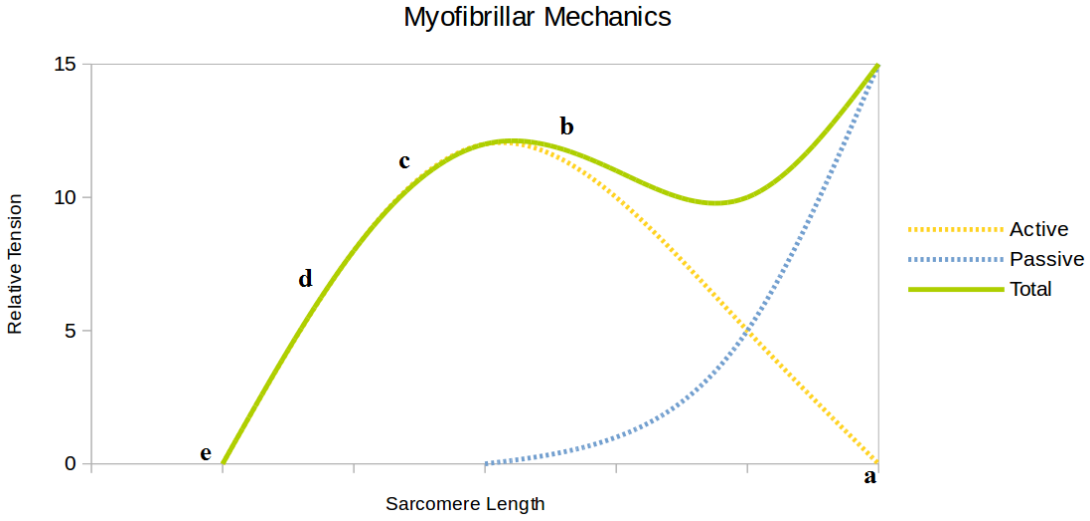

Figure 9: The total contractile force developed during contraction generated by the sum of active and passive forces

In particular, no active force is developed, as seen in the plot of the active force in Figure 9 at (a), when a sarcomere is stretched far enough to eliminate overlap between filaments (Figure 10a), as no cross bridges can form. Changes to the trans-

membrane potential lead to a release in Ca^{2+} ions, which bind to troponin on the thin filament changing its structure to expose binding sites and enable the formation of a cross bridge between myosin and actin (Figure 10b). These cross bridges cause shortening of the muscle fiber by exerting longitudinal forces that increasing the overlap between the thick and thin filaments, and result in increased active contracting force as seen at (b) in Figure 9. However, as the shortening progresses, thin filaments begin to overlap (Figure 10c, 10d) leading to a decrease in potential binding sites, and result in decreased active force (Figure 9 at (c) and (d)). When thin filaments hit the Z-disks they push back against the contractile force (Figure 10e), and net active force becomes zero (Figure 9 at (e)). Maximum force is thus produced when the sarcomere is at its intermediate length, while no force results at either extreme of length.[54]

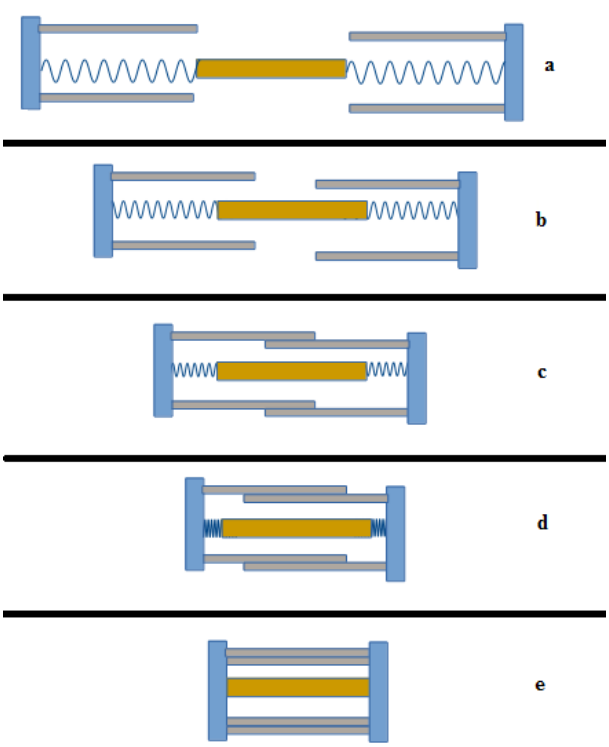

Figure 10: Different stages of stretch and compression of a sarcomere during contraction

On the other hand, a passive force is present in the muscle irrespective of electrical excitation due to the (nonlinear) elasticity of connecting filaments in myofibers and the collagen connective tissue surrounding each muscle fiber. The active force generated by the cross bridges is independent of the passive force from elasticity. Thus the active and passive stresses could be superimposed to get the total force curve, as shown in Figure 9.[54]

iv) Active Stress Model

To capture myofiber mechanical response to electrical excitation at each material point, a calculation of the active tensile (Cauchy) stress tensor, $\boldsymbol{\sigma}_a$, is needed. Active stress in general depends on the voltage, the intracellular calcium

concentration, [Ca^{2+}], fiber stretch state (λ), and sometimes the fiber stretch-rate $\dot{\lambda}$, in addition to any potential set of *state variables*.[60]

The *Kerckhoff model*[82] is a good example of a widely used active stress model. It contains no rate dependence, and no state variables, beyond [Ca^{2+}], contributing to desired model simplicity. It nonetheless adequately connects to cellular chemistry changes, through ionic flux interaction with [Ca^{2+}]. Due to our interest in nano-drug effects on cardiac electromechanics in this work, we are thus satisfied with this rather simple active stress model.

In this model, first a coefficient of the Cauchy active tension (σ_a) is computed, which depends functionally (say, function f_1) on the time elapsed since electrical depolarization (t_a), sarcomere length (l_s) and contractile length (l_c) as follows[82];

$$\sigma_a = f_1(t_a, l_s, l_c) = \frac{l_s}{l_{s0}} f_2(l_c) f_3(t_a, l_s)(l_s - l_c) E_a \tag{2.10}$$

where l_{s0} is the reference sarcomere length and E_a is the stiffness of the elastic filament. The function f_2 describes active stress dependency on contractile length, while the function f_3 describes active stress dependency on electrical activation time and the sarcomere length. These two functions are listed below:

$$f_2(l_c) = \begin{cases} T_0 \tanh^2(a_6(l_c - a_7)) & l_c < a_7 \\ 0 & l_c > a_7 \end{cases} \tag{2.11}$$

$$f_3(t_a, l_s) = \begin{cases} 0 & t_a < 0 \\ \tanh^2\left(\frac{t_{max} - t_a}{t_d}\right) \tanh^2\left(\frac{t_a}{t_r}\right) & 0 < t_a < t_{max} \\ 0 & t_a > t_{max} \end{cases} \tag{2.12}$$

where T_0, a_6 and a_7 are active material parameters and t_{max}, t_d and t_r are activation duration, activation decay time and activation rise time, respectively.

To construct the active stress tensor (σ_a), fiber direction vectors (***f***), defined in the current configuration, are introduced as dyadic bases for the coefficient computed in equation (2.2). This approach permits directional dependence of active stress in the model. Pulling back to the undeformed configuration, an active second Piola-Kirckhoff (*PK2*) stress tensor (T_{active}) can be recovered as follows[74],

$$T_{active} = \frac{J\sigma_a}{\lambda^2} \mathbf{f}_0 \otimes \mathbf{f}_0 \tag{2.13}$$

This pullback operation is necessary to satisfy force equilibrium in the finite element solver on Chaste, which uses a total Lagrangian formulation. In equation (2.13) above, J is the *determinant* of the deformation gradient $\mathbf{F}$, and $\mathbf{f}_0$ is the fiber orientation in the initial (reference) configuration.

v) Passive Stress Model

In this study, we will make the usual assumption that myofibers are *hyperelastic* and that their mechanical response is orientation dependent.[53,78] Viscoelastic and poroelastic effects are thus ignored, and heart muscle is treated as *incompressible*. An isochoric (constant volume) strain energy function may thus be introduced as follows[83];

$$W_{\text{iso}} = W(u) - p(I_3 - 1) \tag{2.14}$$

where $W(u)$ is a strain energy density function of displacement u, and describes mechanical response to both volumetric and isochoric deformation. p is a Lagrange multiplier, which may be interpreted as a hydrostatic pressure that penalizes volume change to enforce isochoric deformation.

a) Holzapfel and Ogden constitutive law

The strain energy function developed by Holzapfel and Ogden[53] is used in this study to compute the passive stress. It is an orthogonal components model based on shear and biaxial tests performed on a cube of passive myocardium tissue. It can capture the dissimilar responses of a material in the fiber *f*, sheet *s* and normal *n* directions. The strain energy function $W(u)$ is written as[53];

$$W(u) = \frac{a}{2b}\exp(b[I_1 - d]) + \sum_{i=f,s}\frac{a_i}{2b_i}\left[\exp\left(b_i\left[I_{4,i} - 1\right]^2\right) - 1\right] + \frac{a_{fs}}{2b_{fs}}\exp\left(b_{fs}I_{8,fs}^2 - 1\right) \tag{2.15}$$

where a, a_f, a_s, a_{fs}, b, b_f, b_s and b_{fs} are experimentally fitted parameters, and $d = 3$ in 3D models. I_1, I_4 and I_8 are invariants of the right Cauchy-Green strain ($\mathbf{C} = \mathbf{F}^T\mathbf{F}$), where $\mathbf{F} = \mathbf{F}(u)$ is the deformation gradient depending on displacements u of in the neighborhood of material point. I_1 is the sole isotropic term included in the energy

density function. I_1 = tr(**C**), with *tr* the trace operator, is thus considered to characterize the behavior of the non-muscular, non-collagenous part of the tissue.[53]

Anisotropy was introduced in equation (2.15) by specifying one or more directions of reference, *labeled i,* and defining the I_4 invariant in that direction according to $I_{4,i} = \mathrm{v}_i \mathbf{.C.} \mathrm{v}_i$, where $\mathbf{v}_i$ is a vector pointing in direction *i*. The exponential function applied to the fourth invariant in the fiber ($\mathrm{I}_{4,\mathrm{f}}$) and sheet directions ($\mathrm{I}_{4,\mathrm{s}}$) is a good reflection of the high stiffening and energy storage behaviors of muscle fibers and connecting collagen fibers, respectively. The other invariant included in the strain energy density function is the *coupling* invariant ($I_{8,fs} = \mathbf{f}_0 \cdot \mathbf{C} \cdot \mathbf{s}_0$), for a more detailed reflection of myofiber inter-dependency of orientations.

We here also note that the I_2 invariant was deemed unnecessary to include in equation (2.15) by Holzapfel and Ogden, while the I_3 invariant was omitted for incompressible tissue behavior, since $J = 1$ and $\mathrm{I}_3 = J^2 = 1$. The I_4 invariant of the normal direction ($\mathrm{I}_{4.\mathrm{n}}$) was further shown to be dependent on I_1, $I_{4,\mathrm{f}}$ and $I_{4,\mathrm{s}}$, so that its inclusion was also unnecessary. Finally, only a coupling of the fiber and sheet directions associated with fiber stretch was included in equation (2.15), as it was observed that the shear response in the planes containing the normal direction are relatively low, and rather similar for both the fiber-normal and sheet-normal planes.[53]

The derivative of the energy function *W* with respect to **C** is then taken to obtain the PK2 stress, **T**(**C**, *p*), yeilding[74];

$$T = 2\frac{\partial W(u)}{\partial C} - pC^{-1} \tag{2.16}$$

where,

$$\begin{aligned}\frac{\partial W(u)}{\partial C} = {} & \frac{a}{2}\exp(b(I_1 - 3))\mathbf{I} \\ & + a_f(I_{4,f} - 1)\exp(b_f(I_{4,f} - 1)^2)\mathbf{f_0}\otimes\mathbf{f_0} \\ & + a_s(I_{4,s} - 1)\exp(b_s(I_{4,s} - 1)^2)\mathbf{s_0}\otimes\mathbf{s_0} \\ & + a_{fs}I_{8,fs}\exp(b_{fs}I_{8,fs}^2 - 1)\mathbf{f_0}\otimes\mathbf{s_0}\end{aligned} \tag{2.17}$$

and **I** is the identity tensor.

When this model is setup for static finite element solvers, the corresponding Jacobian (iteration matrix) is needed[74], and we derive it in this work as follows;

$$\frac{1}{4}\frac{\partial \mathbf{T}}{\partial \mathbf{E}} = \frac{\partial \mathbf{T}}{\partial \mathbf{C}} = \frac{a}{2} b \exp\big(b(I_1 - 3)\big)\mathbf{I}\otimes\mathbf{I} + (2b_{\mathrm{f}}\big(I_{4,\mathrm{f}} - 1\big)^2 + 1)(a_{\mathrm{f}}\exp\,(b_{\mathrm{f}}\big(I_{4,\mathrm{f}} - 1\big)^2)(\mathbf{f_0}\otimes\mathbf{f_0}\otimes\mathbf{f_0}\otimes\mathbf{f_0}) + \Big(2b_{\mathrm{s}}\big(I_{4,\mathrm{s}} - 1\big)^2 + 1\Big)\Big(a_{\mathrm{s}}\exp\Big(b_{\mathrm{s}}\big(I_{4,\mathrm{s}} - 1\big)^2\Big)\Big)(\mathbf{s_0}\otimes\mathbf{s_0}\otimes\mathbf{s_0}\otimes\mathbf{s_0}) + \big(2b_{\mathrm{fs}}I_{8,\mathrm{fs}}^2 + 1\big)\big(a_{\mathrm{fs}}\exp\big(b_{\mathrm{fs}}I_{8,\mathrm{fs}}^2 - 1\big)\big)(\mathbf{f_0}\otimes\mathbf{s_0}\otimes\mathbf{f_0}\otimes\mathbf{s_0}) + p\mathbf{C}^{-1}\otimes\mathbf{C}^{-1} \tag{2.18}$$

Where **E** is the Green-Lagrange strain tensor, and is the strain measure of choice in Chaste, which employs the total Lagrangian formulation, wherein **E** is energetically conjugate to PK2.

This Holzapfel and Ogden can be reduced to a transversly isotropic model by reducing the parameters to only 4 parameters; a, b, a_{f} and b_{f}, which were shown to still fit data sets on cardiac mechanics very well. Indeed, in this study, these four material parameters were used (setting all others to zero) based on one of the most recent studies by Baillargeon et al.[51], which showed improved mechanical predictions on blood ejection fractions, than competing models with all 8 parameters.[50,83]

b) Pole-Zero constitutive law

Nash and Hunter[52] proposed a transversly isotropic material law based on biaxial tests performed on thin sections of passive myocardium tissue. The strain energy function is given as follow;

$$W(u) = k_{11}\frac{E_{11}^2}{|a_{11}-E_{11}|^{b_{11}}} + k_{22}\frac{E_{22}^2}{|a_{22}-E_{22}|^{b_{22}}} + k_{33}\frac{E_{33}^2}{|a_{33}-E_{33}|^{b_{33}}} + k_{12}\frac{E_{12}^2}{|a_{12}-E_{12}|^{b_{12}}} + k_{13}\frac{E_{13}^2}{|a_{13}-E_{13}|^{b_{13}}} + k_{23}\frac{E_{23}^2}{|a_{23}-E_{23}|^{b_{23}}} \tag{2.19}$$

where the k's, a's and b's are the material parameters and the **E** is the Green-Lagrange strain tensor (**E** = (**C** – **I**) / 2)) where **C** is the right Cauchy-Green strain and **I** is the identity tensor.

This constitutive model is already developed on Chaste, but it has not been chosen in this study to examine nanodrug effects as it has been found to give weak results in terms of ventricular volume change and ejection fraction as shown later on

in the thesis. Also, unlike the Holzapfel and Ogden model, it is limited to transverse isotropy and cannot model orthotropy.[53] The biggest problem, however, with this model is the fact that it needs 18 material parameters. Having that many lineary dependent parameters makes them difficult to identify[84] and sensitive to small changes in the data.[53]

c) Mooney-Rivlin constitutive law

The Mooney-Rivlin material law was derived from the work of Mooney[85] and Rivlin[86] in large elastic deformations in rubber-like isotropic materials. The strain energy function is given as;

$$W(u) = c_1 (I_1 - 3) + c_2 (I_2 - 3) \quad (2.20)$$

where I_1 and I_2 are the invariants of the right Cauchy-Green strain ($\mathbf{C} = \mathbf{F}^T\mathbf{F}$), where $\mathbf{F} = \mathbf{F}(u)$ is the deformation gradient depending on displacements u of in the neighborhood of material point. $I_1 = \mathrm{tr}(\mathbf{C})$, with *tr* the trace operator, $I_2 = \frac{1}{2}[(\mathrm{tr}(\mathbf{C}))^2 - \mathrm{tr}(\mathbf{C}^2)]$. c_1 and c_2 are the material parameters.

This material law is already developed on Chaste, but, as shown later, it gives weaker mechanical behavior compared to clinical data and compared to the other two constitutive laws investigated in this thesis. Its problem lies in the fact that it assumes the material behaves identically in all directions and does not take into account the fiber or sheet directions which is not the behavior of the cardiac tissue.[87] Hence, this material law was not used in this study to investigate the effect of nanodrugs on the cardiac mechanical deformation.

C) Electromechanical

i) Coupling Summary

Multiscale electromechanical modeling (itself multiphysics) is required in this work, since coupling appears between different length and time scales of our model ranging from molecular myofilaments (length ≈ 1.5-3.5 μm) to the organ level (volume ≈ 280 cm^3), and from rapid changes in ionic fluxes to the much slower muscle contraction. In summary, ionic models are first solved at the subcellular level, then ion concentrations are fed into the reaction-diffusion electrophysiological equation to study signal propagation across the organ, and into the active stress model to predict resulting mechanical deformation due to myofilament Ca^{2+} based activation. This is followed by passive tissue mechanics solving, which updates the electrical model with fiber and sheet orientations and the stretch-activated ionic channels. Clearly then all levels have a direct effect on each other via parameter passing, as summarized in Figure 11.

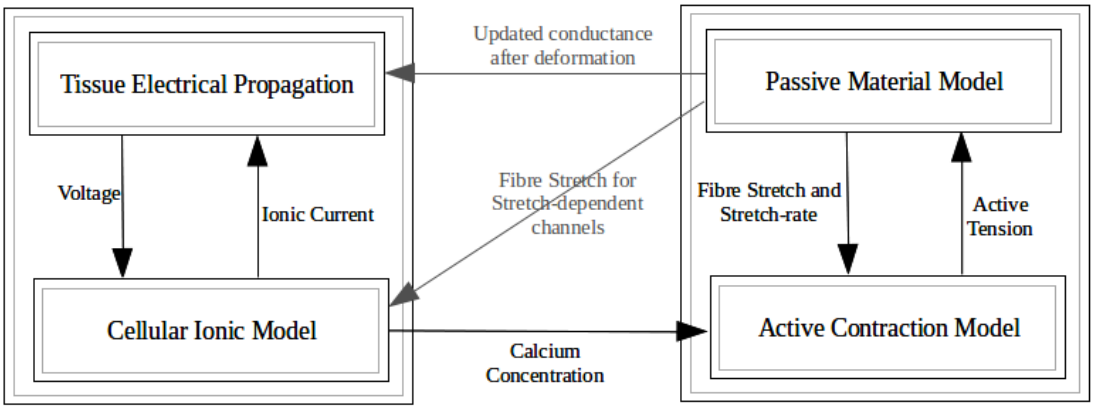

Figure 11: Components of the cardiac electromechanical model

However, the feedback of the mechanical deformation on the electrical conductance was not accounted for in this work since it is very computationally expensive to apply on big meshes such as the one used here. It would be quite interesting to see the feedback effect and compare with and without it on a more optimized tissue mechanics solver. The feedback to the ionic model was also removed since implementing how the stretch affects the stretch-dependent ion channels is outside the scope of this work.

ii) Stress Model Implementation on Chaste

When solving tissue deformation, at each instant inertial effects are neglected and the tissue is assumed to be in equilibrium. The weak form of the equilibrium equations needed to get the deformed configuration in the incompressible case using the finite element methods are as follows[74];

$$\int_{\Omega_0} \boldsymbol{T} \frac{\partial x_i}{\partial X_M} \frac{\partial(\delta x_i)}{\partial X_M} dV_0 - \int_{\Omega_0} \rho_0 b_i \delta x_i dV_0 - \int_{\partial\Omega_0^{trac}} s_i \delta x_i dS_0 = 0 \qquad \forall \delta x \in V_0 \tag{2.21}$$

$$\int_{\Omega_0} \delta p(det\boldsymbol{F} - 1) dV_0 = 0 \qquad \forall \delta p \in W \tag{2.22}$$

where $\mathbf{T} = \mathbf{T}_{active} + \mathbf{T}_{passive}$, V_0 is the subspace of deformations and W is the subspace of pressures, ρ_0 is the density, b is the body force per unit mass and s is the surface force. Equation (2.22) is the incompressibility constraint. Since gravity is neglected and there are no applied forces, the last 2 terms of equation (2.21) are zero giving the equilibrium equations for the incompressible volume the following form:

$$\frac{\partial}{\partial X_M}(\boldsymbol{T}(x,p)\boldsymbol{F}(x)) = 0 \tag{2.23}$$

$$det\mathbf{F} = 1 \tag{2.24}$$

Mechanical deformation is solved for on a quadratic mesh where quadratic interpolation is used for solving the displacement over N nodes and linear interpolation is used for solving the pressure over M nodes making the overall number of unknowns in the 3D mesh $3N + M$.

3) Results and Discussion

A) Problem Setup

The geometrical model used in this work is derived from CT data of the human ventricular chambers.[76,88] The mesh is confined to the left and right ventricles only and meshed into 238,382 elements. Since the electrical and mechanical meshes have different requirements regarding element type and element size, different computational meshes are used for each. The electric mesh is a linear tetrahedral mesh composed of 49,658 nodes. On the other hand, the mechanics mesh is a quadratic mesh with 354,107 nodes, to avoid pressure instabilities.[89] Both meshes are generated using *Chaste.*

The simulations were run on an AMD Opteron server with 256 GB of memory on an Ubuntu 14.04 operating system.

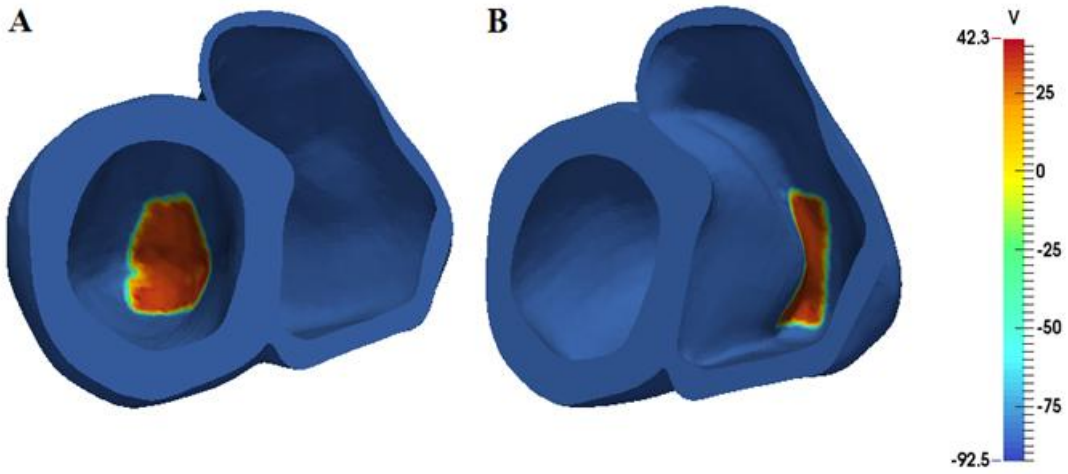

Figure 12: Basal view of ventricular model at time 1 ms highlighting the area of applied stimulus on the endocardium in A) the left ventricle and B) the right ventricle

Ventricular tissue was stimulated by -10,000 μA for 1 ms in the endocardium. Figure 12 highlights the locations where the stimulus was applied in the left (A) and right (B) ventricle endocardia. The monodomain reaction-diffusion equation was then solved in our simulations for 400 ms, to ensure complete activation and repolarization of the ventricles. The corresponding PDE solver on Chaste was called with a time step of 0.05 ms, Electrical conductivity along the fiber direction was set to 1 mS/cm and 0.3 mS/cm along the sheet and normal directions. and a surface area to volume ratio

was 200. For the cell model, the ordinary differential equation (ODE) time step was taken as 0.01 ms.

Dirichlet boundary conditions were prescribed for our mechanics model, where the nodes at the very bottom of the left ventricular apex (marked in yellow on Figure 13) were fixed in space in all 3 directions, leaving the remainder of the mesh to deform freely. As mentioned earlier, Kerckhoff's contraction model is used to calculate the active tension; its solver was called with a time step of 0.01 ms. Equations of equilibrium were then set to solve once every 10 ms.

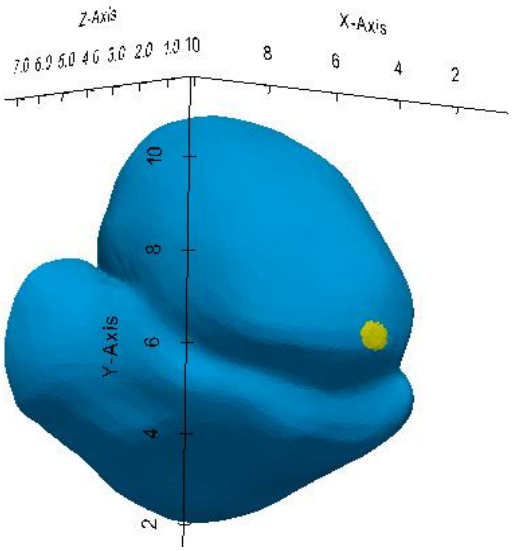

Figure 13: Dirichlet boundary conditions. Nodes at (z < 0.3) marked yellow are fixed in x, y, and z directions

The Streeter fiber class on Chaste was used to generate the fiber, sheet and normal directions at each element in the mesh (cell-centered). The vectors defining the fiber and sheet directions are shown in Figure 14 A and B, respectively. This fiber definition is necessary for both the electrical conduction and mechanical deformation.

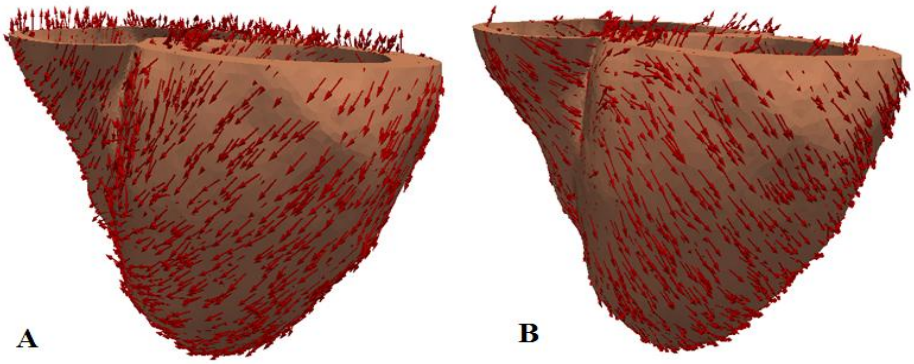

Figure 14: Streeter A) fiber and B) sheet direction vectors mapped on the ventricular mesh

The post processing for this study was performed on Matlab[4] and the visualization of the mesh, its fibers and its electromechanical properties on Paraview[5].

[4] http://www.mathworks.com/products/matlab/
[5] http://www.paraview.org/

B) Simulation under normal conditions (Control)

i) Electrophysiology

a) Pseudo-ECG

The ECG is the recording of the cardiac potential off the body surface. Instead of solving the expensive problem of a coupled heart-torso model, an approximation can be made, through an averaging of signal propagation and recording it via an electrode placed at a specified distance from the heart.[88] This approximation is called the pseudo-ECG and a Chaste post processing class[57] has been used to calculate it using the following formula[90];

$$\Phi_e(x', y', z') = D\int [-\nabla V_m \cdot (\nabla \frac{1}{r})]dx \tag{3.1}$$

where Φ_e is the extracellular potential at location (x', y', z'), D is the diffusion coefficient, V_m is the trans-membrane potential and r is the distance of the electrode from a source point (x, y, z) on the heart surface to the electrode position (x', y', z') such that;

$$r = [(x - x')^2 + (y - y')^2 + (z - z')^2]^{1/2} \tag{3.2}$$

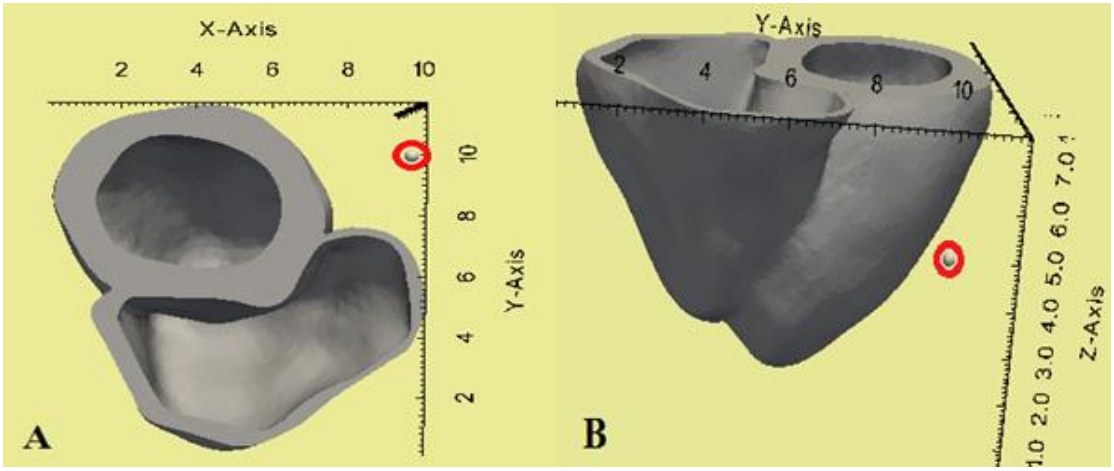

Figure 15: Basal (A) and side (B) view of the ventricle model with the electrode position coordinates at (10, 10, 5)

In this study, the diffusion coefficient was set to *1* and the electrode was placed in the position specified in Figure 15 such that (x', y', z') = (10.0, 10.0, 5.0), a location comparable to the surface of the torso. The pseudo-ECG computed from the voltage is plotted in Figure 16 from the beginning of the QRS complex to the end of the T-wave (QT interval), to assess ventricular activation and repolarization.[91] The

plot shows a good prediction of the QT interval, with a duration of a little over 350 ms, which is well within the expected range.[26]

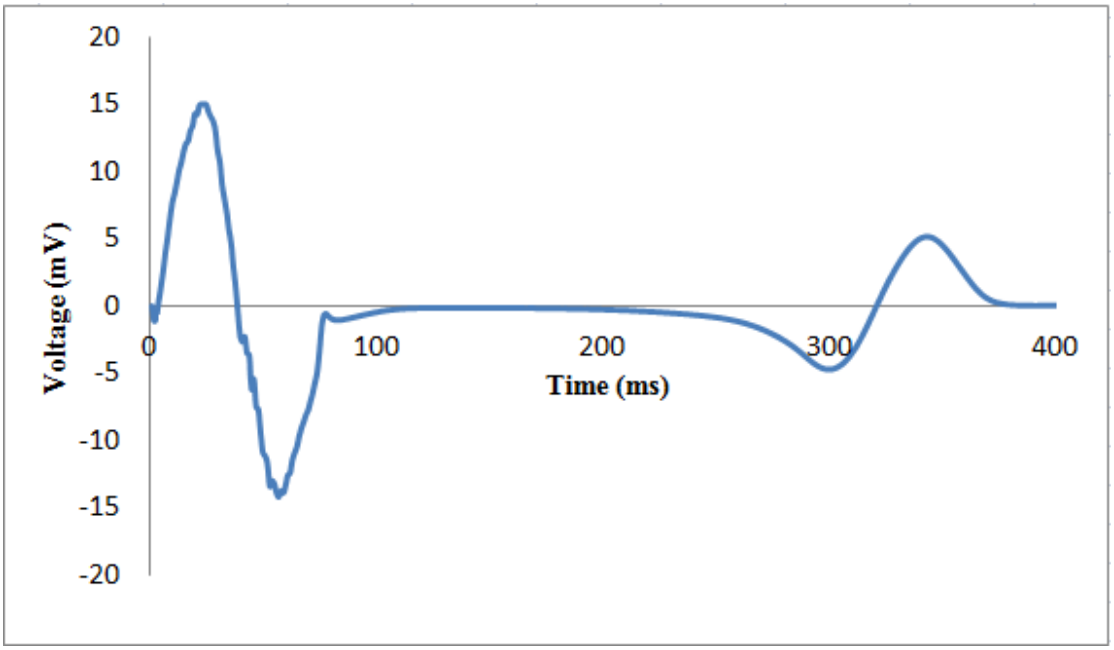

Figure 16: Pseudo-ECG plot of QT interval under normal conditions

b) Action Potential

The action potential (AP) generated by the ion flow through the cardiac cell membranes is recorded at each time step for every node in the mesh. The AP of a sample node is plotted in Figure 17 and it shows it undergoes the five phases of the cardiac activation and repolarization, and the action potential duration is under 400 ms.

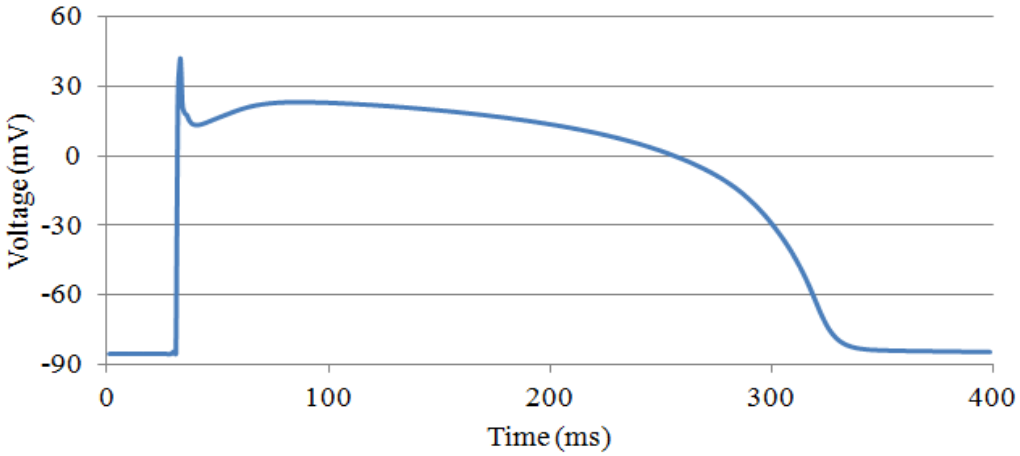

Figure 17: Action Potential plot under normal conditions

The total activation time, which is the time it takes for the excitation wave to propagate throughout the ventricles from the apical endocardium to the basal epicardial wall, is 77 ms. The ventricles completely repolarize at around 368 ms. All these values are consistent with the literature.[26] Figure 18A further captures the electrical excitation wave at mid propagation from the apex to the base, corresponding to a time of 45 ms. Figure 18B then shows complete tissue repolarization at time 300 ms. Conversely, Figure19A shows the map of activation times and Figure 19B the map of repolarization times for ventricles. All these predictions are again consistent with the literature.[26]

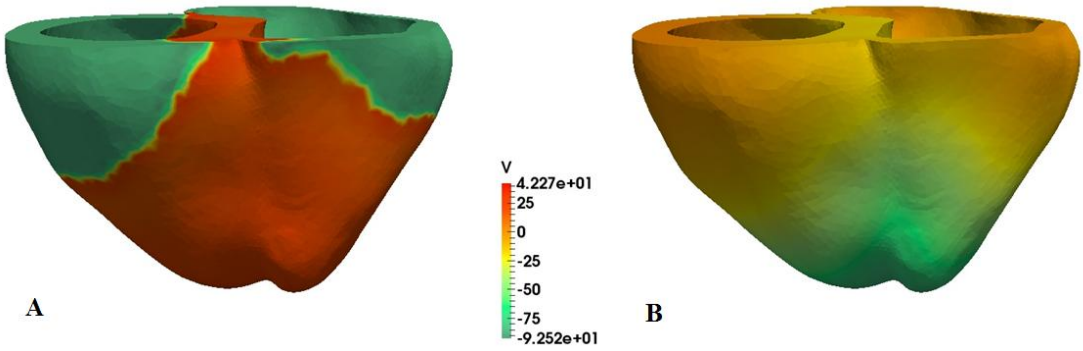

Figure 18: A) Depolarization at t=45 ms, B) Repolarization at t=300 ms

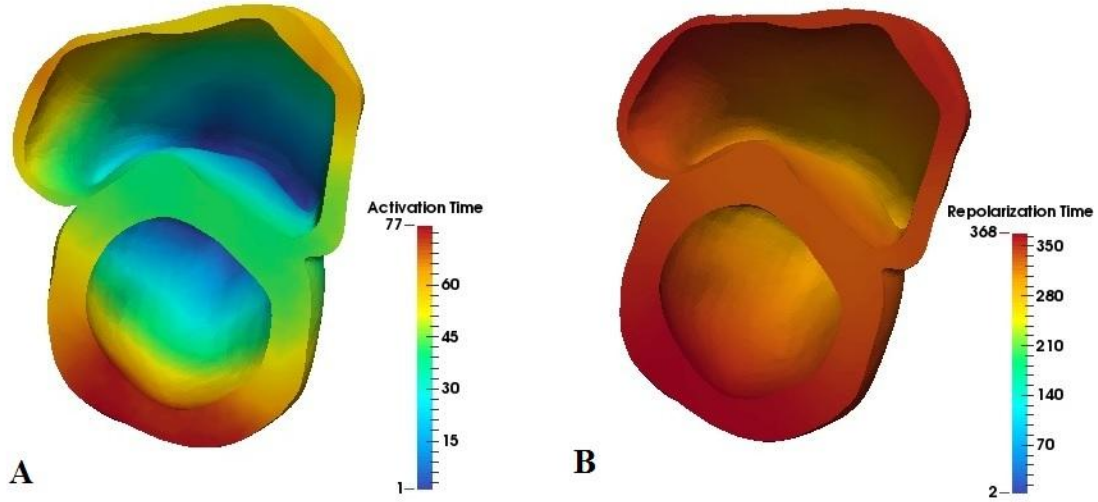

Figure 19: A) Activation time map, B) Repolarization time map

ii) Tissue Mechanics

The Kerckhoff contraction model was used to solve for the active tension, while the energy function proposed by Holzapfel and Ogden was used to generate the passive material stress. The passive stress and its Jacobian were developed using the C++ programming language, and intergrated on Chaste. The material is modeled as transversly isotropic by zeroing out 4 of the 8 material parameters. The material parameter values used herein are listed in Table 1, guided by a recent study due to Baillargeon et al.[51], which showed improved prediction of blood ejection fractions.

Table 1: Holzapfel and Ogden material parameters used in this study

A	a_f	a_s	a_{fs}	b	b_f	b_s	b_{fs}
0.33	0.25	0	0	7.08	5.34	0	0

For validation, our material model was run under the same conditions as, and compared against, the well-established transversly isotropic Pole-Zero material law, whose material parameters were proposed by Nash and Hunter[52]. Both models completed simulation of almost 90% of the cardiac cycle without difficulty, with our model running faster, reaching 350 ms in 325h 32m and the Pole-Zero material law reaching 350 ms in 334h 54m. After 90% of the cycle, both models exhibit instability in the mesh and diverge, prematurely ending the simulation.

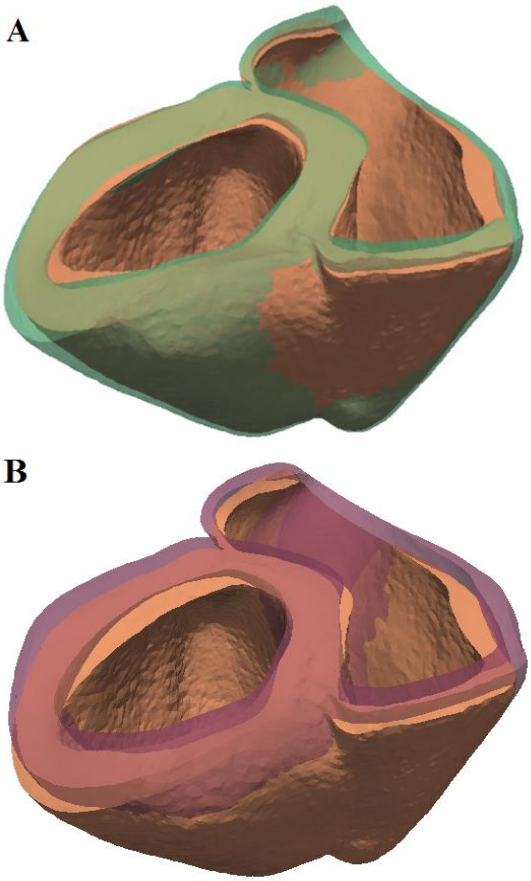

Figure 20: Ventricular contraction of A) Holzapfel and Ogden model (solid pink) against Pole-Zero model (translucent green)and B) Holzapfel and Ogden model (solid pink) against Mooney-Rivlin model (translucent purple)

To highlight the importance of the fiber orientation in the mechanical tissue deformation, our transversly isotropic material model was also

compared against the isotropic Mooney-Rivlin material model with material parameters c_1 = 2 and c_2 = 6, as proposed by Nash and Panfilov.[87] Unlike the transversly isotropic models, the Mooney-Rivlin model ran till the end of the simulation reaching 400 ms in 249h 12m.

Figure 20 shows the maximum ventricular contraction resulting from the models superimposed, with the solid pink representing the Holzapfel and Ogden model, the translucent green representing the Pole-Zero model (Figure 20A) and the translucent purple representing the Mooney-Rivlin model (Figure 20B). The models exhibit similar looking contractions, however the Holzapfel and Ogden model appears slightly more contracted, which is desirable.

For a proper comparison, a side-by-side map of tissue deformation of the Holzapfel and Ogden model against the Pole-Zero model, colored by strain distribution and stress distribution, is shown in Figures 21 and 22, respectively. The strain and stress maps of the Holzapfel and Ogden model against the Mooney-Rivlin model are shown in Figures 23 and 24, respectively. The effective deviatoric stress and the effective deviatoric strain were calculated at each element of the mesh at 50 ms intervals. The deviatoric component of the stress and strain tensors only accounts for the distortional element of the tensor without the volume change (as tissue is incompressible); deviatoric stress is calculated as follows:

$$\sigma'_{ij} = \sigma_{ij} - \frac{1}{3}\delta_{ij}\sigma_{kk} \tag{3.3}$$

and the deviatoric strain as:

$$\epsilon'_{ij} = \epsilon_{ij} - \frac{1}{3}\delta_{ij}\epsilon_{kk} \tag{3.4}$$

The effective stress is then calculated as:

$$\sigma_{eff} = \sqrt{\frac{3}{2}\sigma' : \sigma'} \tag{3.5}$$

and the effective strain as:

$$\epsilon_{eff} = \sqrt{\frac{2}{3}\epsilon' : \epsilon'} \tag{3.6}$$

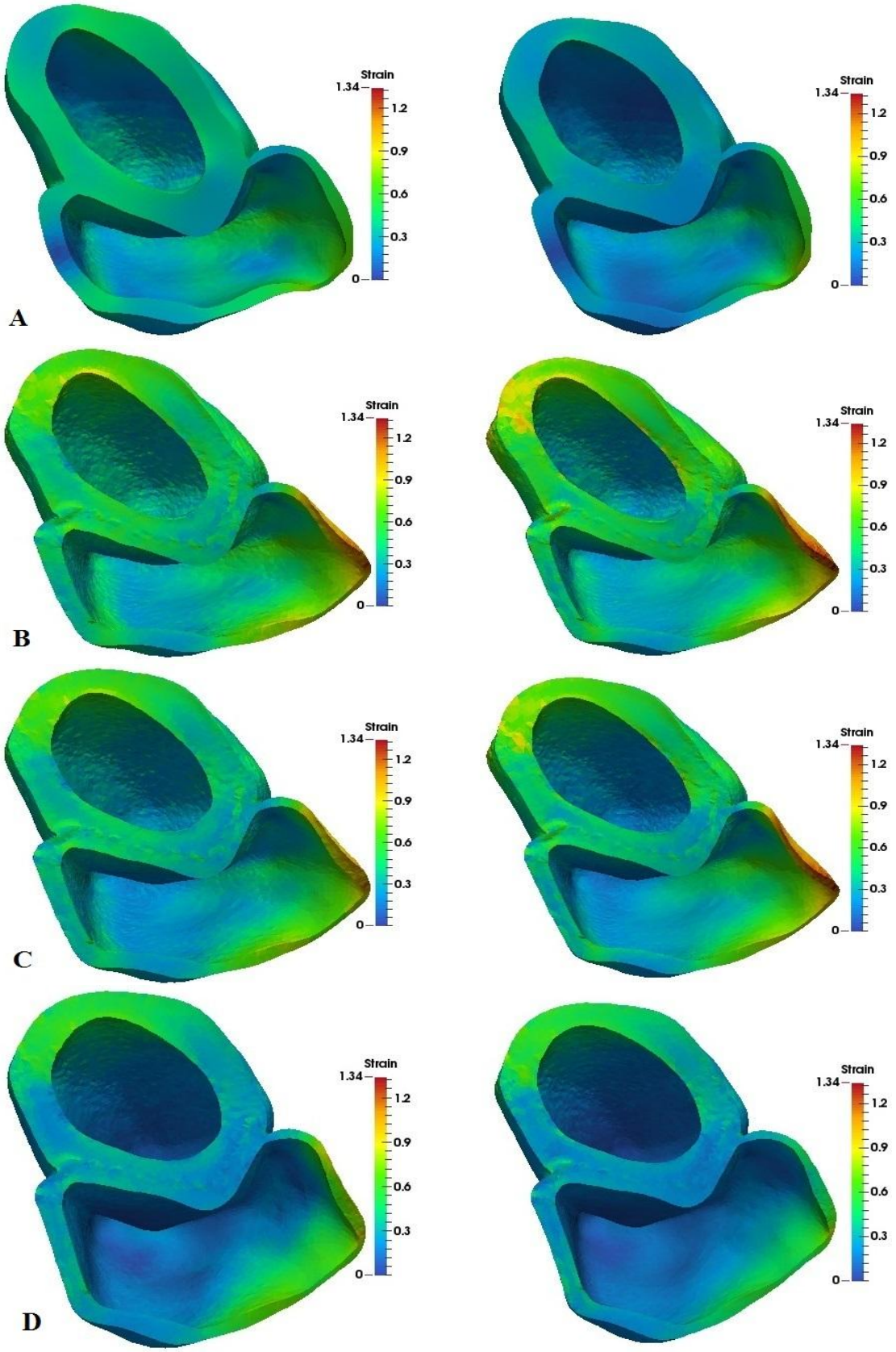

Figure 21: Strain distribution maps of the Holzapfel and Ogden model on the left and the Pole-Zero model on the right at times A) 50 ms, B) 200 ms, C) 300 ms, D) 350 ms

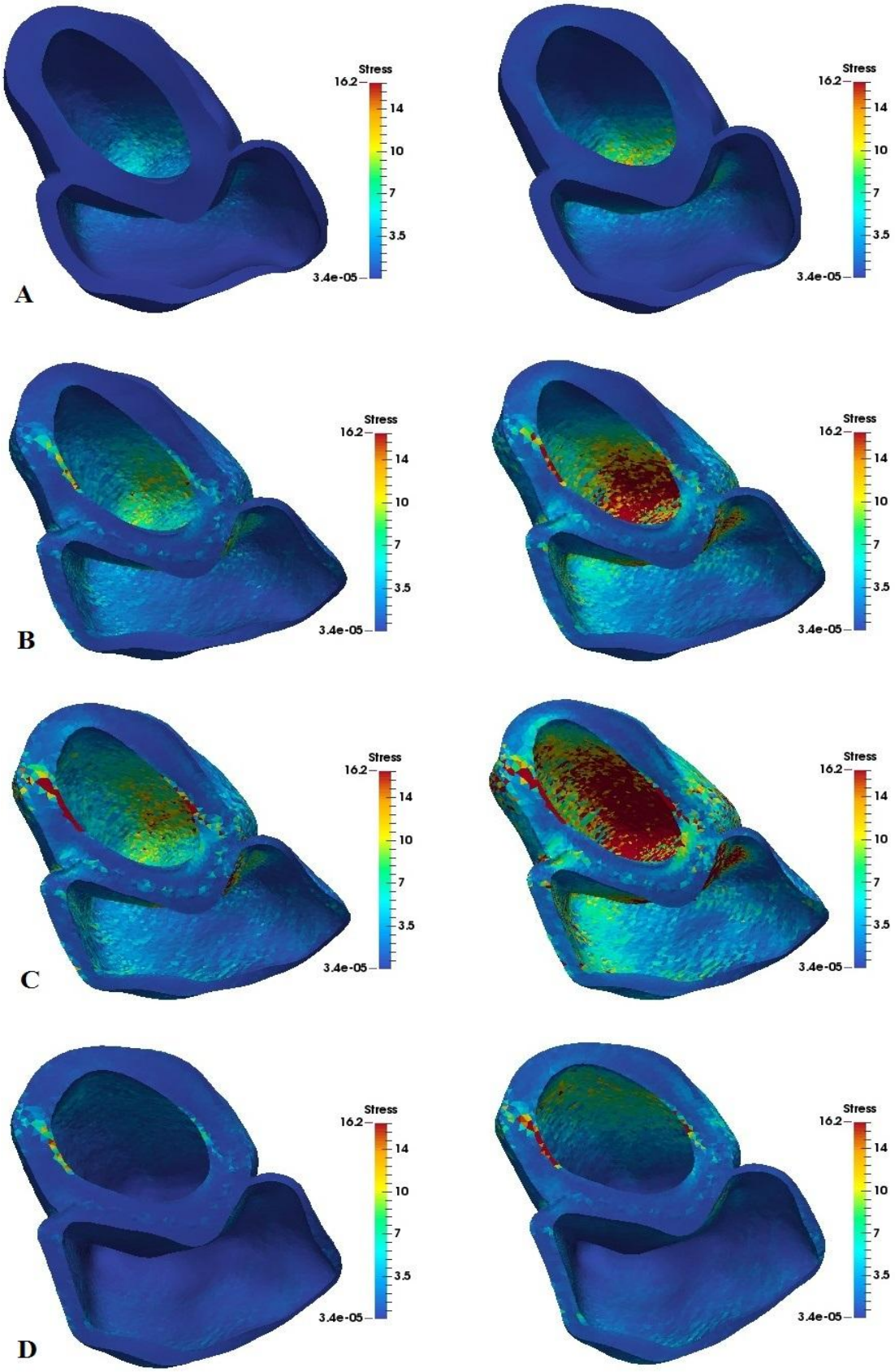

Figure 22: Stress distribution maps of the Holzapfel and Ogden model on the left and the Pole-Zero model on the right at times A) 50 ms, B) 100 ms, C) 200 ms, D) 350 ms

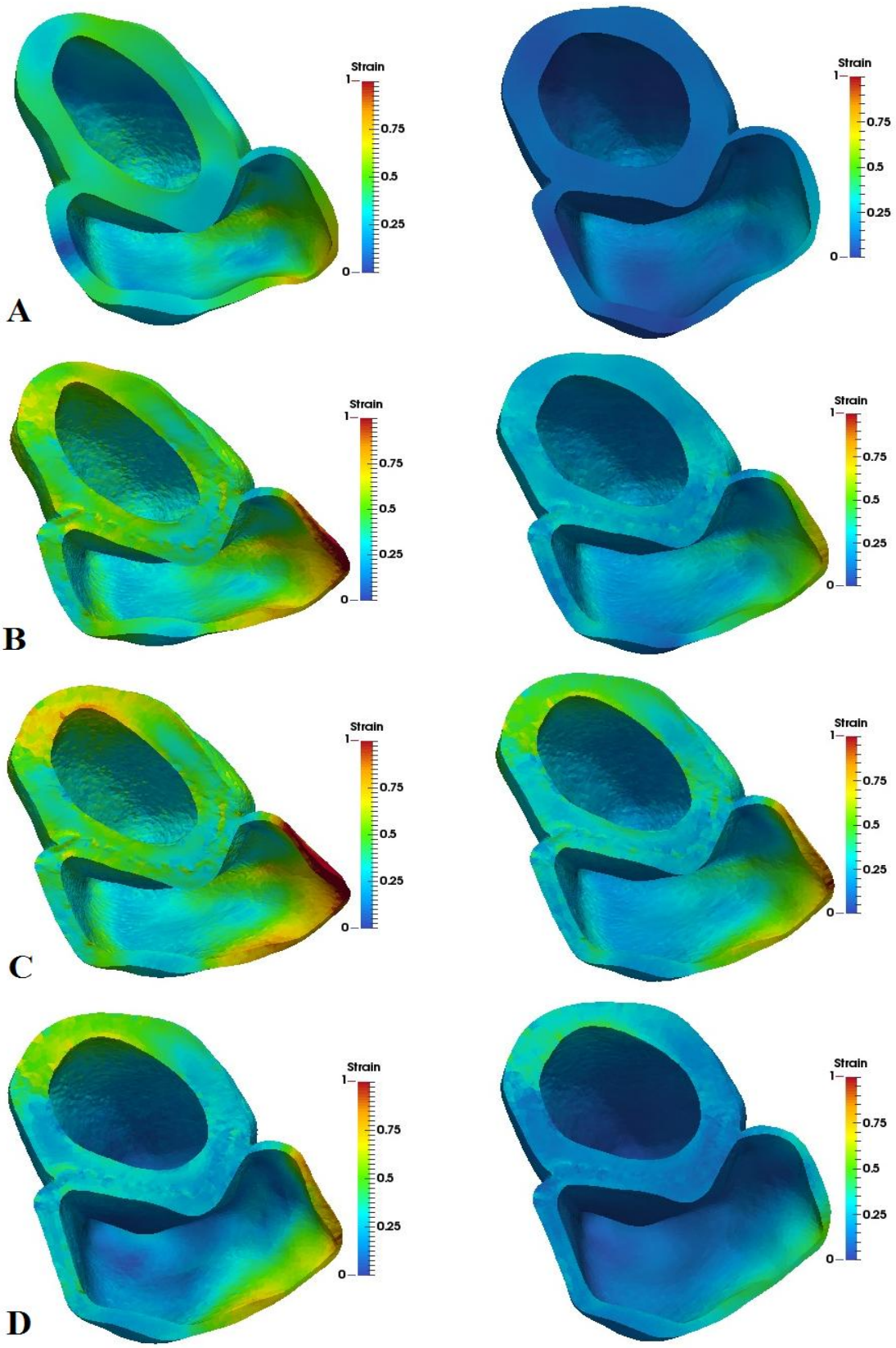

Figure 23: Strain distribution maps of the Holzapfel and Ogden model on the left and the Mooney-Rivlin model on the right at times A) 50 ms, B) 100 ms, C) 250 ms, D) 350 ms

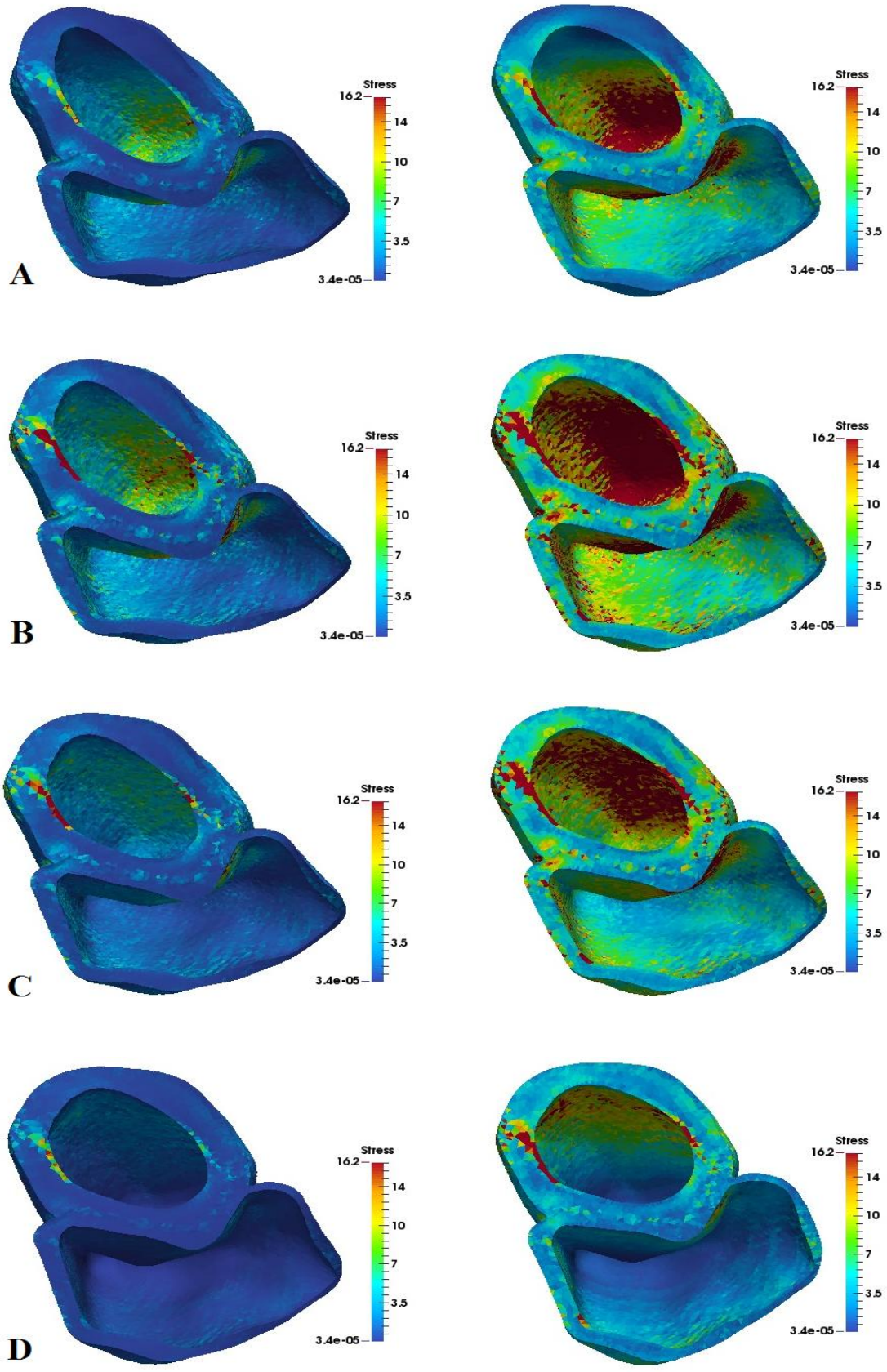

Figure 24: Stress distribution maps of the Holzapfel and Ogden model on the left and the Mooney-Rivlin model on the right at times A) 100 ms, B) 200 ms, C) 300 ms, D) 350 ms

Looking at the predicted strain maps of the Pole-Zero model compared to the Holzapfel and Ogden model, small differences appear in the basal area and on the surface, especially close to the time of 300 ms (repolarization), but both models are comparable in terms of strain distribution. For the stress distribution maps, however, the Pole-Zero model clearly exhibits higher stress levels than the Holzapfel and Ogden model throughout the cycle, which indicates a much stiffer response from the Pole-Zero model.

As for the Mooney-Rivlin model, the strain appears to be much less pronounced than the Holzapfel and Ogden model while the stress appears to be much more pronounced. This indicates that the lack of fiber direction in the cardiac muscles leads to less tissue deformation and a stiffer response from the model.

To further quantify the mechanical behavior predicted, and decide on which model is preferable to move forward with, several biomarkers are used, including; the ventricular volume, the ejection fraction, the left ventricle twist angle between the apex and the base, the longitudinal strain, and the radial strains. These are analyzed next.

a) Ventricular volume

At each time step, to measure the volume enclosed by the ventricles (which is irregular), left ventricle and right ventricle endocardiac nodes are first separated from the rest of the mesh, and then from each other. For the ventricular node sets, alpha shapes are formed where all the nodes are connected turning the hollow ventricle into a solid body that is divided into tetrahedrons as shown in Figure 25. They are used to define the correct shape of the irregular cavities of the ventricles and calculate the correct volumes using a ready developed Matlab code.[6]

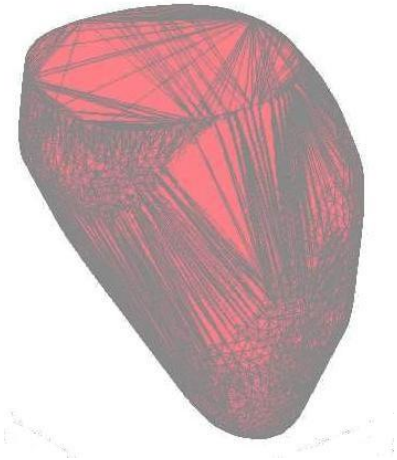

Figure 25: Delaunay triangulation of the left ventricle to calculate volume

Figure 26 plots the changing volume of the LV and RV through time, when using the Holzapfel and Ogden model, the Pole-Zero model, and the Mooney-Rivlin model. The starting volume of the LV and RV are 96.7 cm^3 and 96.6 cm^3. With the Holzapfel and Ogden model, the LV reaches a minimum volume of 69.4 cm^3 at time 190 ms and the RV reaches its minimum volume 75.5 cm^3 at time 90 ms. As for the Pole-Zero model, the LV minimum volume reached is 78.7 cm^3 at 200 ms and minimum RV volume of 84.7 cm^3 at 90 ms. The Mooney-Rivlin model doesn't show much volume difference from the Pole-Zero model with a minimum LV volume of 80.5 cm^3 at 200 ms and a RV volume of 85.4 cm^3 at 190 ms.

Hence the Holzapfel and Ogden model shows significantly more contraction than both the Pole-Zero and the Mooney-Rivlin models. Surprisingly, despite the lack of fiber and sheet directions, the ventricular volume reduction of the Mooney-Rivlin model is close to that of the Pole-Zero model which indicates that in terms of ventricular contraction it is not a bad alternative for the Pole-Zero model specially when accounting for its speed and stability. However, these systolic volumes of the ventricles do not match those obtained from clinical data, which can reach as low as 24 cm^3 and 40 cm^3 for the left and right ventricles, respectively[92], but they do exhibit the same patterns of volume change through time.[46]

[6] http://www.mathworks.com/matlabcentral/fileexchange/28851-alpha-shapes/content/alphavol.m

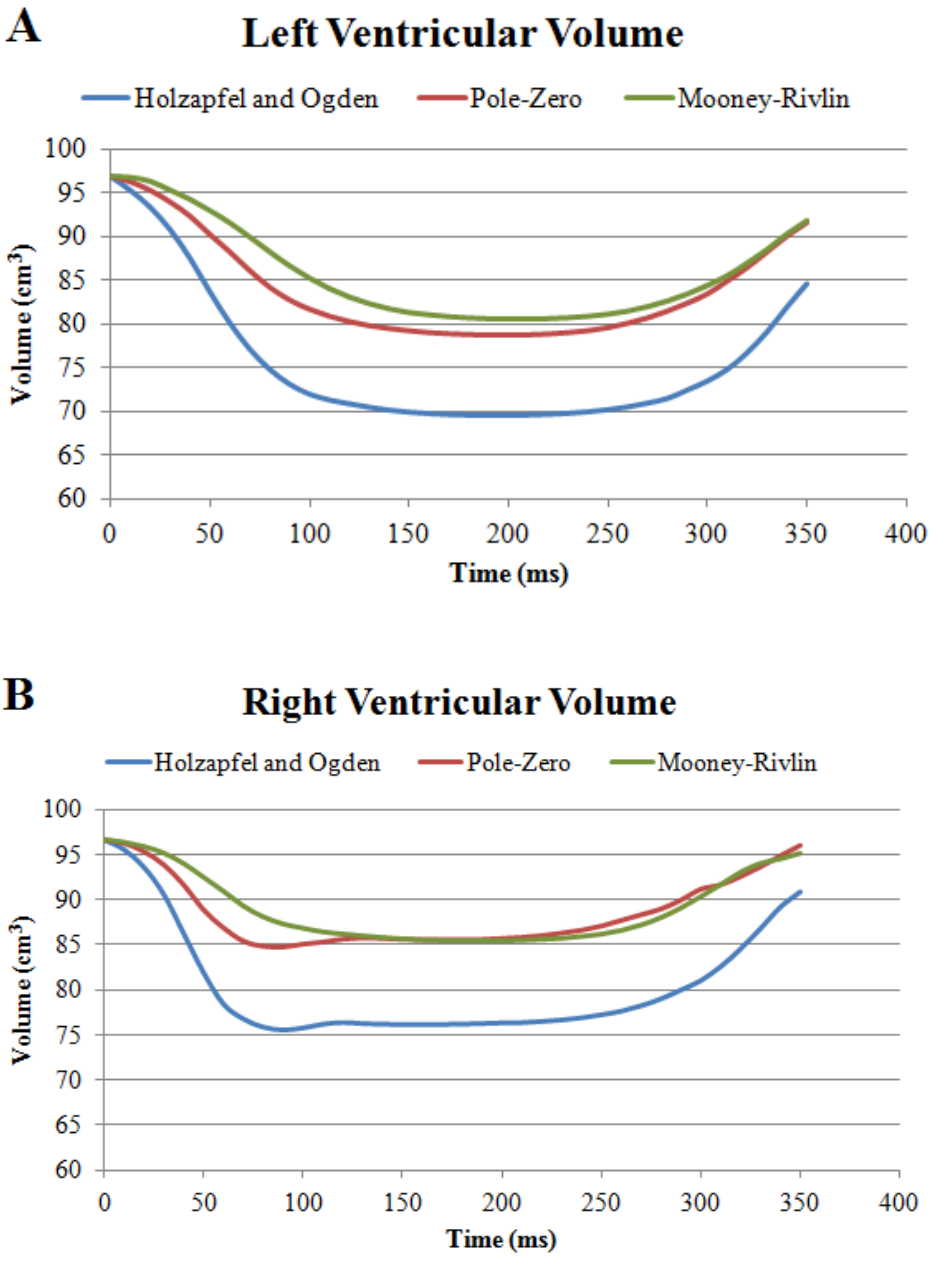

Figure 26: Volume change through time of A)left and B)right ventricles with the Holzapfel and Ogden model vs. the Pole-Zero and the Mooney-Rivlin models

b) Ejection Fraction

The ejection fraction (EF) is the percentage of blood ejected from the ventricles during contraction. It is a very good indicator of how healthy the heart is, by measuring how well it is pumping blood. It is calculated from the formula[93];

$$EF = 100\frac{EDV-ESV}{ESV} \tag{3.7}$$

where EDV is the end diastolic volume and ESV is the end systolic volume. The values of the EFs predicted by the Holzapfel and Ogden, the Pole-Zero, and the Mooney-Rivlin models are shown in Table 2.

Table 2: Ejection Fraction values for Holzapfel and Ogden vs. Pole-Zero and Mooney-Rivlin models

Holzapfel and Ogden		Pole-Zero		Mooney-Rivlin	
LV	RV	LV	RV	LV	RV
28.2%	21.8%	18.7%	12.2%	16.8%	11.6%

As expected from the volume change curves, the Holzapfel and Ogden model exhibits a larger EF than the Pole-Zero and Mooney-Rivlin models due to the larger change in volume. The values are still considerably far from clinical data[94], but are consistent with various computational model results in literature[51], and should thus be sufficient for our purpose of detecting the change in the heart's performance under drug influence. In fact, this newly developed model provides a considerable improvement to the ones on Chaste.

c) Left Ventricle Twist

The helical structure of the fiber distribution in the ventricles induces torsion in the cardiac muscles during contraction, and plays a crucial role in ventricular blood filling and ejection.[46] As shown in Figure 27, to measure the twist angle in the LV, we define an axial vector, which extended from a fixed point at the apex to the middle of the cavity at the base, whose orientation we follow in the initial and the contracted meshes. A second (radial) vector was extended from the axial vector, standing at the base, in the middle of the LV cavity, to a chosen point on the LV wall. We also follow the motion of this radial vector in the initial and contracted meshes. Note that measuring the angle between the initial and deformed radial vectors is not suitable, since their orthogonality to the axial vector is not guaranteed, particularly after contraction. Hence, a third (normal) vector, orthogonal to both the axial and the radial vectors in each of the meshes, is obtained from the cross product of the axial and radial vectors. The angle between these normal vectors in the intial and deformed meshes is thus calculated to indicate the twist angle of the LV.

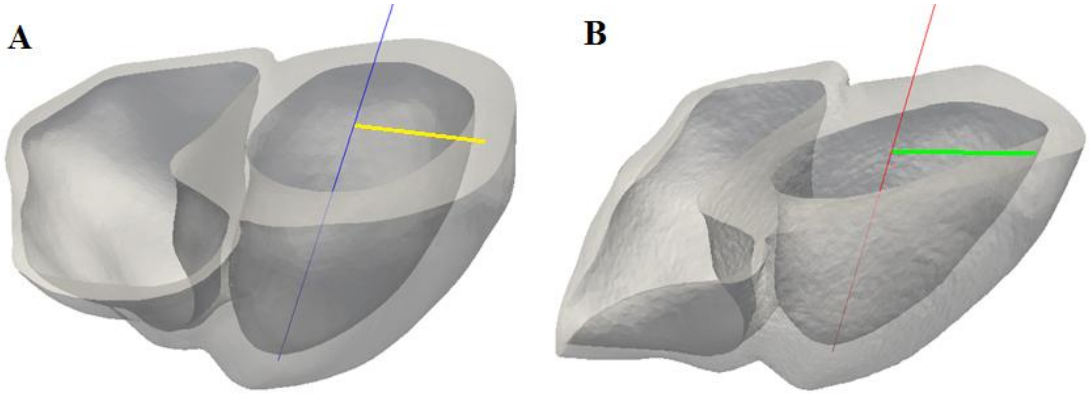

Figure 27: A) Undeformed mesh with an axial vector (blue) through the LV and a radial vector(yellow) connecting it to the LV wall B) Deformed mesh with an axial vector (red) through the LV and a radial vector(green) connecting it to the LV wall

Unlike the Mooney-Rivlin model, the resulting twist angle for both transverse isotropic material models is in very good agreement with the range of experimental measures in literature.[95,96] The changing twist angle over time is plotted in Figure 28. The Holzapfel and Ogden model predicts a maximum twist angle of 15.3 degrees 80 ms into the simulation while the Pole-Zero model predicts a lower maximum twist angle of 12 degrees at 90 ms and the Mooney-Rivlin model predicts a maximum twist angle of 5.2 degrees at 150 ms. The low twisting effect of the Mooney-Rivlin model is a clear consequence of the lack of fiber and sheet orientation definitions which indicates their importance in recreating the LV torsion of the contracting heart.

More interesting, is that the trend the Holzapfel and Ogden model predicts for LV twist angle is more similar to clinical data than the other two models[46], which confirms it is an important improvement of the models in Chaste.

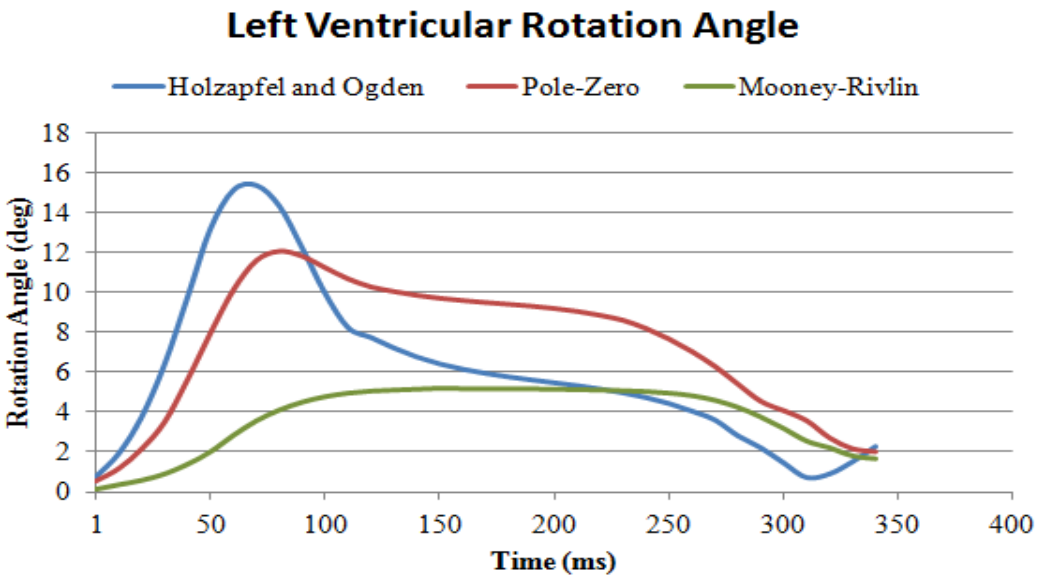

Figure 28: Left Ventricle rotation angle change over time of the Holzapfel and Ogden model vs. the Pole-Zero and the Mooney-Rivlin models

d) Longitudinal and Radial Strains

The longitudinal and radial strains are the main indicators of change in dimensions. The longitudinal strain is measured through the septum as shown in Figure 29 to indicate longitudinal shortening during contraction. Two radial strains are also measured for each ventricle, one in the lengthening direction (long) and the other in the shortening direction (short) as shown in Figure 30.

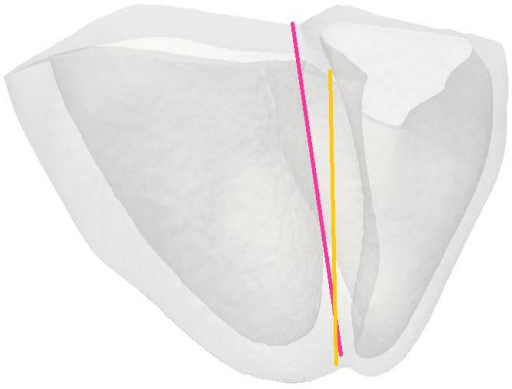

Figure 29: Longitudinal axis from apex to base in the undeformed (pink) and deformed meshes (orange)

The radial strains measured in this study cannot compare favorably to clinical measurements since the deformation at the base of the ventricles is actually limited by its attachment to the atria. However, the measurements are here used to evaluate the change in model dimensions for the different material models, and under the influence of drugs.

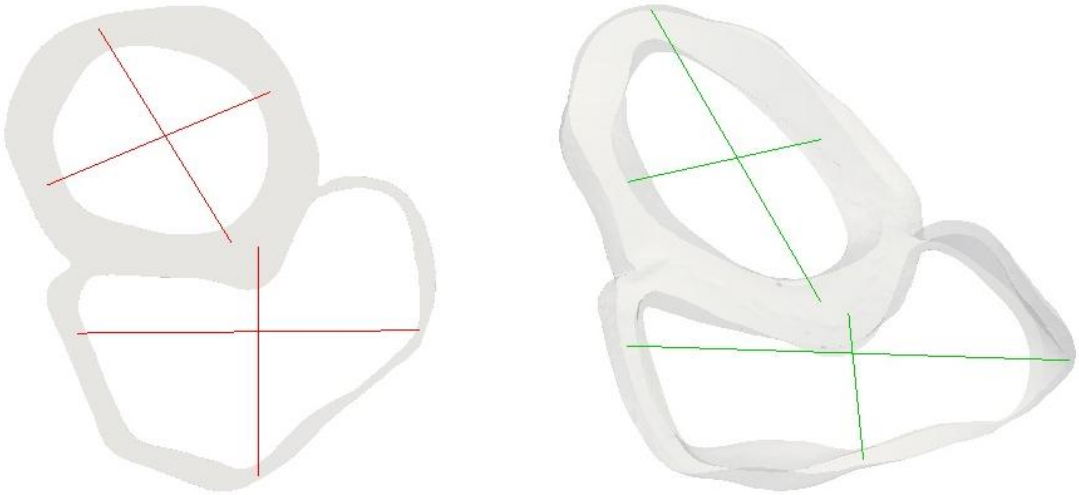

Figure 30: Radial lines indicating their position in the undeformed mesh (left) and in the deformed mesh (right)

The plot of the longitudinal strain through time is shown in Figure 31. The results further support that the Holzapfel and Ogden model is able to produce more longitudinal shortening, of 12.8%, and exhibit stronger contractile effects than the Pole-Zero, whose maximum shortening is 11.7% and the Mooney-Rivlin with maximum shortening of 9.1%.

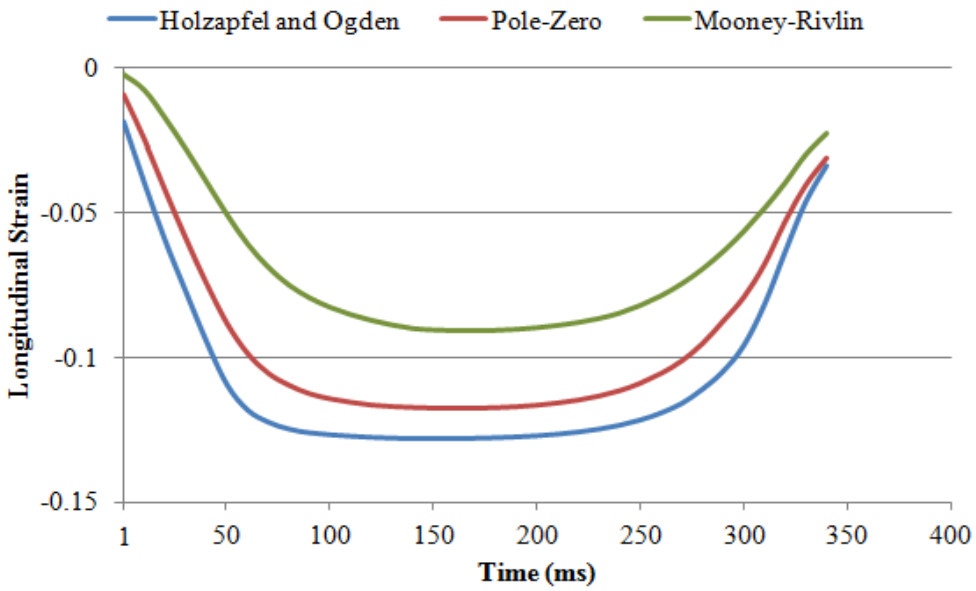

Figure 31: Longitudinal strain plot for the Holzapfel and Ogden model vs. the Pole-Zero and the Mooney-Rivlin models

From the basal view, the ventricles appear to be squeezed in one direction and stretched in the other, so the radial strain is measured in both directions for each ventricle. Figure 32 of the LV long side deformation indicates that the anisotropic models exhibit the same maximum stretch, but different patterns of deformation. However, for the short side, plotted in Figure 33, the Holzapfel and Ogden model causes the LV to record larger contraction than the Pole-Zero model. The Mooney-Rivlin plots indicate that the model does not reach the levels of stretching and squeezing of the other two models due to the stiffness of the model resulting from the lack of fiber and sheet directions.

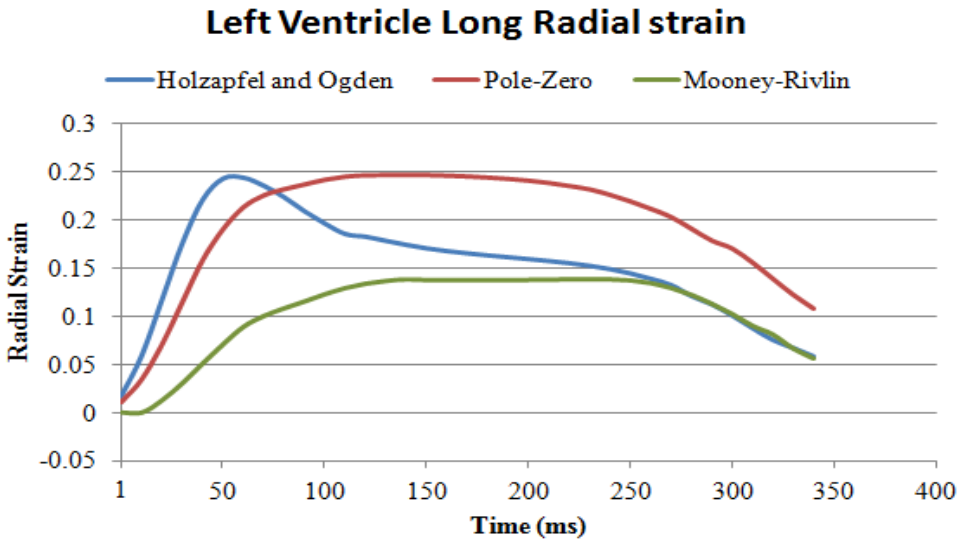

Figure 32: Left Ventricle strain in the long direction for the Holzapfel and Ogden model vs. the Pole-Zero and Mooney-Rivlin models

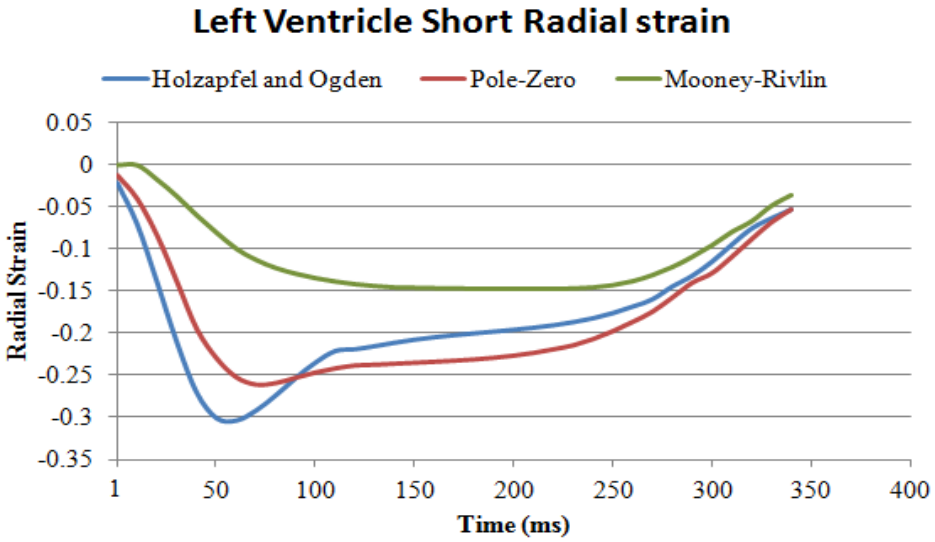

Figure 33: Left Ventricle strain in the short direction for the Holzapfel and Ogden model vs. the Pole-Zero and Mooney-Rivlin models

With the regards to the radial strains of the RV, for the long side, all three models appear to exhibit a similar stretch pattern. However, the Pole-Zero model seems to be somewhat delayed and the Mooney-Rivlin model gives significantly less stretching. As for the short side, they again predict similar strain patterns, but the Holzapfel and Ogden model again records a higher shortening percentage than both the Pole-Zero and the Mooney-Rivlin models. The percentages of stretching and shortening are recorded in Table 3.

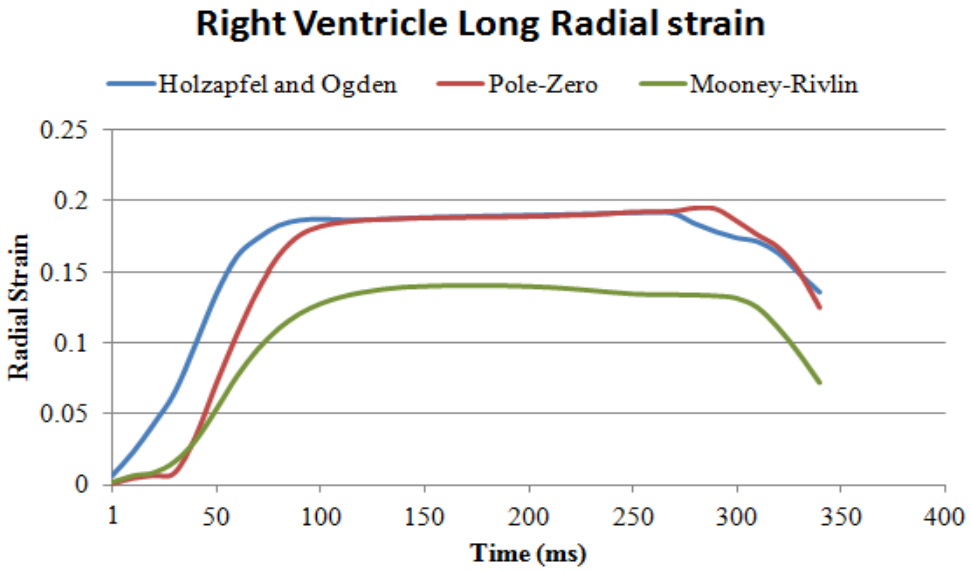

Figure 34: Right Ventricle strain in the long direction for the Holzapfel and Ogden model vs. the Pole-Zero and the Mooney-Rivlin models

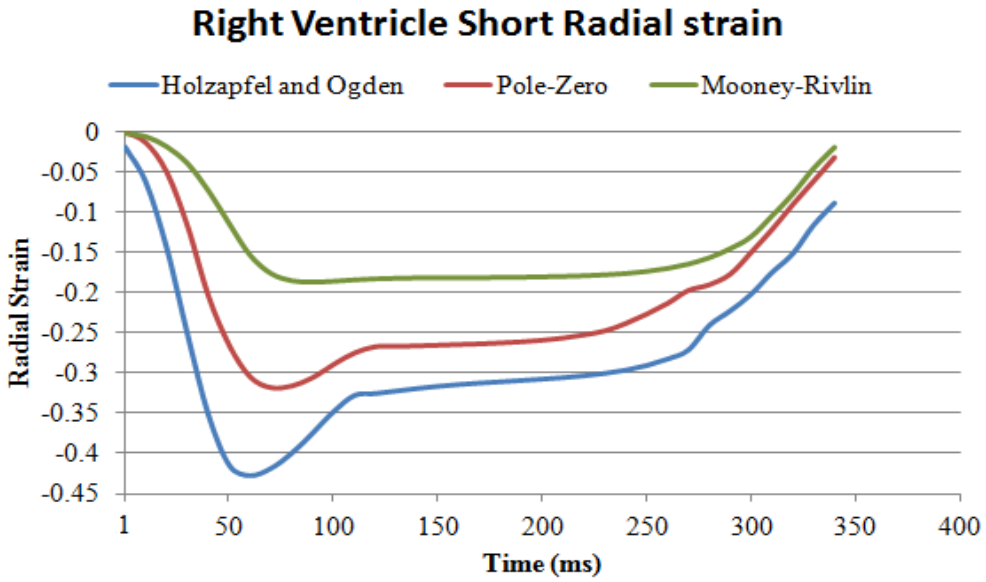

Figure 35: Right Ventricle strain in the short direction for the Holzapfel and Ogden model vs. the Pole-Zero and the Mooney-Rivlin models

Table 3: Radial stretching and shortening of the Holzapfel and Ogden model and the Pole-Zero model

Holzapfel and Ogden				Pole-Zero				Mooney-Rivlin			
LV		RV		LV		RV		LV		RV	
Long	Short	Long	Short	Long	Short	Long	Short	Long	Short	Long	Short
24%	30%	19%	42%	24%	26%	19%	32%	14%	15%	14%	18%

In summary, the results comparing between the two mechanical models validate the Holzapfel and Ogden model we developed on Chaste for this study, and in fact the various biomarkers we studied provide sufficient evidence that it gives superior results in terms of predicting cardiac functionality. The results also validate the need for fiber orientation definition especially for the modeling of the LV twisting and the longitudinal shortening.

Therefore, the Holzapfel and Ogden model was selected for the investigation of the effect of nanodrug influence on cardiac mechanics, whose results are reported next.

C) Effects of Sodium channel blockage

The sodium channel activation is responsible for the depolarization of cardiac myocytes.[97] Sodium channel blocks are known to cause activation time delays resulting from the decrease in conduction velocity through the cardiac tissue.[26] This blockage can be caused by drugs of the type Class I antiarrhythmics, which specifically target the sodium channels, or even by non-cardiovascular drugs such as antipsychotics and anticonvulsants.[97] The simulation was carried out using the Holzapfel and Ogden model under the same conditions of the Holzapfel and Ogden control simulation with an IC_{50} dose of a sodium channel blocker.

i) Electrophysiology

Figure 36A compares the average activation time of the simulation under the influence of a sodium channel blocker with the control and shows an average delay of about 9 ms. The conduction velocity was also plotted in Figure 36B showing the sodium channel block causing a decrease in conduction velocity of the action potential in the ventricles. Figure 37 compares the conduction velocities of the control and sodium channel blocked simulations. It shows how far along the ventricles the electrical wave has spread at t = 45ms showing the one under drug influence to be clearly falling behind. This activation delay and reduced conduction velocity are consistant with findings in literature.[26]

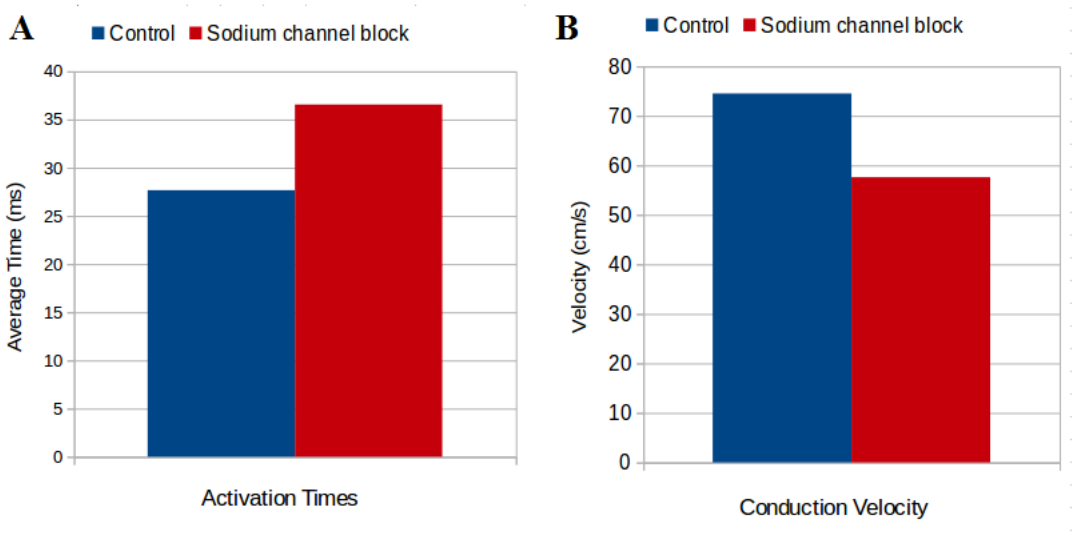

Figure 36: The A) activation time and B) conduction velocity of action potential through the ventricles for control (blue) and for IC50 dose of a sodium channel blocker (red)

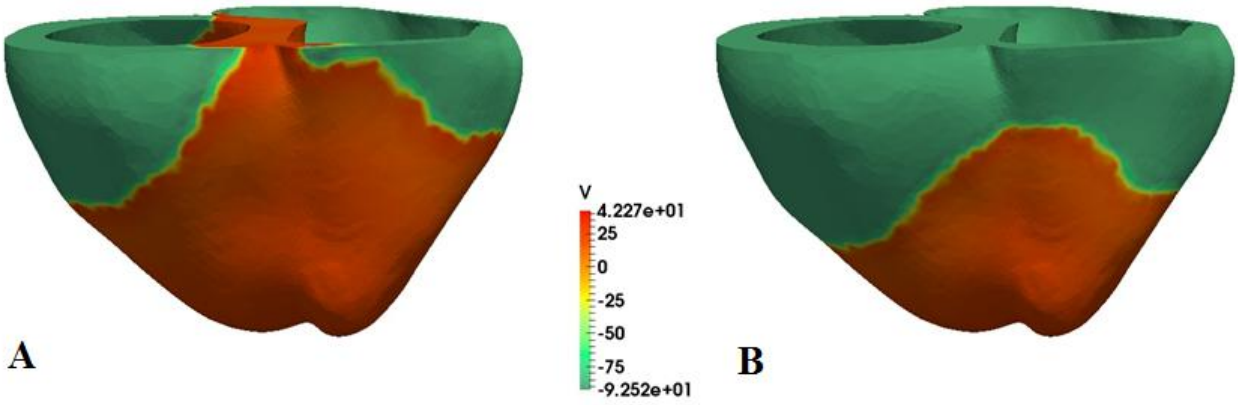

Figure 37: Electrical wave propagation along the ventricular mesh for A) control and B) sodium channel blockage

Figure 38 plots the simulated effect of the sodium channel blocker on pseudo-ECG against the control. Results show a clear prolongation in the QRS complex due to the decreased rate of depolarization and, even though the blockage does not affect repolarization, the T-wave experiences a shift forward as a result of the delayed activation. The alterations in the QT interval match those reported in literature.[43]

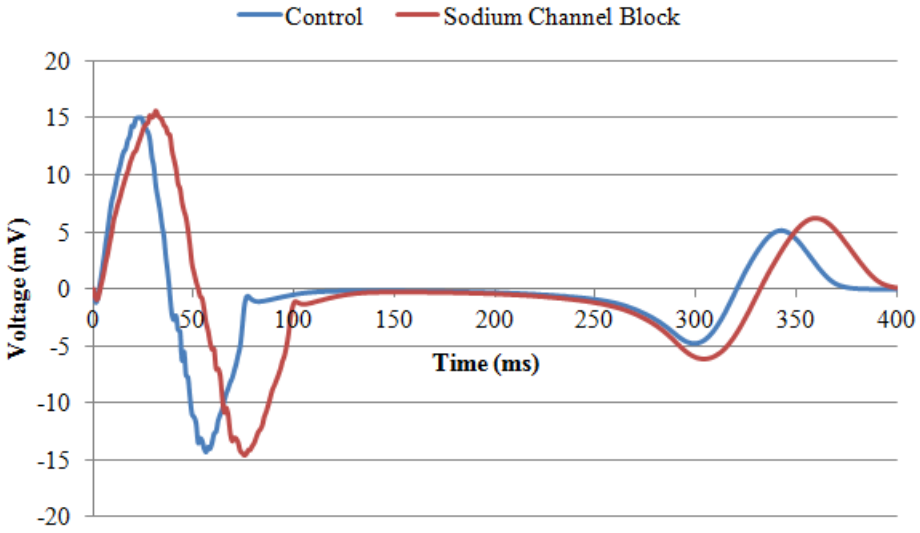

Figure 38: Pseudo-ECG QT interval for control (blue) and for IC50 dose of a sodium channel blocker (red)

This consequence of the conduction delay during activation on the repolarization is also clear in the AP plot in Figure 39. The changes in the AP curve are also consistant with the literature.[23,26] It exhibits a decrease in maximum voltage amplitude and a deflection in the activation-repolarization cycle which results in the prolongation of the action potential duration. Figure 40 shows a difference in

repolarization times between the control and the influence of sodium channel block of about 9 ms, which is the same difference between the activation times confirming that there is no additional effect on the repolarization by the sodium channel block.

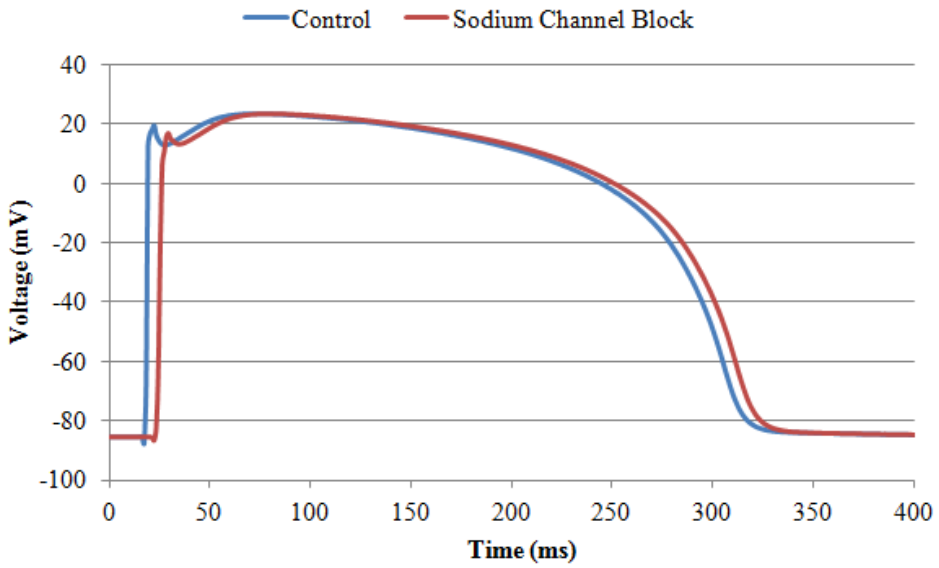

Figure 39: Action potential for control (blue) and for IC50 dose of a sodium channel blocker (red)

Activation time maps for the ventricular model in Figure 41 show the effect of the sodium channel blocker on the tissue activation time. The color gradient in Figure 41A shows the maximum time for tissue activation under normal conditions is 77 ms while in Figure 41B under sodium channel blocker influence, the same tissue activation time reaches 100 ms. Figure 42 compares the repolarization time maps highlighting the slight delay in the drug influences simulation. The activation maps produced appear to have similar patterns to those found in literature.[26]

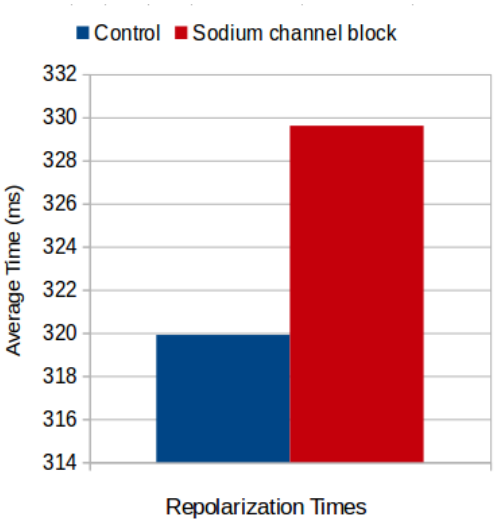

Figure 40: Repolarization time for control (blue) and for IC50 dose of a sodium channel blocker (red)

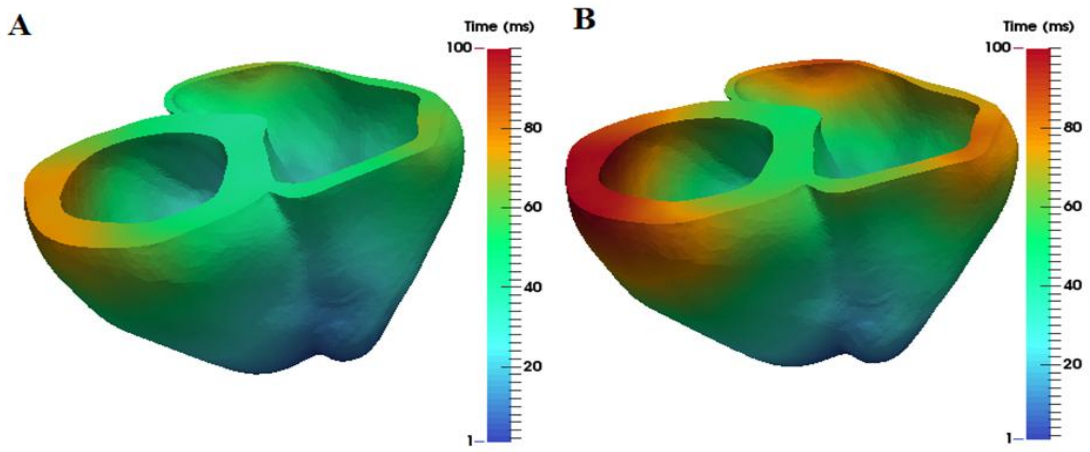

Figure 41: Activation time maps of the ventricular meshes A) under control conditions and B) under the influence of sodium channel blocker

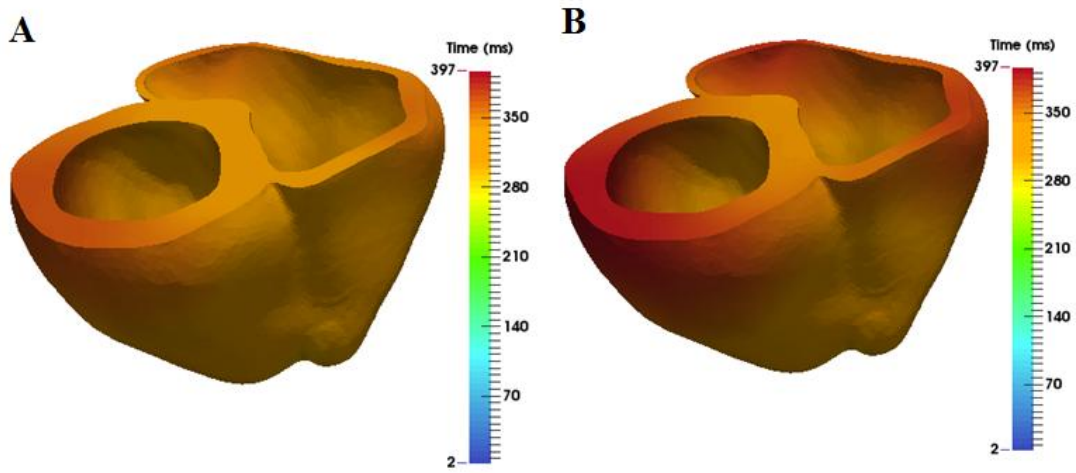

Figure 42: Repolarization time maps of the ventricular meshes A) under control conditions and B) under the influence of sodium channel blocker

It is thus established that simulation results are consistent with experimental results[21] and computational model results[26,43] in literature regarding the effect of sodium channel blockers on the reduced rate of depolarization and the decreased action potential conduction velocity.

ii) Tissue Deformation

As previously discussed, so far in literature the effect of drugs has only been studied on the electrophysiology of the heart. Studying the mechanical results will give an answer to how much these electrical changes affect the mechanical pumping of the heart.

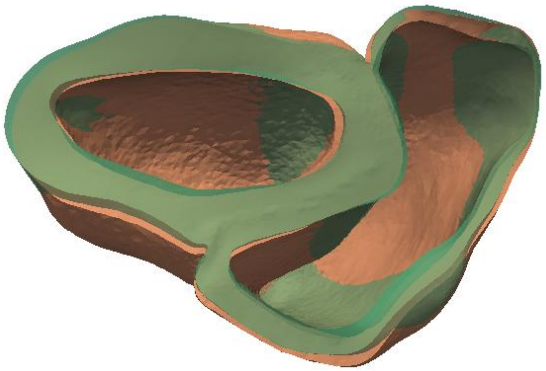

Figure 43: Ventricular contraction of the control (solid pink) vs. Na+ blocked model (translucent green)

The mechanical results of the coupled simulation under the influence of an IC_{50} dose of a sodium channel nanodrug were compared to the control run under normal conditions using the same Holzapfel and Ogden material model. Figure 43 shows the ventricular contraction of the two simulations superimposed with the control as the solid pink mesh and the nanodrug influenced as the translucent green. They appear to be slightly out of synch, but the data needs to be quantified to understand the extent of the nanodrug effect on the heart function .

The effective deviatoric strain distribution maps of the nanodrug influenced model are compared against the control in Figure 44. However, no observable difference can be noted between the two strain distributions.

The effective deviatoric stress distribution maps are also compared in Figure 45. There does appear to be a slight difference between the 2 distributions. In Figure 45A, stresses seem to rise at the endocardium of the LV at the base in the control simulation, while they are only just starting to appear in the drug influenced model. In 45B, the stresses rise in the drug influenced model as well, but they appear to be behind the control. At the end of the simulation, in Figure 45D, the stresses in the drug influenced model seem to be falling at a lower rate than the control model. So far, these findings are consistent with what is known about sodium channel blocking causing a delay in the cardiac cycle.[18,26]

The mechanical biomarkers are calculated next for the drug influenced model and compared to the control to quantify the extent of the effect of the sodium channel blockage on the cardiac function.

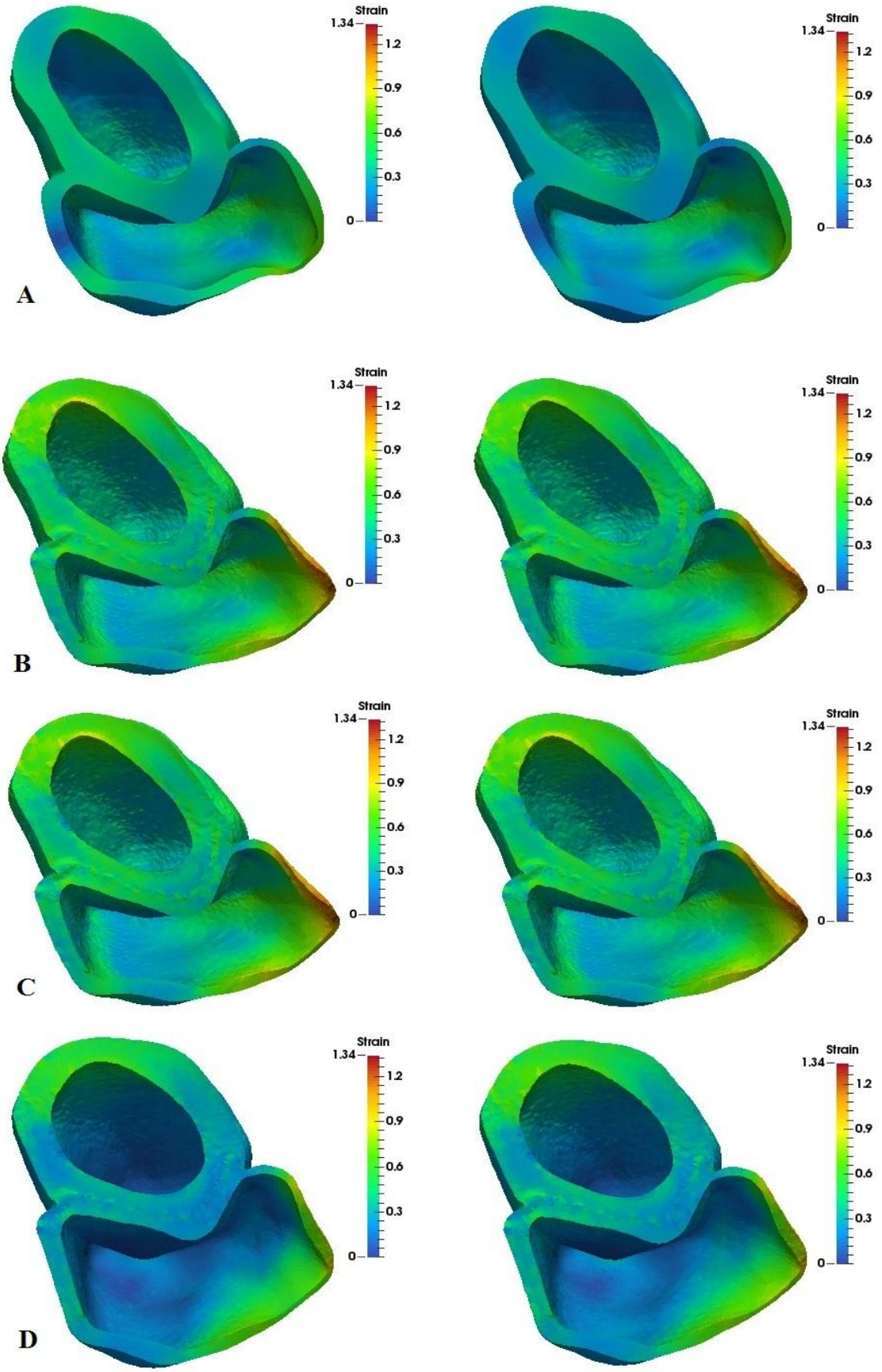

Figure 44: Strain distribution maps of the control on the left and under Na^+ channel blocking on the right at times A) 50 ms, B) 150 ms, C) 250 ms, D) 350 ms

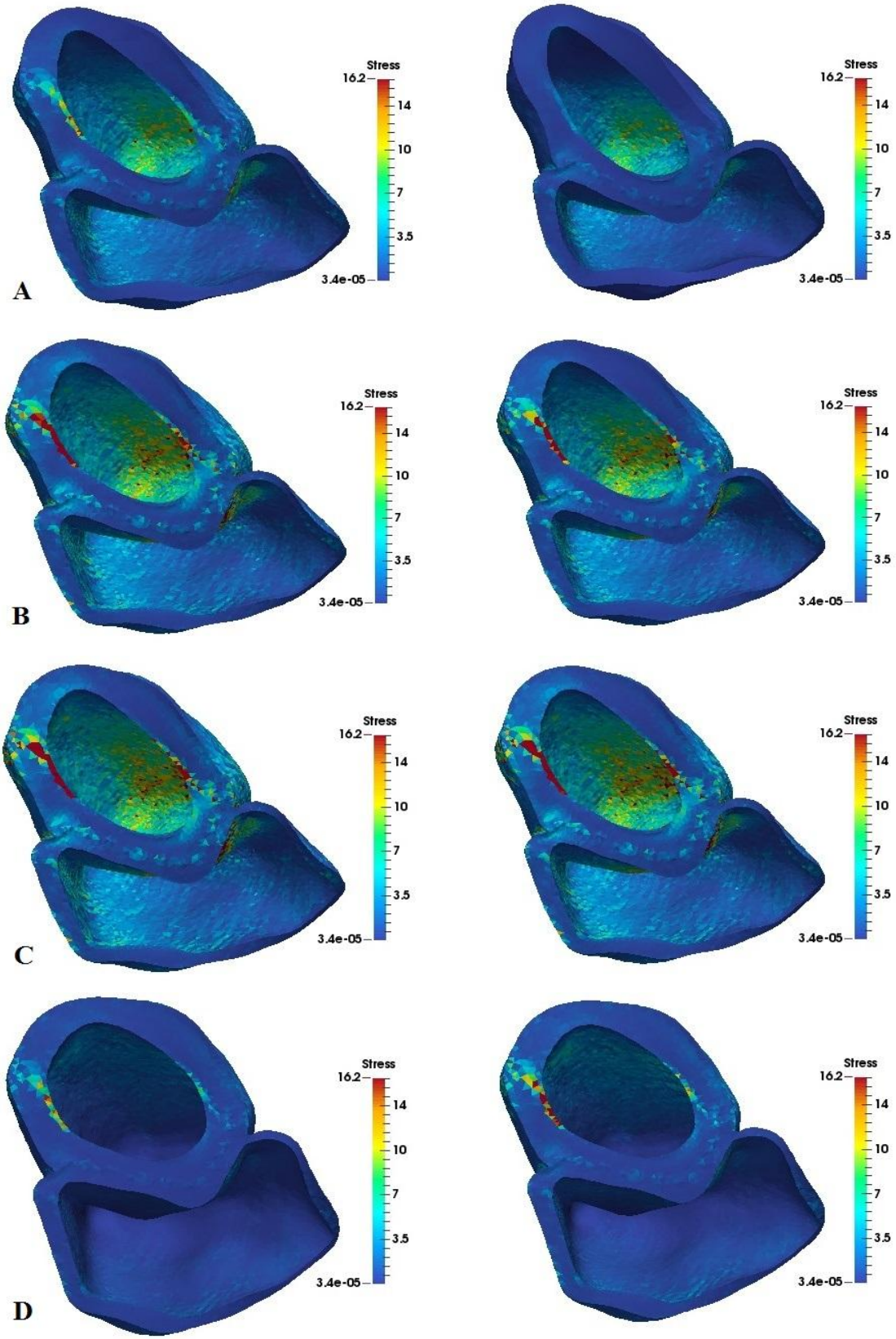

Figure 45: Stress distribution maps of the control on the left and under Na^+ channel blocking on the right at times A) 100 ms, B) 150 ms, C) 200 ms, D) 350 ms

a) Ventricular Volume

The volumes of the left and right ventricles was calculated for the drug influenced model and plotted against the control. The results are shown in Figure 46. Both models exhibit similar trends and reach the same minimum ventricular volumes, but the drug-induced model seems to be lagging behind the control in both the LV and the RV and this lag not only affected the muscle contraction, but the volume restoration is falling behind as well. These results indicate that the ventricular performance has been shifted as a result of the electrophysiology delay.

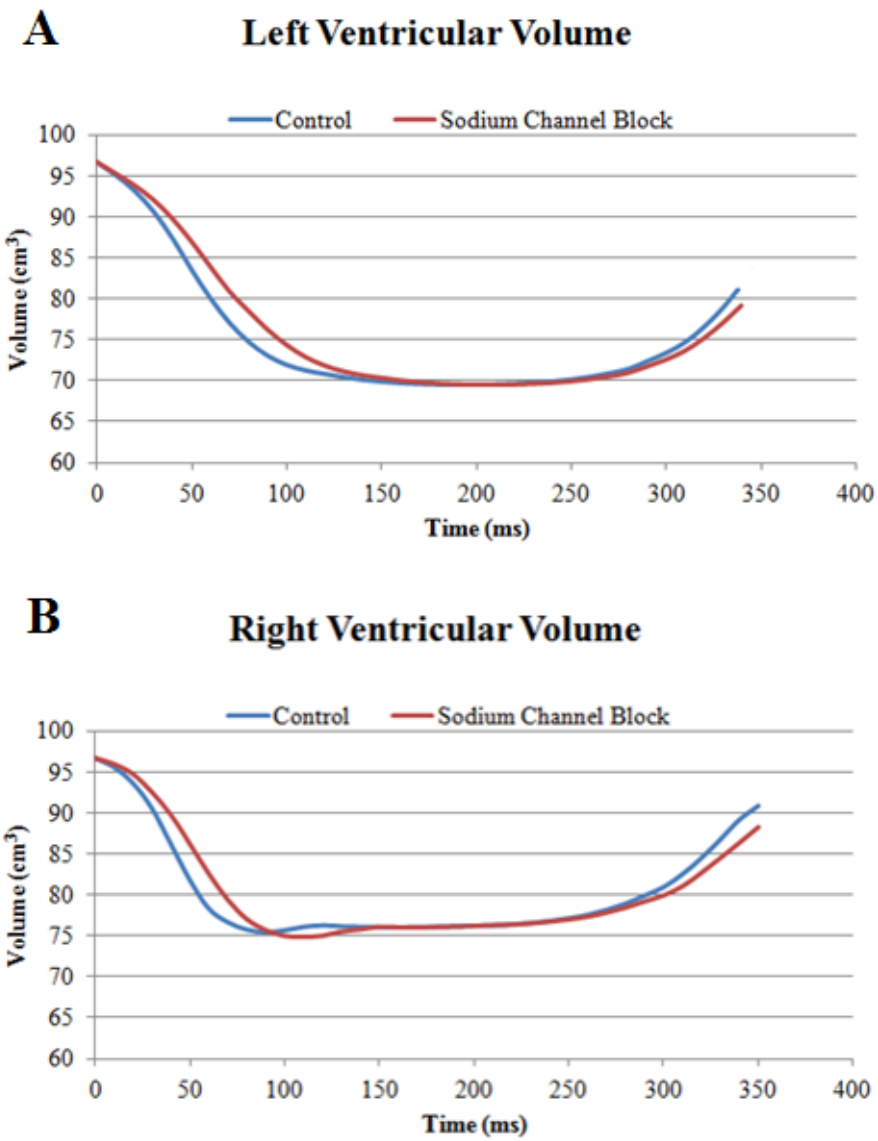

Figure 46: Volume change through time of A) left and B) right ventricles under normal conditions and under IC_{50} dose of Na^+ channel blocker

b) Ejection Fraction

The EFs of the drug induced model were calculated and compared to the control. The results are recorded in Table 4. The LV EF appears to be unaffected while the RV, interestingly, seems to have exhibited an increase in the ejection fraction. As far as we know, these results are new and there are no reports to compare them to.

Table 4: Ejection Fraction values for the control vs. the Na^+ channel blocked model

Control		Sodium Channel Blocker	
LV	RV	LV	RV
28.2%	21.8%	28.2%	22.5%

c) Left Ventricle Twist

The twisting motion of the LV is crucial in the cardiac functionality and risky if compromised. Figure 47 plots the LV twist angle of the drug induced model against the control. As expected, the rate of angle twist decreases as a consequence of the sodium channel block delay. This checks out with the literature.[19] However, the maximum twist angle reached by the LV is higher in the drug induced model reaching almost 17 degrees. This result is also new and unpredicted and the cause of which would make for an interesting study.

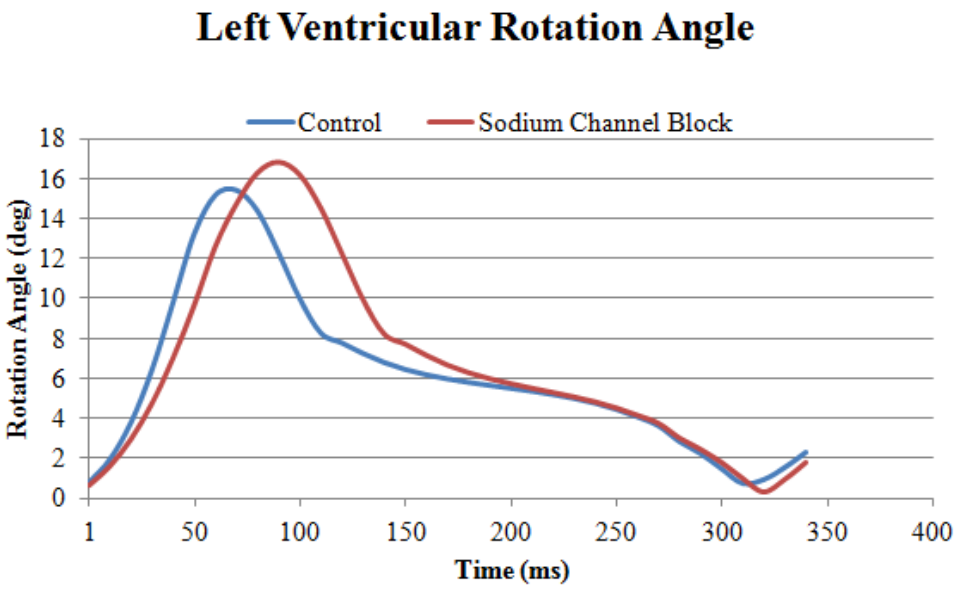

Figure 47: Left Ventricle rotation angle change over time under normal conditions and under IC_{50} dose of Na^+ channel blocker

d) Longitudinal and Radial Strains

As shown in Figure 48, the longitudinal strain measures of the drug influenced model exhibit similar trends to the control, but at a lower rate. The same longitudinal axis shortening during contraction is achieved by both models, but, as predicted by the electrophysiology, the drug influenced model was delayed.[18,19]

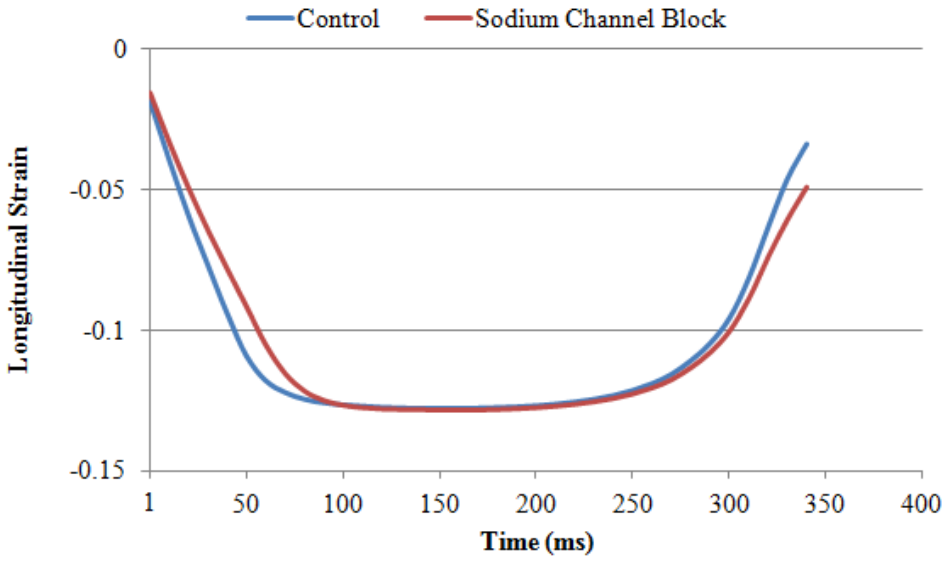

Figure 48: Longitudinal strain under normal conditions and under IC50 dose of Na+ channel blocker

The same delay is experienced in the radial strains as well. However, in both ventricle, except for the stretching in the RV long direction, which is similar to the control, there appear to be a higher percentage of stretching and shortening in the drug induced model. The exact percentages are recorded in Table 5 and the radial strain plots of the LV and RV are shown in Figures 49, 50, 51 and 52. This increased mechanical performance is an unexpected finding and more research is needed to understand its cause and subsequent effect.

Table 5: Radial stretching and shortening of the control and Na+ channel blocked model

Control				Sodium Channel Block			
LV		RV		LV		RV	
Long	Short	Long	Short	Long	Short	Long	Short
24%,	30%	19%	42%	25.8%	32.2%	19%	45.8%

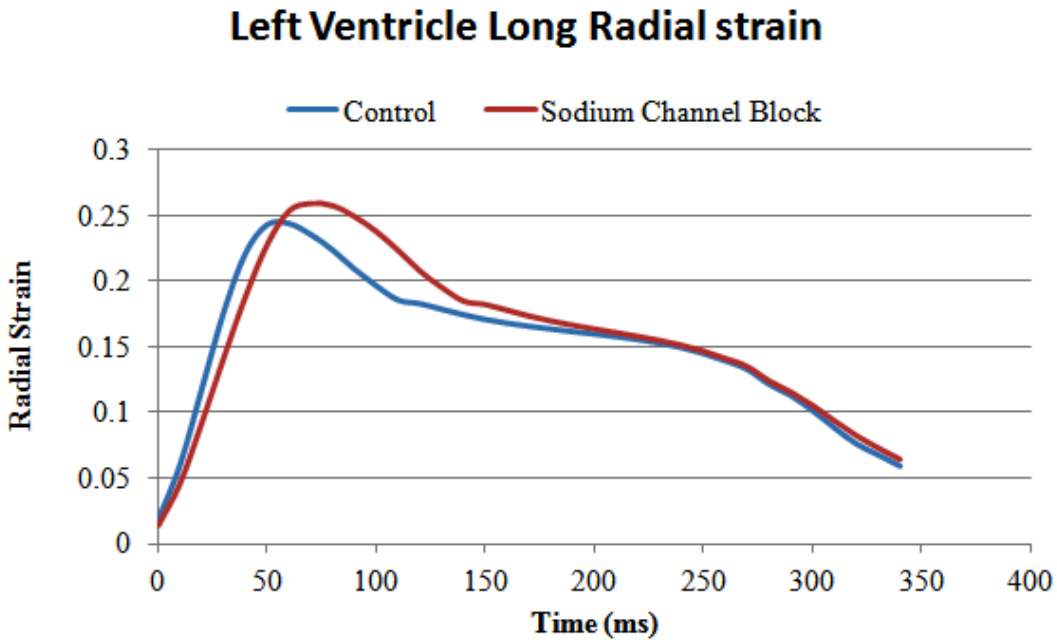

Figure 49: Left Ventricle strain in the long direction for control and Na^{+}channel blocked model

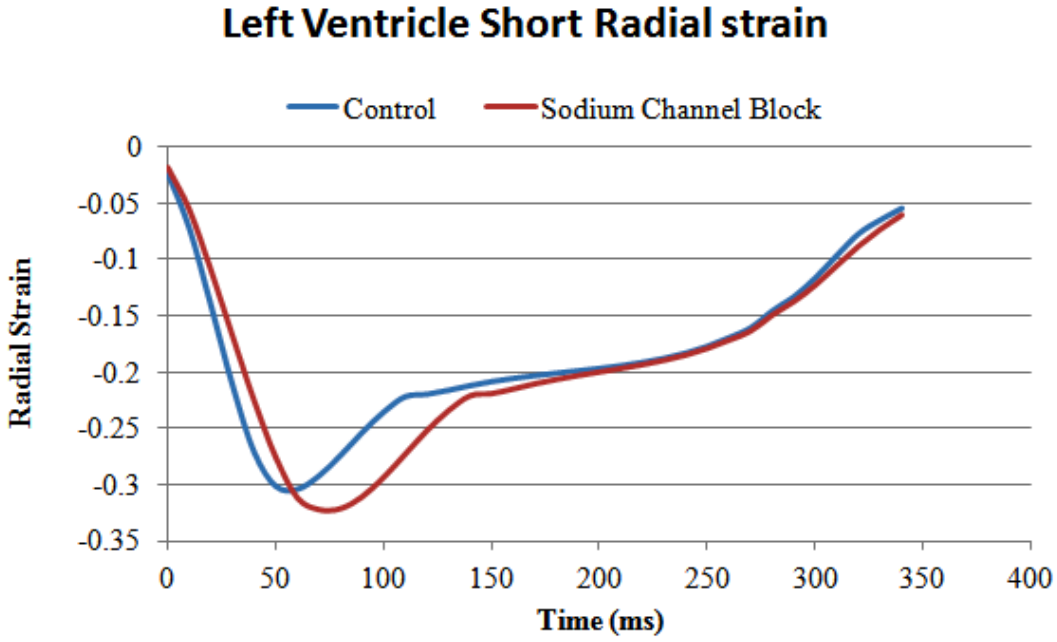

Figure 50: Left Ventricle strain in the short direction for control and Na+channel blocked model

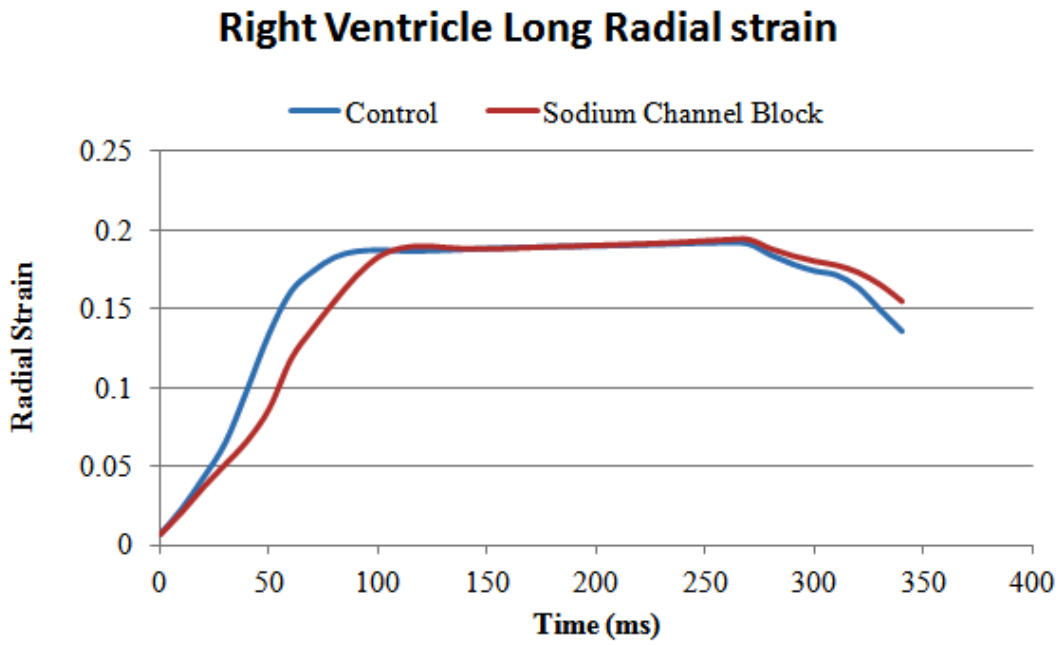

Figure 51: Right Ventricle strain in the long direction for control and Na+channel blocked model

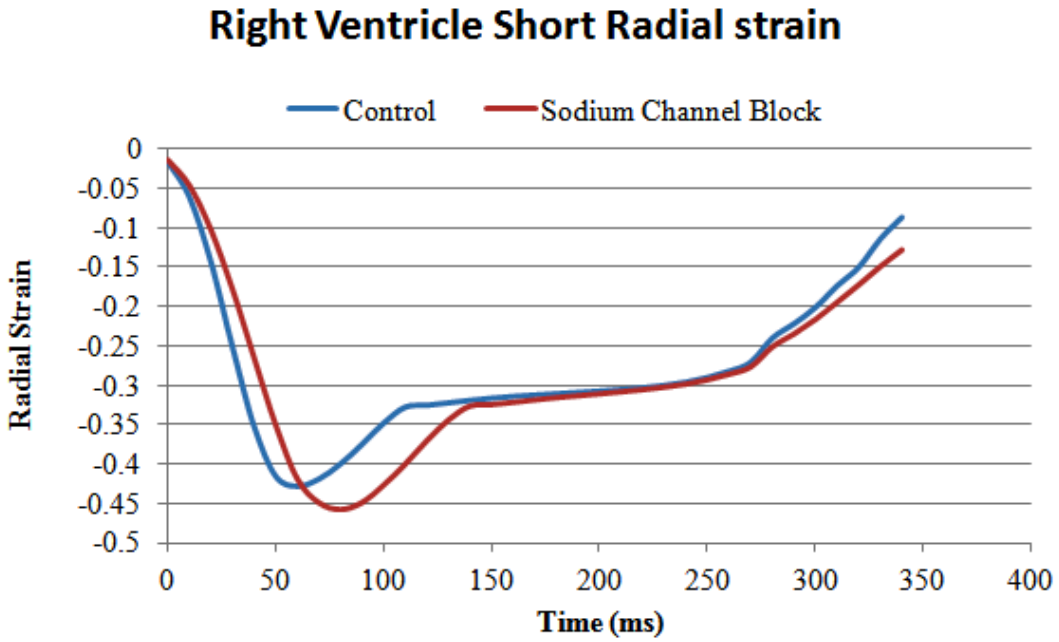

Figure 52: Right Ventricle strain in the short direction for control and Na+channel blocked model

D) Simulation of the effects of Potassium channel blockage

In simulating the effect of potassium channel blockage on the function of the heart, the effect of ultra-small gold nanoparticles of 1.4 nm diameter (Au1.4MS) that are frequently used as drug carriers were chosen as an example drug to investigate. With an IC_{50} value of 48 μM[17] the potassium channel blockage of 100 μM concentration of the drug, using the formula in equation (2.1) causes a blockage of 68%. A simulation was carried out under the same control conditions with 100 μM concentration of Au1.4MS as the potassium channel blocker.

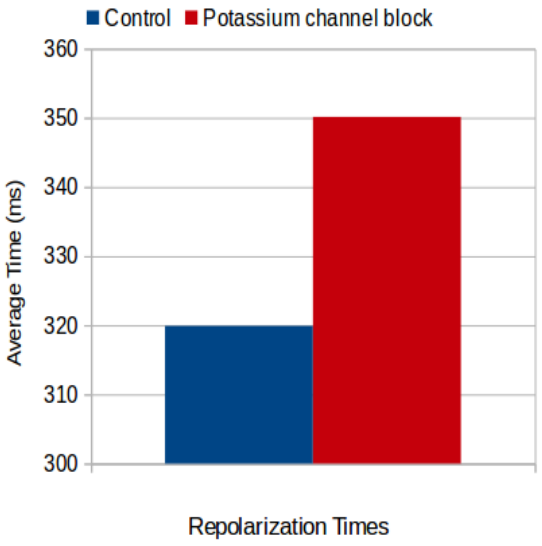

Figure 53: Average repolarization time of the ventricles for control (blue) and for Au1.4MS influence (red)

i) Electrophysiology

Figure 53 shows the difference in repolarization time of about 30 ms between the control simulation and AuNP-influenced simulation. A side by side comparison of the 2 simulations at time 300 ms during repolarisation shows the control simulation ahead of the drug influenced once is shown in Figure 54. These results are a good match to reports in literature.[26]

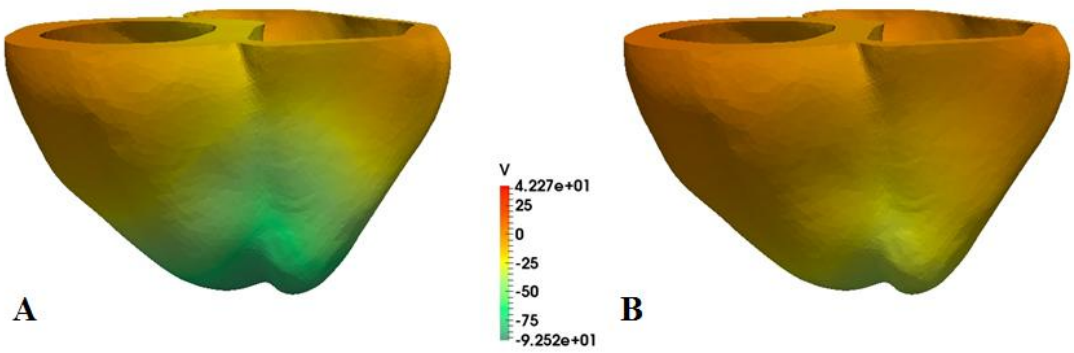

Figure 54: Repolarization of the ventricular mesh tissue of A) control and B) AuNP-influenced simulations

The pseudo-ECG of the potassium channel blocking simulation in Figure 55 does not show difference from the control during the depolarization in the QRS complex. The change can be observed in the increase in the QT interval and the lower T-wave amplitude due to decreased dispersion during repolarization similar to changes reported in literature.[44,98]

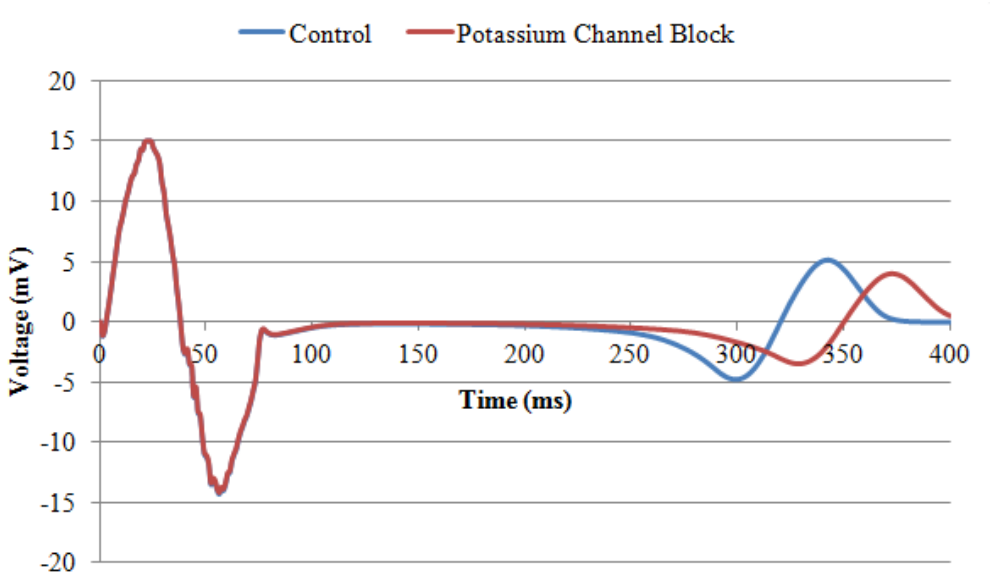

Figure 55: Pseudo-ECG QT interval for control (blue) and for Au1.4MS influence (red)

In Figure 56, the AP plot comparing the results of the control and potassium channel blocker, shows the activation in both cases as almost exactly the same. The deviation can be seen during the repolarization phase of the action potential as potassium channel blockage leads to delayed repolarization and increase in action potential duration. The results appear to be consistent with reports in literature.[44,98]

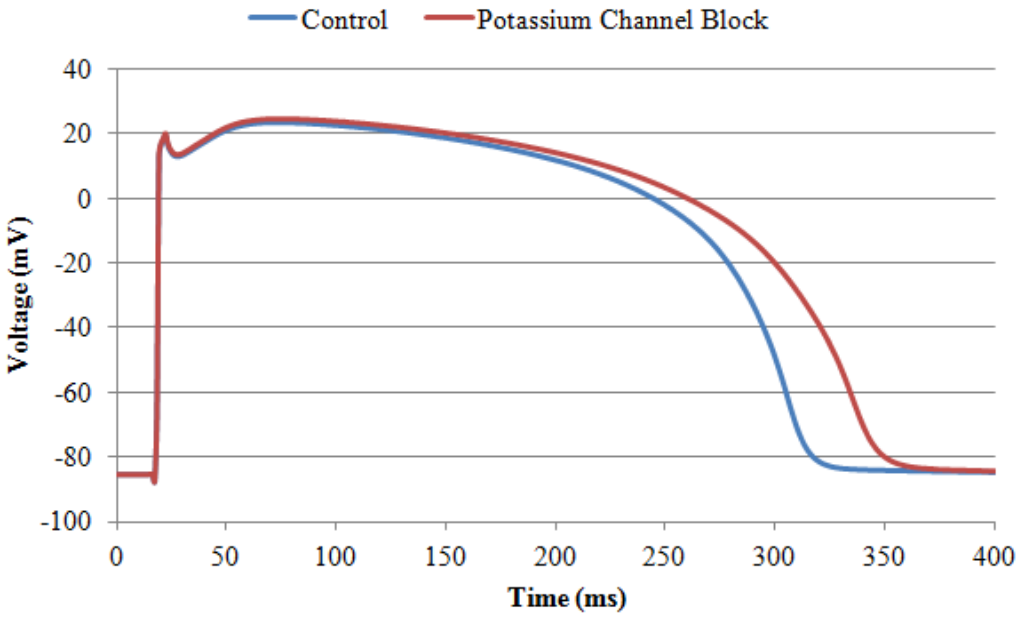

Figure 56: Action potential for control (blue) and for Au1.4MS influence (red)

Repolarization time maps for the ventricular model in Figure 57 show the effect of the potassium channel blocker on the tissue repolarization time. The color gradient in Figure 57A shows the maximum time for tissue repolarization under normal conditions is 391 ms while in Figure 57B under nanodrug influence, the same tissue repolarization time reaches 397 ms. The simulation results are as such consistent with findings in literature regarding the effect of potassium channel blockers on the action potential duration prolongation due to the decreased rate of ventricular tissue repolarization.[26]

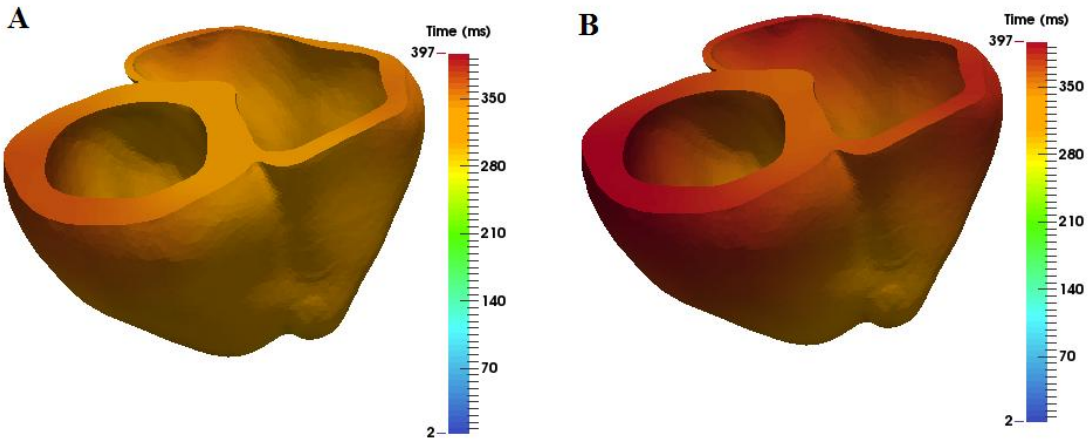

Figure 57: Repolarization time maps of the ventricular mesh under A) normal conditions and B) the influence of potassium channel blocker

ii) Tissue Deformation

Figure 58 shows the ventricular mesh at the end of the simulation near the end of the cardiac cycle in the control and the AuNP-influenced models. From the electrophysiological results, potassium channel blockers are known to cause repolarization delay.[44] Therefore, differences between the behavior of the control and the AuNP-induced model should begin to appear near the end of the simulation during ventricular relaxation. There does not appears to be any visual difference between them the 2 models in Figure 58.

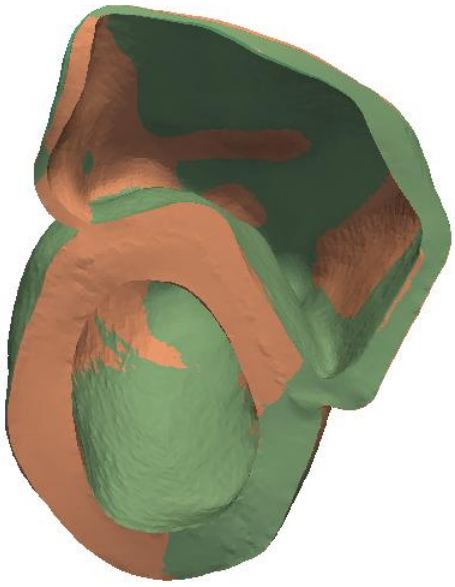

Figure 58: Ventricular contraction of the control (solid pink) vs. K+ channel blocked model (translucent green)

The effective deviatoric strain and the effective deviatoric stress maps of the AuNP-induced model are shown in Figures 59 and 60, respectively, in comparison with the control model. The stress and strain color distributions do not show any difference between the two models either. According to electrophysiological findings,[44] the results are expected to remain identical for about 250 ms after which change is expected, but so far doesn't appear. The other biomarkers are needed to shed more light on the AuNP-influenced mechanical behavior of the heart.

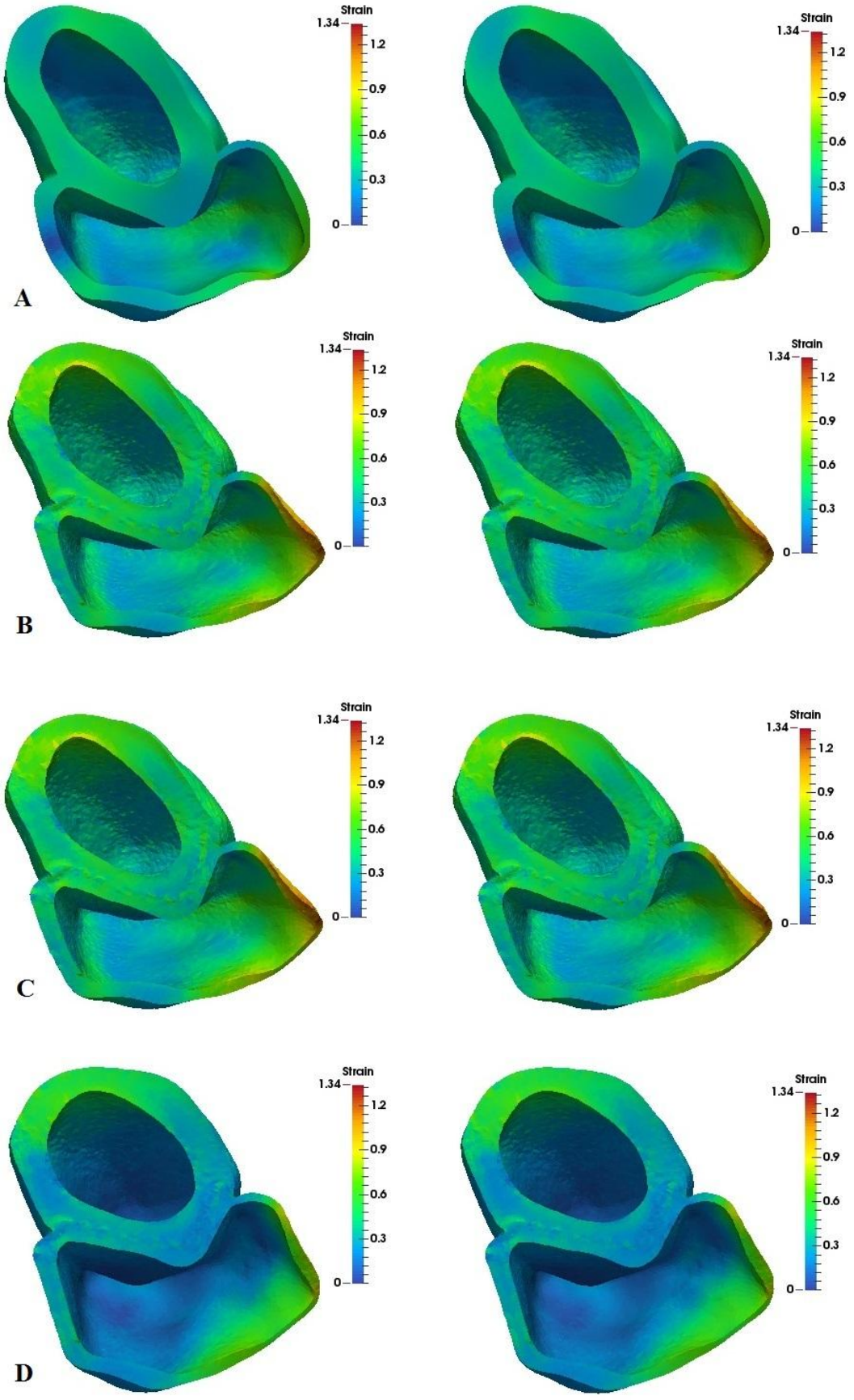

Figure 59: Strain distribution maps of the control on the left and under K^+ channel blocking on the right at times A) 50 ms, B) 150 ms, C) 250 ms, D) 350 ms

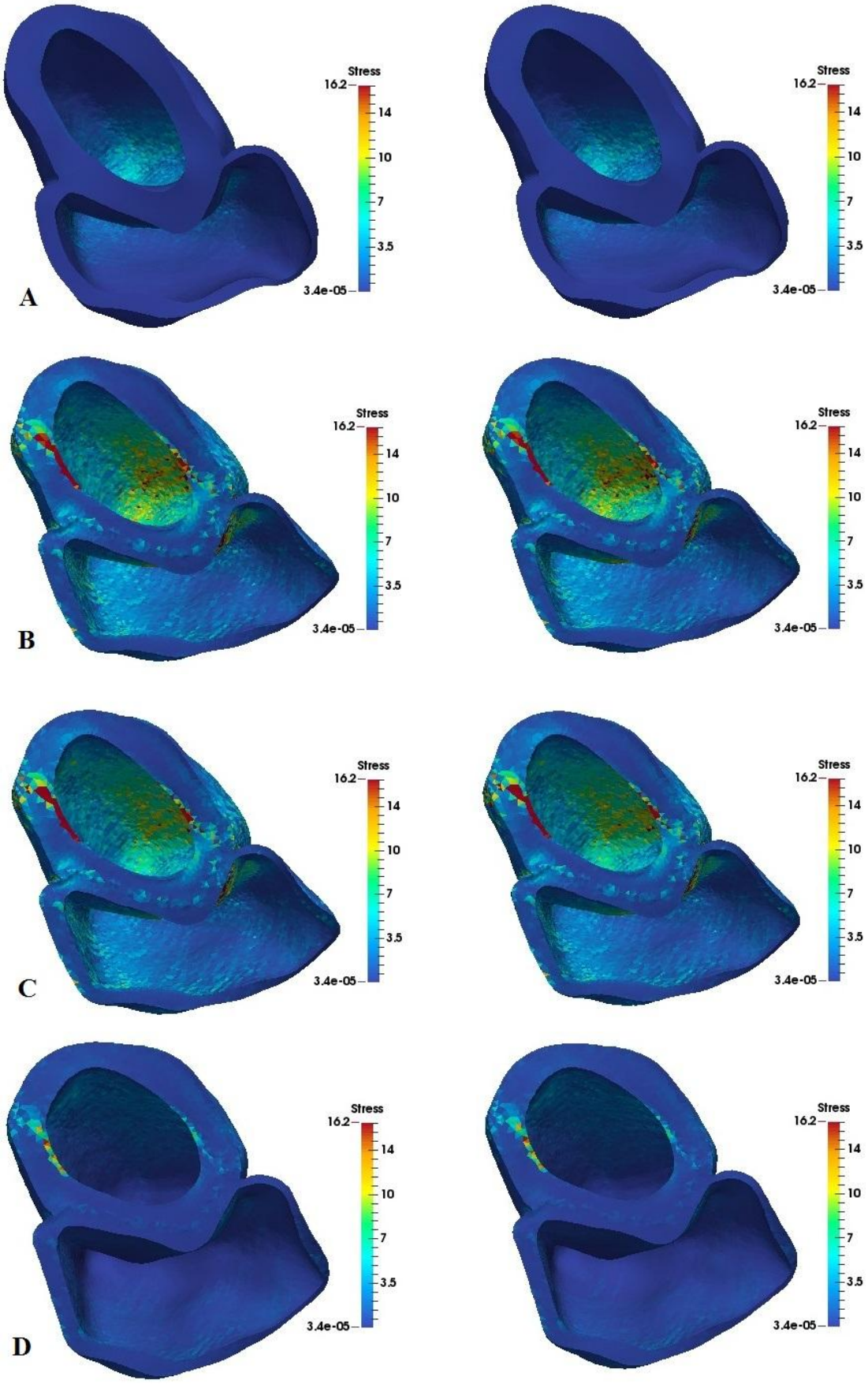

Figure 60: Stress distribution maps of the control on the left and under K^+ channel blocking on the right at times A) 50 ms, B) 150 ms, C) 250 ms, D) 350 ms

a) Ventricular Volume

The left and right ventricular volumes were calculated at each time step and compared to the control volume measurements. The plots are shown in Figure 61. The volume change in the LV is exactly the same in both the control and the AuNP-induced model. As for the RV volume, there appears to be an extremely slight change between the 2 models at the very last simulation time step. Other than that, the volume change is identical. The ventricular volume restoration was expected to slow down as the repolarization in the AP slows down[26], but that effect did not appear.

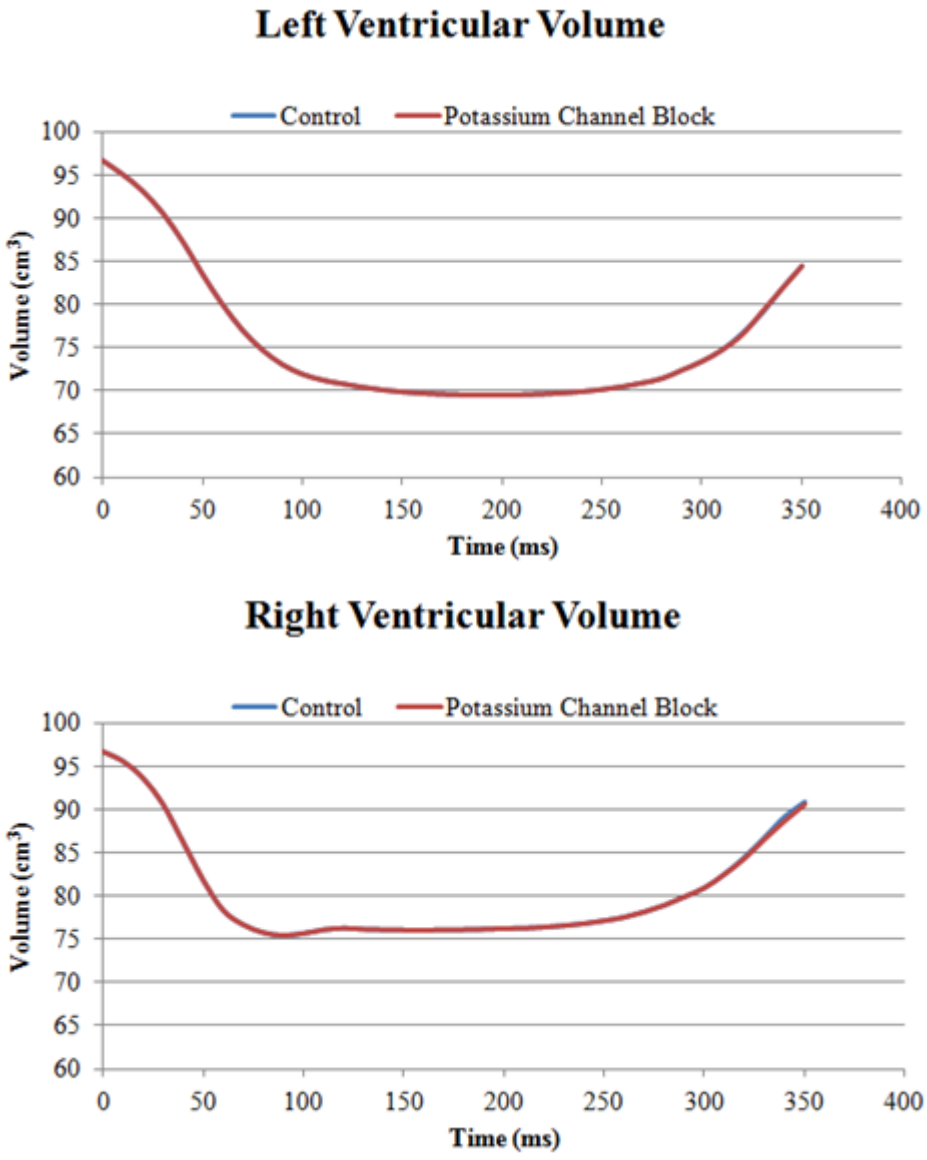

Figure 61: Volume change through time of A) left and B) right ventricles under normal conditions and under K^+ channel blocker

b) Ejection Fraction

The EF is not a suitable biomarker for potassium channel blockage as it does not affect the activation[26] and therefore does not affect systole. Since there is no volume change between the 2 models, the EF of the AuNP-induced model is identical to the control. The values are shown in Table 6.

Table 6: Ejection Fraction values for the control vs. the K^+ channel blocked model

Control		Potassium Channel Blocker	
LV	RV	LV	RV
28.2%	21.8%	28.2%	21.8%

c) Left Ventricle Twist

Again, the twist angles of the drug-induced model are the same as the control which is as expected since the twist occurs near the beginning of the cycle where the potassium channel block shows no effect on the electrophysiology.[26,44] However, between the times 300 ms and 350 ms, a small change starts to appear between the 2 models, as seen in Figure 62.

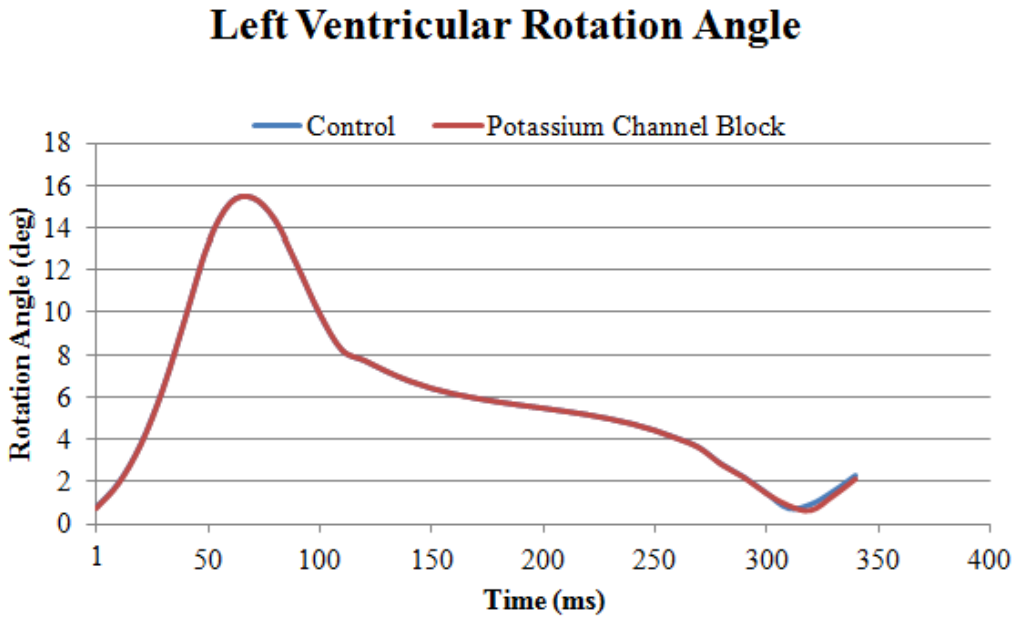

Figure 62: Left Ventricle rotation angle change over time under normal conditions and under K^+ channel blocker

d) Longitudinal and Radial Strains

Figure 63 plots the longitudinal strain of the drug induced model against the control. The LV and RV radial strains are plotted as well in Figures 64, 65, 66 and 67. The strains shows the same behavior of the other biomarkers where the results are identical to the control. Again this is unexpected. More visible differences were expected to appear near the end of the cycle such as a slower rate of recovery.

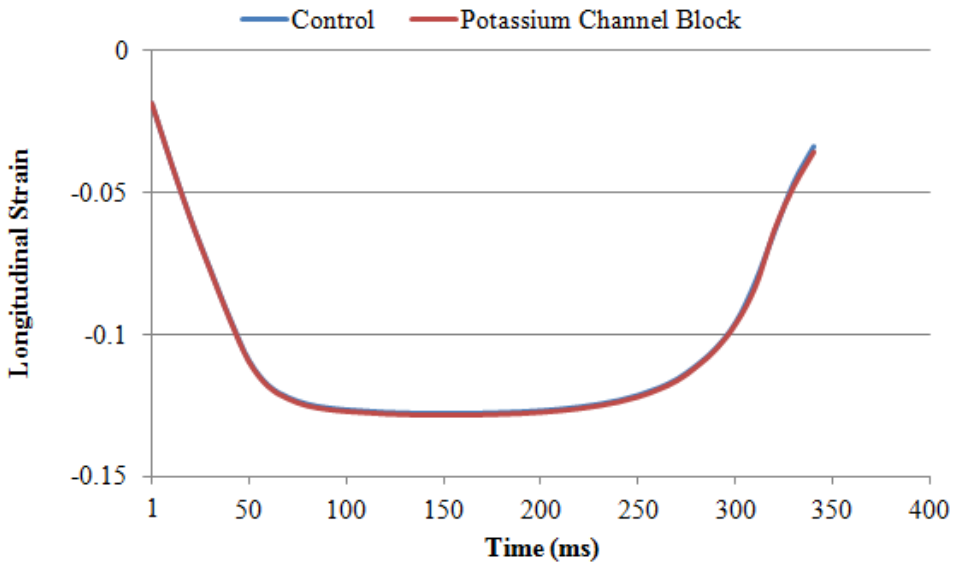

Figure 63: Longitudinal strain under normal conditions and under K^+ channel blocker

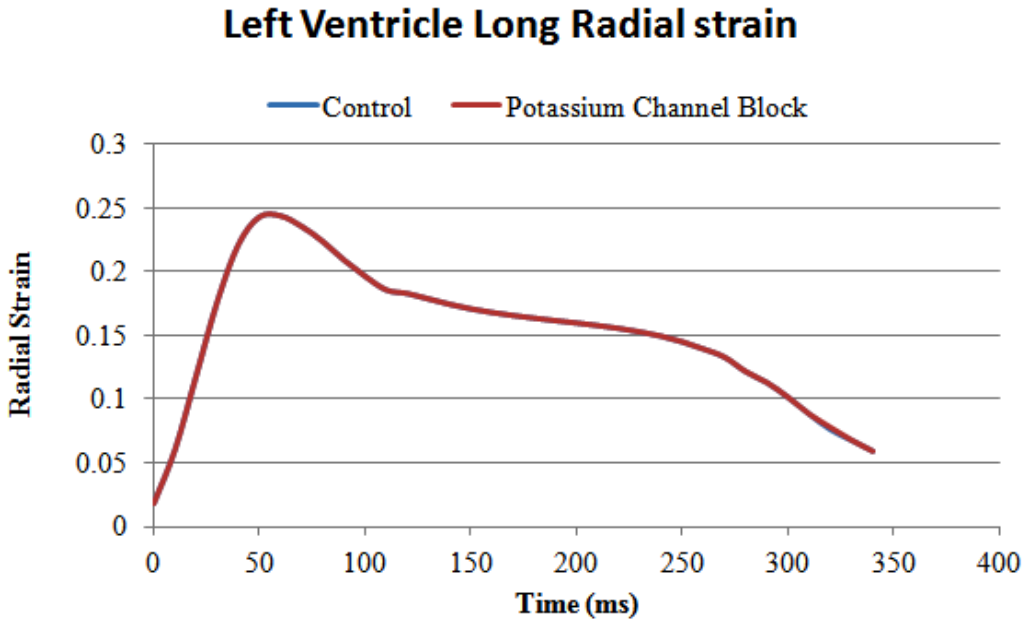

Figure 64: Left Ventricle strain in the long direction for control and K^+ channel blocked model

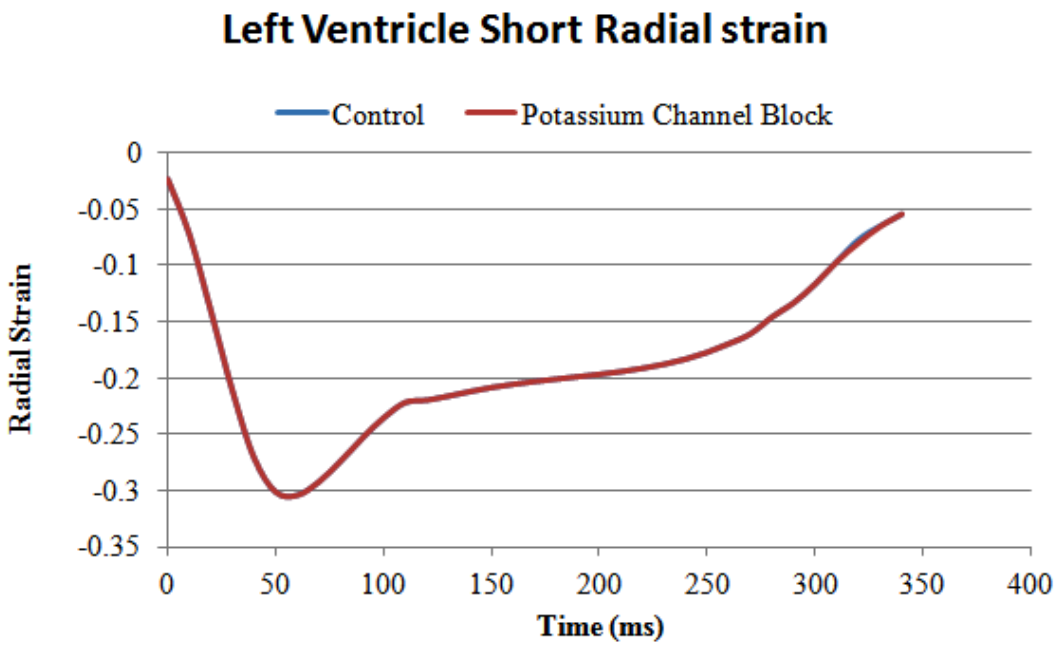

Figure 65: Left Ventricle strain in the short direction for control and K^+ channel blocked model

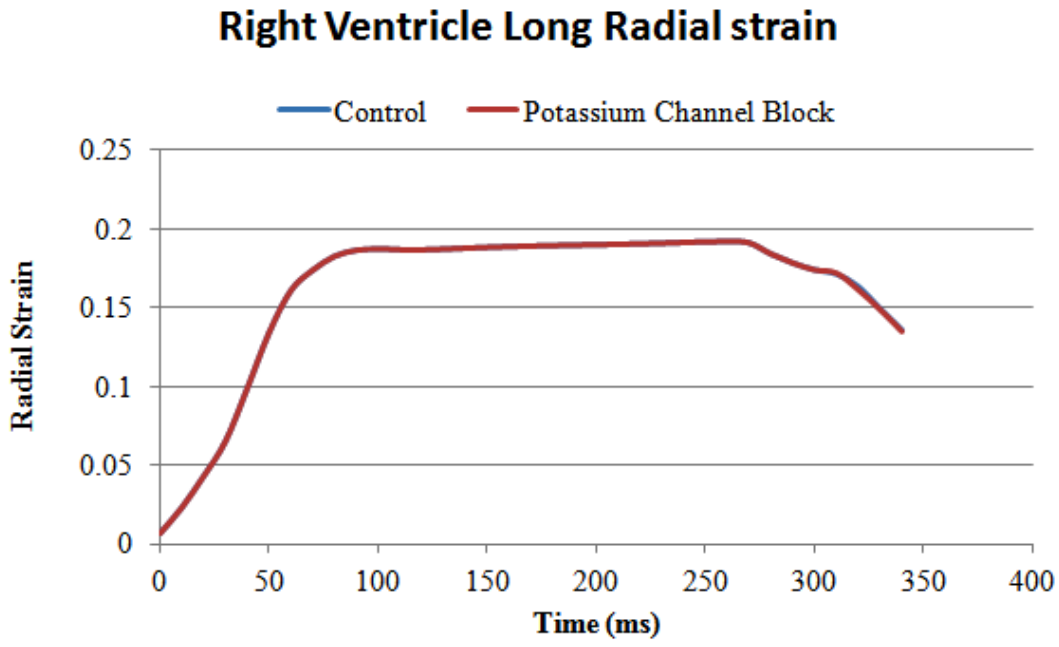

Figure 66: Right Ventricle strain in the long direction for control and K^+ channel blocked model

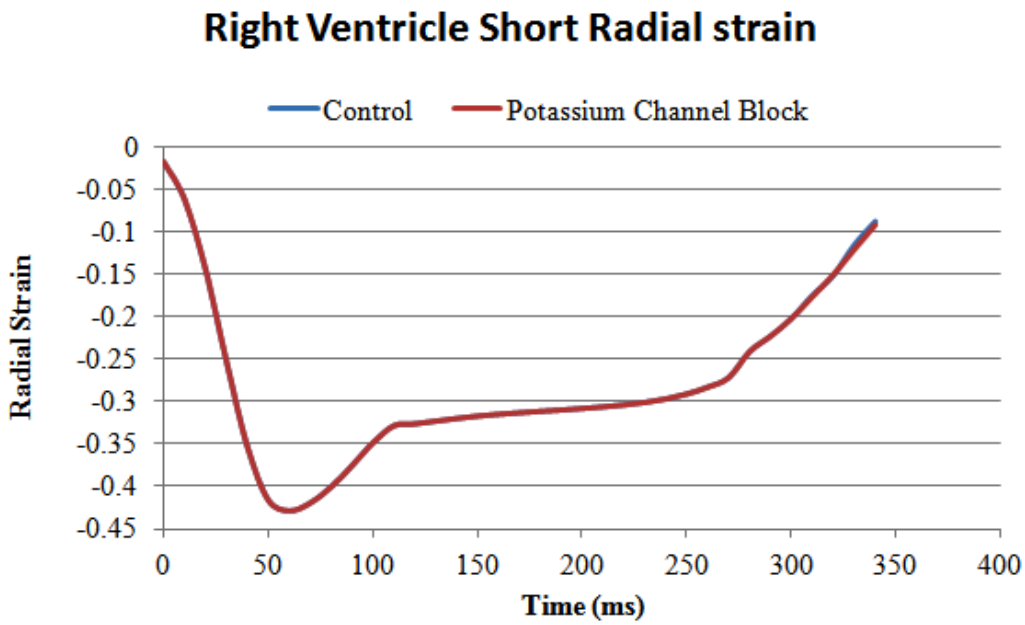

Figure 67: Right Ventricle strain in the short direction for control and K^+ channel blocked model

Potassium channel blockers are known to affect the final (repolarization) phase of the cardiac cycle. So its behavior being identical to the control is expected in the first half or two thirds of the cycle. As expected, there was no change in the EF or the maximum LV twist angle as these two biomarkers are systole quantifying biomarkers. The differences were expected to be seen in the restoration curves of the volume and strain plots. The differences were expected to appear at around the same time they appear in the electrophysiology which is at 250 ms. That did not happen and only very slight changes appeared in some cases at the very end of the simulation. The most likely reason it is late in showing compared to electrophysiology is that the mechanical deformation is slow to respond to electrical excitation. The fact that only 350 ms of the cycle are available in this study is a shortcoming since the effect may appear in the last 50 ms and pass over into the next cycle.

E) Simulation of the effects of Calcium channel blockage

Calcium dynamics form the link between electrical activation and mechanical contraction[63] since the generation of the active tension depends on intracellular calcium concentration as previously mentioned.[60] The L-type calcium channel is a pathway found in all cardiac cell membranes and is the principle pathway of calcium into the cell.[2] The blockage of L-type calcium channel has been known to cause reduction in the T-wave amplitude and shortening in the QT interval caused by the reduction of the action potential duration.[42] Drugs that cause calcium channel blocking have many clinical applications such as reducing blood pressure and altering heart rate.[42] A simulation was carried out under the influence of the IC_{50} dose of a calcium channel blocker using the same control conditions and the results are shown below.

i) Electrophysiology

Figure 68 shows the difference in average repolarization times between the control and under the influence of a calcium channel blocker. The plot shows the simulation with the calcium channel blocker repolarizing about 50 ms ahead of the control simulation.

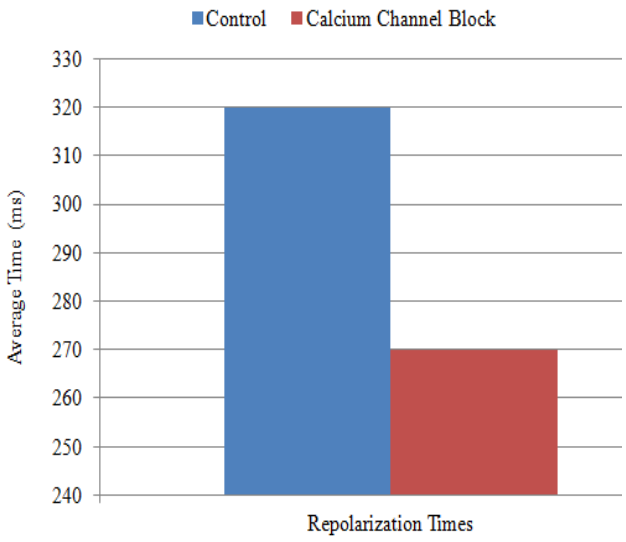

Figure 68: Average repolarization time of the ventricles for control (blue) and for IC_{50} dose of a calcium channel blocker (red)

Figure 69 shows a side by side comparison of the electrical potential of the two simulations at time 300 ms during repolarization. The images show the repolarization of the drug-influenced simulation to be clearly ahead of the control. These results are consistent with findings in literature.[42]

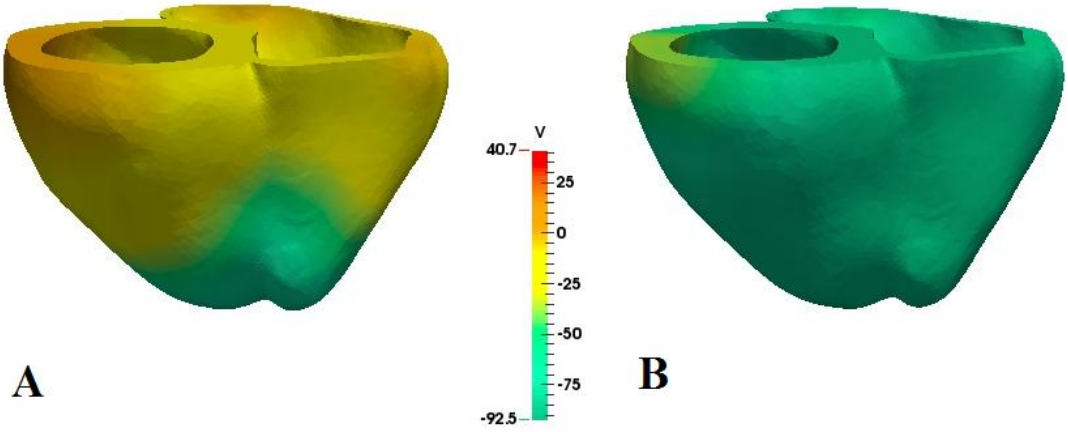

Figure 69: Repolarization of the ventricular mesh tissue at time 300 ms of A) control and B) calcium channel blockage

The effect of blocking L-type calcium channel on the pseudo-ECG is plotted against the control in Figure 70. The drug barely affects the QRS complex with only a very small decrease its amplitude. The T-wave, however, experiences a significant shift backwards leading to shortening of the QT interval. There is also a slight decrease in the T-wave amplitude. These alterations in the QT interval match those reported in literature.[42]

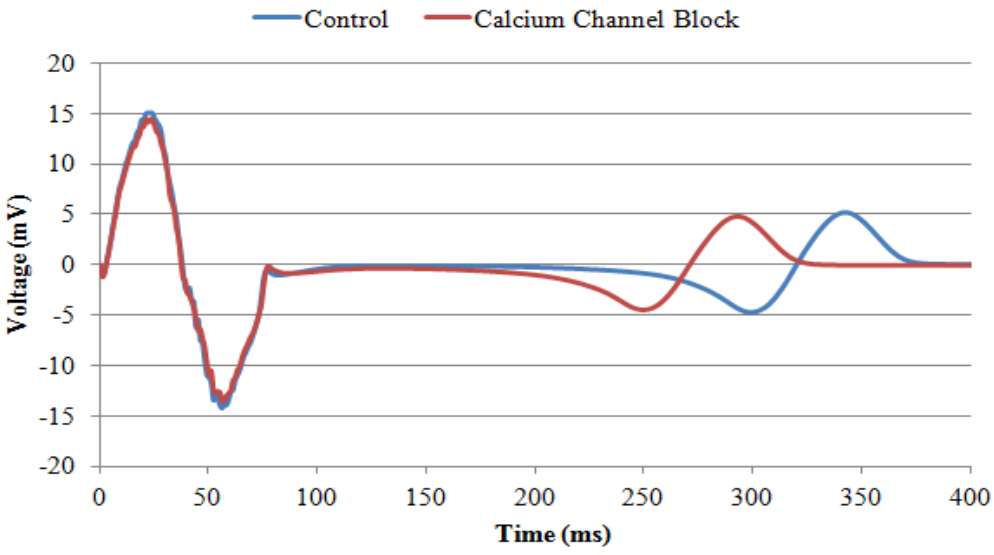

Figure 70: Pseudo-ECG QT interval for control (blue) and for IC_{50} dose of a calcium channel blocker (red)

The action potential plot comparing the control simulation with the simulation under the influence of a calcium channel blocker is shown in Figure 71. The activation of both appear to be almost the same except for a slight reduction in amplitude of the drug-influenced simulation. A more significant difference appears in the plateau and repolarization phases. There is a reduction in the voltage at the plateau phase and early repolarization for the drug-influenced simulation which agree with reports in literature.[99]

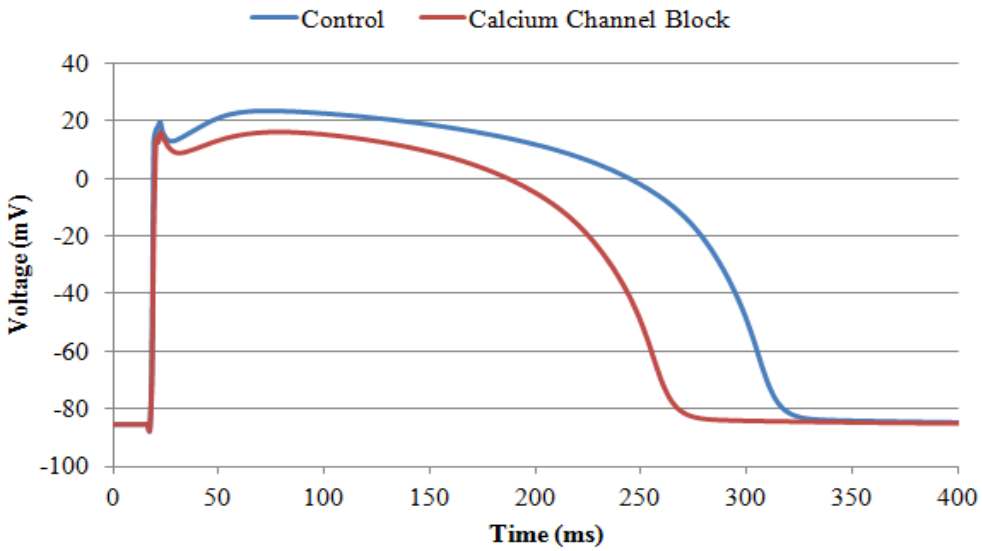

Figure 71: Action potential for control (blue) and for IC_{50} dose of a calcium channel blocker (red)

Repolarization time maps for the ventricular model shown in Figure 72 show the effect of L-type calcium channel blocking on the tissue repolarization time. The color gradient in Figure 72A shows the maximum time for tissue repolarization under normal conditions is 368 ms while in Figure 72B under drug influence, the same tissue repolarization time reaches only 318 ms.

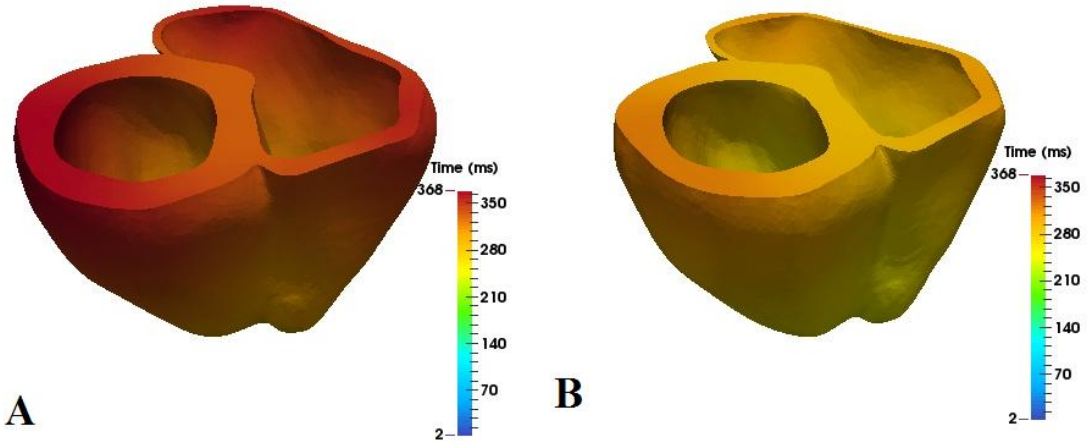

Figure 72: Repolarization time maps of the ventricular mesh under A) normal conditions and B) the influence of calcium channel blocker

All the electrophysiological simulation results are as such consistent with findings in literature regarding the effect of L-type calcium channel blockers on the action potential duration shortening due to early repolarization.[42,99]

iii) Tissue Deformation

The electrophysiological simulations indicate that the calcium channel blocked model should repolarize and reach the end of the cardiac cycle 50 ms before the control. This means that the nanodrug induced model should be relaxing much faster than the control. That, however, does not seem to be the case in Figure 73 which shows the superimposed ventricular models of both the control and the calcium channel blocked model. There doesn't appear to be any visible difference between the relaxation of the two models.

Figure 73: Ventricular models of the control (solid pink) vs. Ca^{2+} channel blocked model (translucent green)

The comparison between the effective deviatoric strain and the effective deviatoric stress maps of the L-type calcium channel blocked model and the control are shown in Figures 74 and 75, respectively. The stress and strain color distributions do not show differences between the two models either. According to electrophysiological findings,[42] differences are expected to appear in the results, at least during diastole, but so far there are none. Further mechanical biomarkers are needed to shed light on the calcium channel blocking nanodrugs' influence on mechanical behavior of the heart.

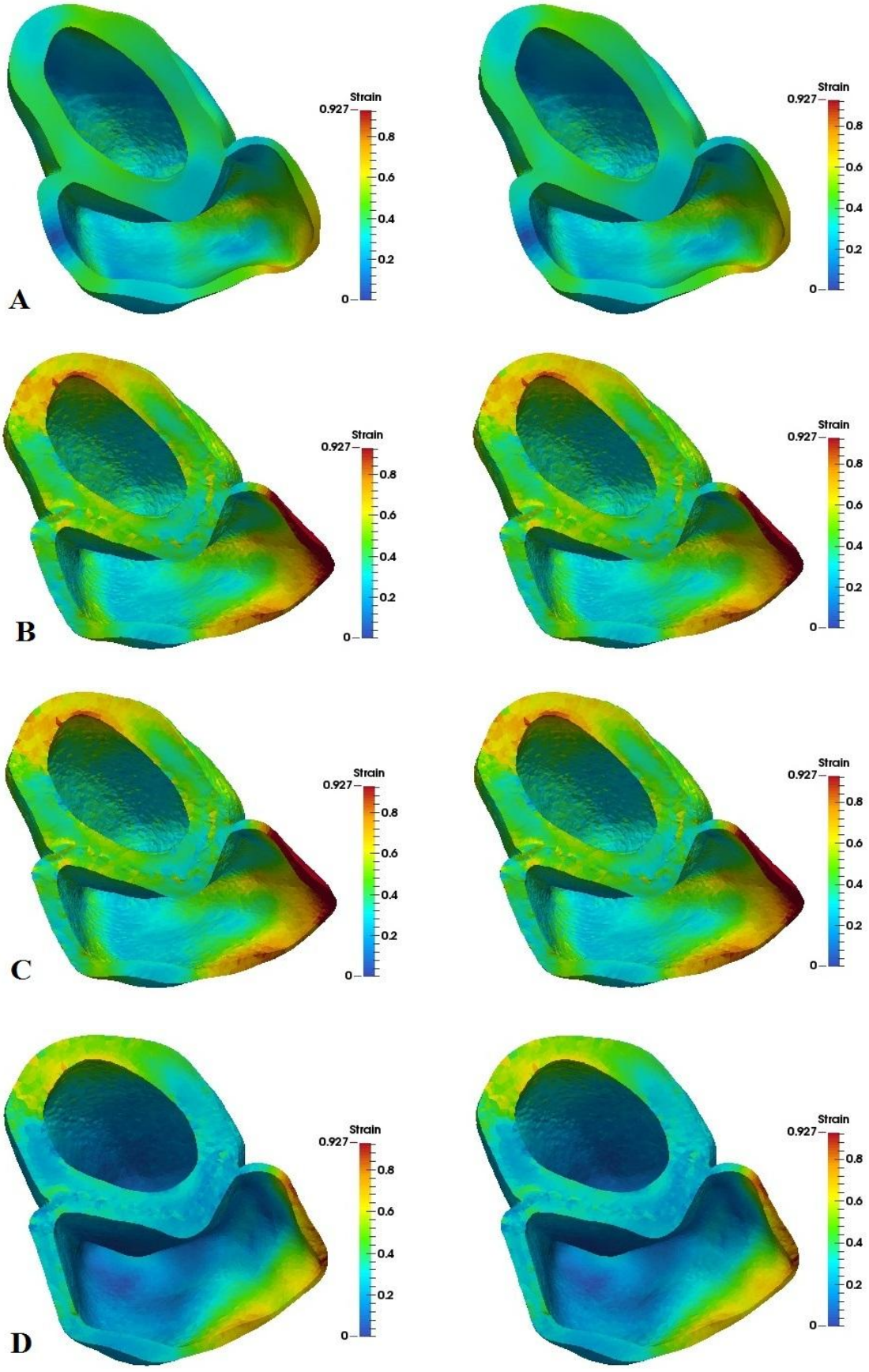

Figure 74: Strain distribution maps of the control on the left and under Ca^{2+} channel blocking on the right at times A) 50 ms, B) 150 ms, C) 250 ms, D) 350 ms

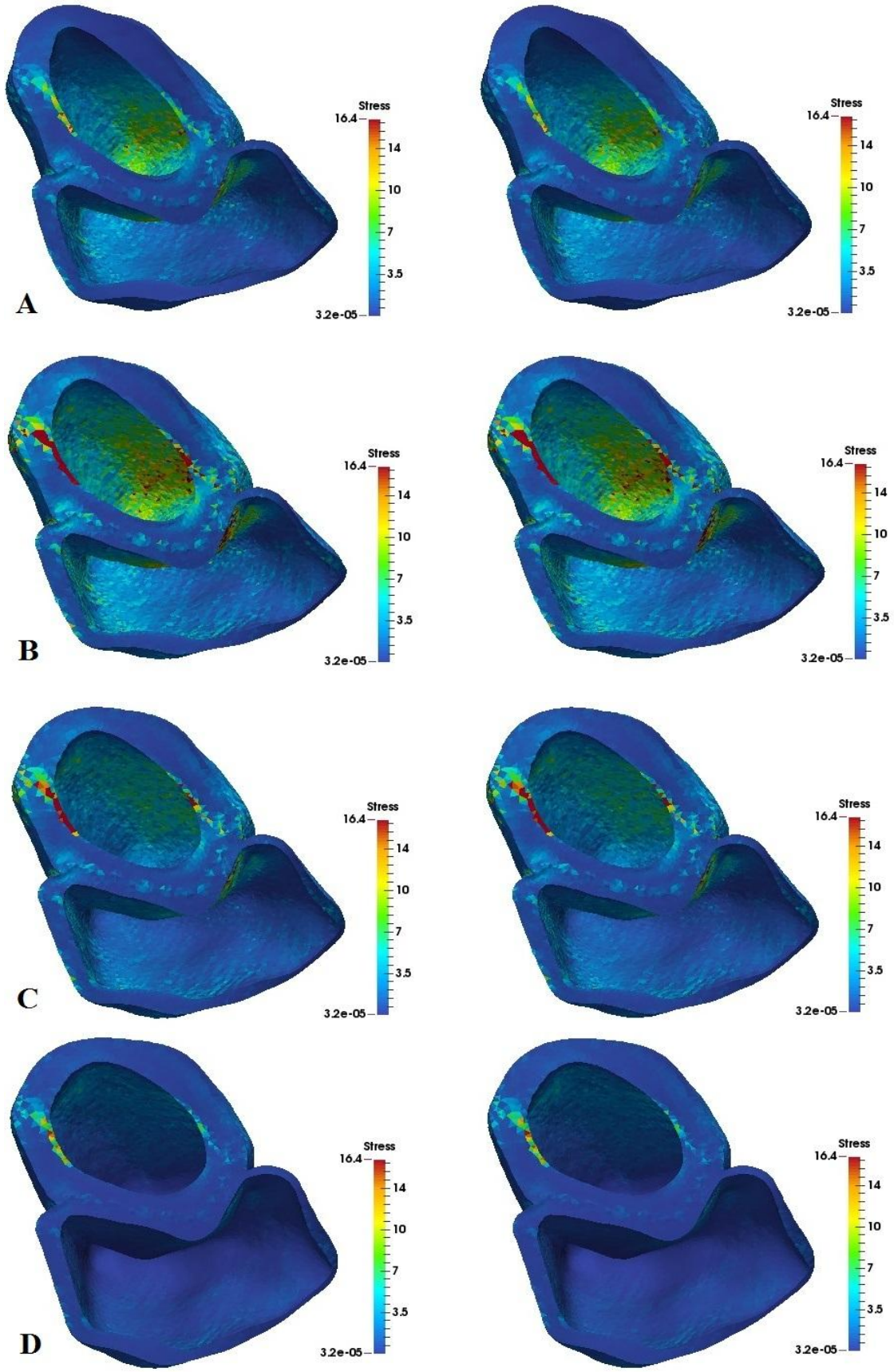

Figure 75: Stress distribution maps of the control on the left and under Ca^{2+} channel blocking on the right at times A) 50 ms, B) 150 ms, C) 250 ms, D) 350 ms

a) Ventricular Volume

The left and right ventricular volumes were calculated at each time step and compared to the control volume measurements with the results plotted in Figure 76. The volume change in the LV and the RV are similar in both the control and the nanodrug-induced model. Reports in literature[42,99] and the electrophysiological results of the simulation support the expectation that the ventricular volume for the calcium channel blocked model was to be restored faster than the control. The direct link between the calcium concentration and the ventricular mechanical response[60] also supports the claim that the blocking the calcium channel would have a significant effect on the volume change. However, neither of these expectations occurred in the volume change of both models.

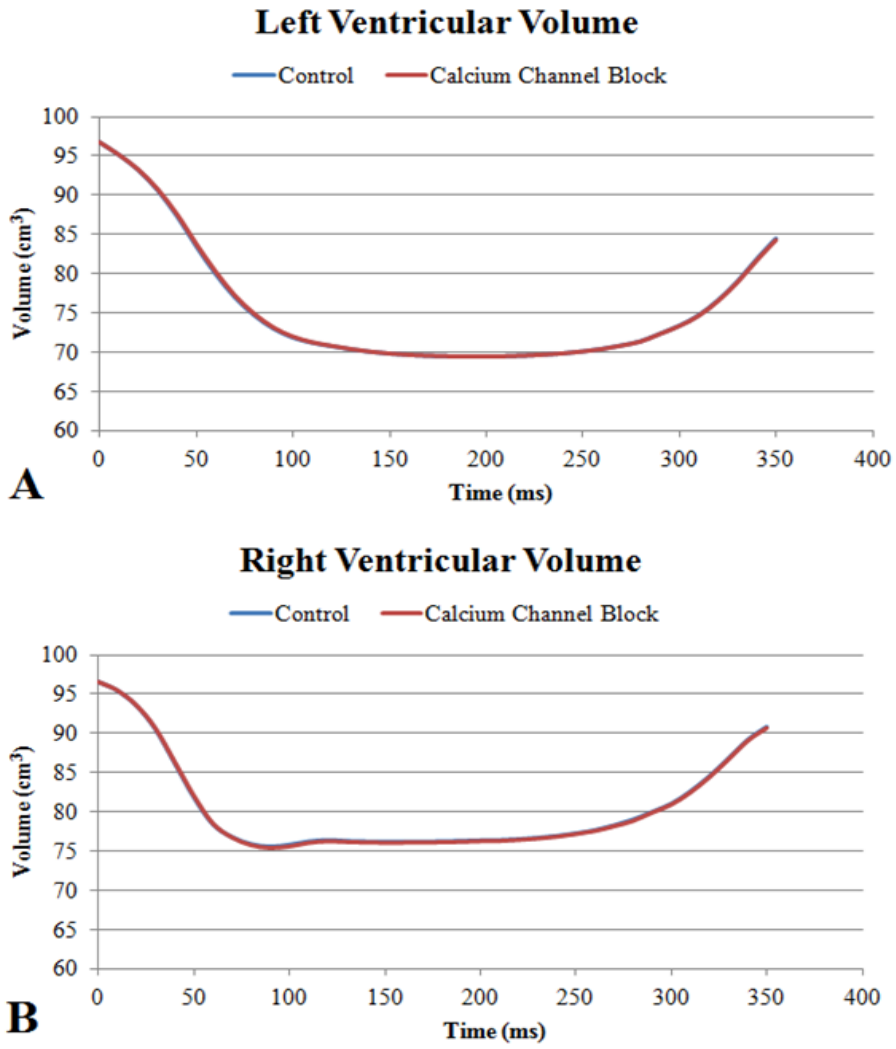

Figure 76: Volume change through time of A) left and B) right ventricles under normal conditions and under Ca^{2+} channel blocker

b) Ejection Fraction

Since calcium channel blocking with an IC_{50} dose did not affect ventricular contraction in our simulation of a single cardiac cycle,[60] no difference was predicted between the control and the nanodrug-induced EFs. There appears to be a very slight increase in the EF of the RV in the nanodrug-influenced model; however, we deem it too small to have significance in the simulated cycle. The values are given in Table 7.

Table 7: Ejection Fraction values for the control vs. the Ca^{2+} channel blocked model

Control		Calcium Channel Blocker	
LV	RV	LV	RV
28.2%	21.8%	28.2%	21.9%

c) Left Ventricle Twist

As shown in Figure 77, the calcium channel block does not appear to have any significant effect on the LV twist angle value. Neither was the LV twisting restored faster in the model under the nanodrug influence, nor was the twisting strength affected by the change in the calcium concentration.

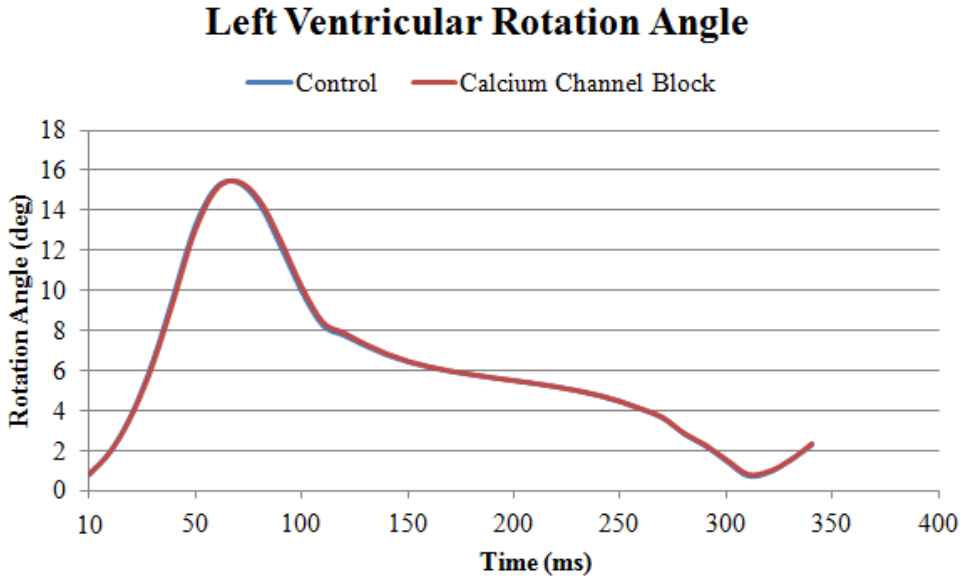

Figure 77: Left Ventricle rotation angle change over time under normal conditions and under Ca^{2+} channel blocker

d) Longitudinal and Radial Strains

The longitudinal strain of the calcium channel blocked model against the control is plotted in Figure 78. The LV and RV radial strains are plotted as well in Figures 79, 80, 81 and 82. The behavior of the strains is similar to the behavior of the other biomarkers with the results similar to the control. Contrary to the reported results, visible differences were expected to appear during the cycle due to the change in the calcium concentration and the strain values were expected to be restored faster.[42, 60]

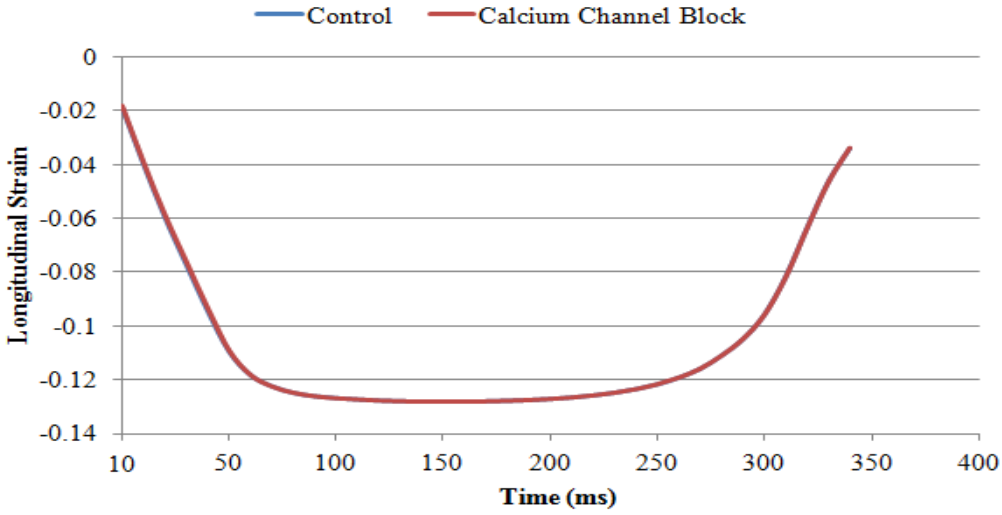

Figure 78: Longitudinal strain under normal conditions and under Ca^{2+} channel blocker

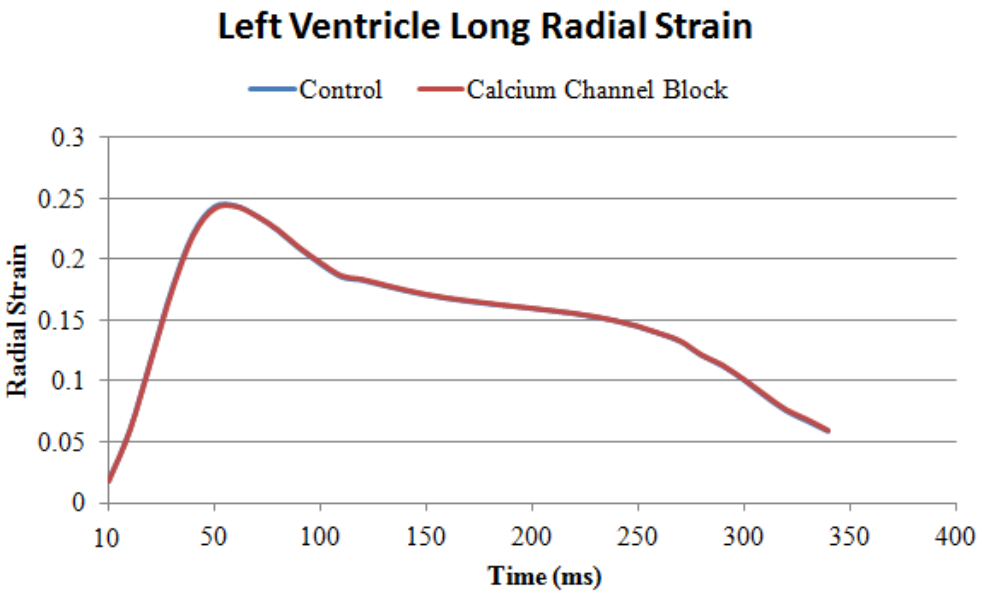

Figure 79: Left Ventricle strain in the long direction for control and Ca^{2+} channel blocked model

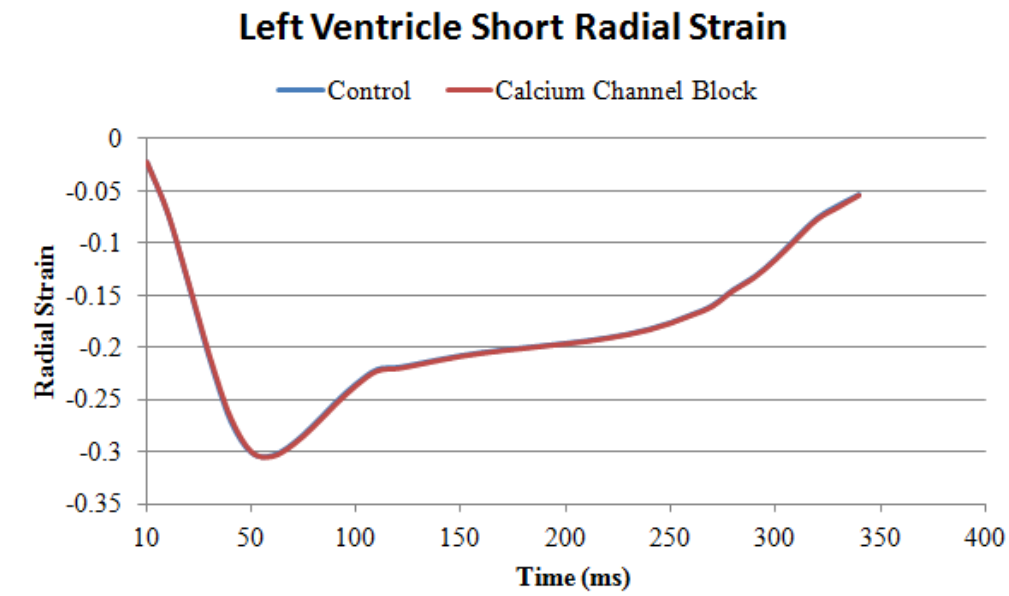

Figure 80: Left Ventricle strain in the short direction for control and Ca^{2+} channel blocked model

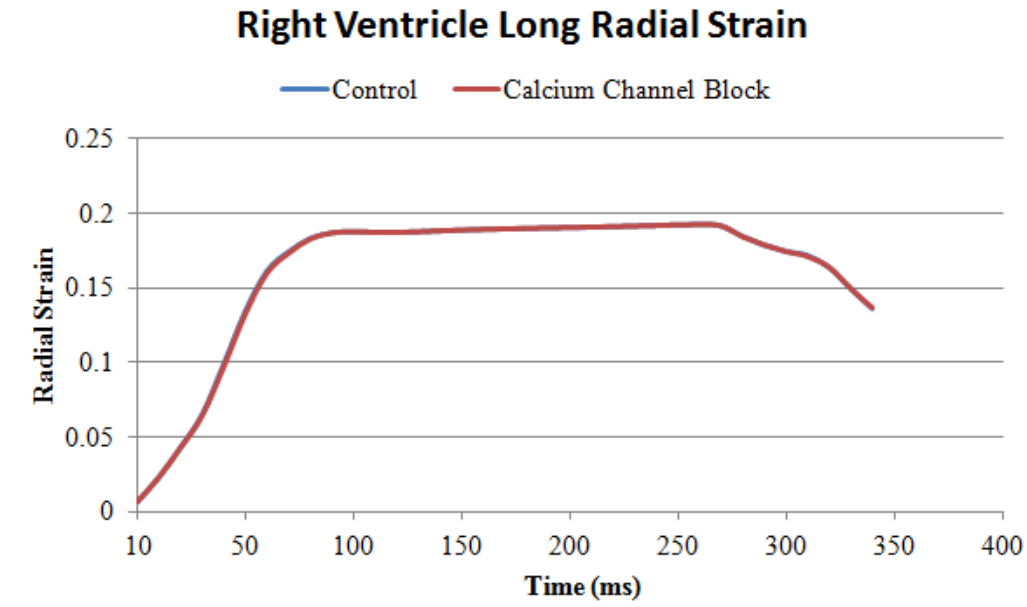

Figure 81: Right Ventricle strain in the long direction for control and Ca^{2+} channel blocked model

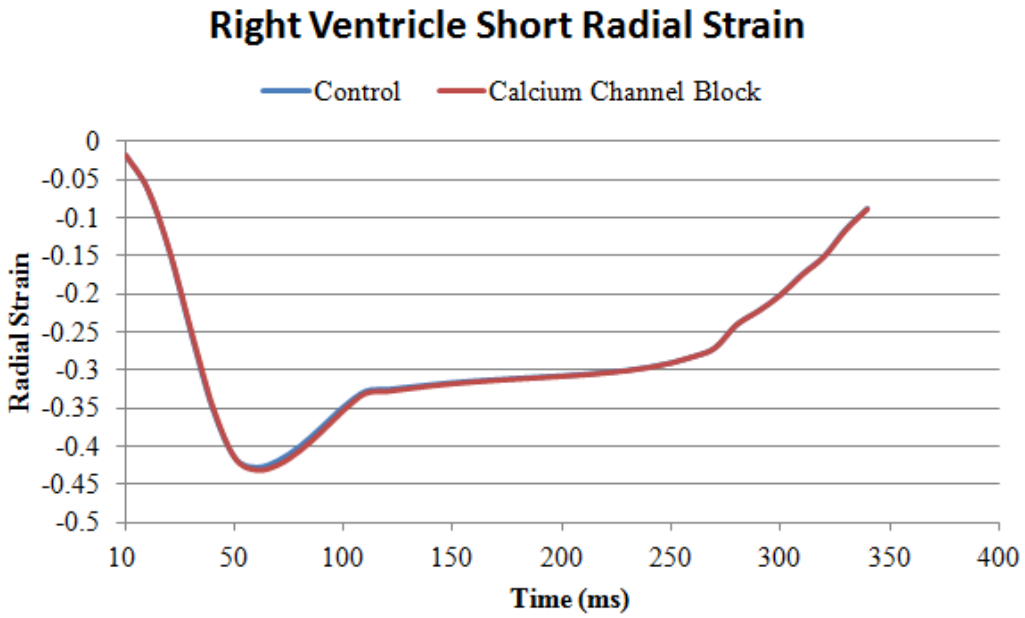

Figure 82: Right Ventricle strain in the short direction for control and Ca^{2+} channel blocked model

L-type calcium channel blockers are known in literature to reduce the QT-interval and the action potential duration due to early repolarization.[42,99] The calcium dynamics are also known to be the direct link between the electrophysiology and the mechanical contractile behavior of the cardiac tissue.[60] Therefore, our expectation by applying an IC_{50} value of a calcium channel blocker was to predict a disturbance in the mechanics of the whole cycle compared to the control. That, however, was not the case as seen in the results of the tissue deformation biomarkers. The results were all similar to the control. The IC_{50} value of a calcium channel blocker was enough to cause electrophysiological changes; however, it could be that the mechanics is not sensitive enough to detect these changes, so that a greater channel inhibition needs to be tested for mechanical disturbances to appear. It is also thought that one cardiac cycle is not sufficient to affect the deformation abnormalities, so that modeling more than one cycle could be needed to access the effect of calcium channel blockage on the mechanical behavior. Thus, our predictions on calcium blockage will need to be elaborated in future work.

4) Conclusion

The objectives of this study were to model accurately a single ventricular contraction-relaxation cycle and monitor the effect induced by nanodrugs on LV and RV electro-mechano-physiology. The objectives of this study were thus achieved. The nanodrugs causing sodium channel blockage were found to produce the expected delays, and predicted additionally other effects on LV twisting and ventricular strain. The nanodrugs causing potassium and calcium channel blockage showed that the mechanics does not respond as quickly to the electrophysiology as does the electrophysiology to ionic changes. Nonetheless, it is possible for small deviations from the normal to accumulate over multiple cardiac cycles, and lead to adverse consequences on cardiac health in the long term. As such, multi-cycle investigations of K^+ and Ca^{2+} effects on cardiac electro-mechanics are recommended for future work.

Chaste was chosen as the software to build our model on, as it offers an open source multiphysics framework to build the coupled (drug-electro-mechano-physiological) system.

Two material laws for modeling passive material stress were already in place on Chaste; however, new reports in literature suggested that the orthotropic Holzapfel and Ogden material law was better suited than the isotropic (Mooney-Rivlin) or the transversely isotropic hyperelastic model (Pole-Zero) available in Chaste. The Holzapfel and Odgen material law was thus developed for implicit finite element implementation, incorporated on Chaste, and used to solve the coupled multiphysics model. To check the validity of the material law, it was compared to the transverse isotropic Pole-Zero law. To validate the importance of fiber orientation definition in mechanical modeling, the Holzapfel and Odgen model was also compared to the isotropic Mooney-Rivlin model.

All three models solved 90% of the target cardiac cycle, before meeting mesh instabilities. The results showed not only that the Holzapfel and Ogden model was less stiff than both the Pole-Zero model and the Mooney-Rivlin model, but that even when using the material law as transversely isotropic (confining it to four parameters only, and not using its full orthotropic capability), it showed better mechanical performance in terms of ventricular volume reduction, ejection fraction, left

ventricular twisting, and longitudinal shortening. These are all key mechanical biomarkers where the Holzapfel and Ogden model outperforms its competitors pre-programmed on Chaste.

Encouraged by the mechanical predictions of the Holzapfel and Ogden model, three nanodrug effects were then investigated in the coupled multiphysics framework, in the form of the IC_{50} value of a sodium channel blocker (such as silver nanoparticles), a 100 μM dose of ultrasmall gold nanoparticle drug carriers and the IC_{50} value of a calcium channel blocker (such as ZnO nanoparticles). The electrophysiological predictions were found to be consistent with the information published in literature. For the mechanics, the delay in the electrical activation caused by the sodium channel blocker was translated into a delay in all the mechanical biomarkers of the ventricles, as expected. Further interesting predictions were made, which require further study; they are the increased LV twist angle and the increased stretching and shortening of the ventricles in the radial directions as a result of sodium channel blockage.

For the potassium channel blocking effect the results turned out, predictably, the same as for the control, since the electrical activation and hence the contraction are not affected by potassium channel blockage. Unfortunately, modeling only 90% of the cycle was thus not enough to reveal how ventricular relaxation would be affected, since the effects were only starting to appear as the simulation terminated.

As for the calcium channel blocker, the IC_{50} value was enough to cause electrophysiological changes from the control, however, these changes were not translated to the tissue mechanics. It might be that the mechanics are not sensitive enough to detect these changes, so a larger channel inhibition needs to be tested for mechanical disturbances to appear, or one cardiac cycle is just not sufficient to affect the deformation abnormalities and modeling more cycles will be required to access the effect of calcium channel blockage on the mechanical behavior.

For the future work of this study more information is needed to understand the unexpected mechanical behavior of the sodium channel blocked model and the calcium channel blocked model and to acquire more conclusive results about the potassium channel blocked model. The first step would be to fix the mesh stability of the models on Chaste, e.g. using compressible models with a large bulk modulus to

mimic incompressible behavior less restrictively, to enable the completion of the first cardiac cycle and to open the possibility of modeling more than one cycle.

Another issue that might be affecting the sensitivity of the model to the nanodrug effects is that the mechanical response is not fed back to the electrophysiology. This feedback effect was not accounted for in this work since, on Chaste, it is very computationally expensive to apply on big meshes such as the one used here. Nonetheless, this two-way coupling is crucial and needs to be tested since even small changes in the mechanics could amplify electrical changes which in turn would amplify changes in the mechanics.

Improvement to EF can be made in the LV and RV simulation if we revise the boundary conditions. Fixing the apex and leaving the base free is the opposite of the natural order of things. At the moment these boundary conditions are the most stable. It is a good compromise since the ventricles are still able to contract and twist, however, the lack of atria in the model leave the base completely free to spread as the muscles contract downwards as shown in Figure 83 and as evidenced from the radial strain results.

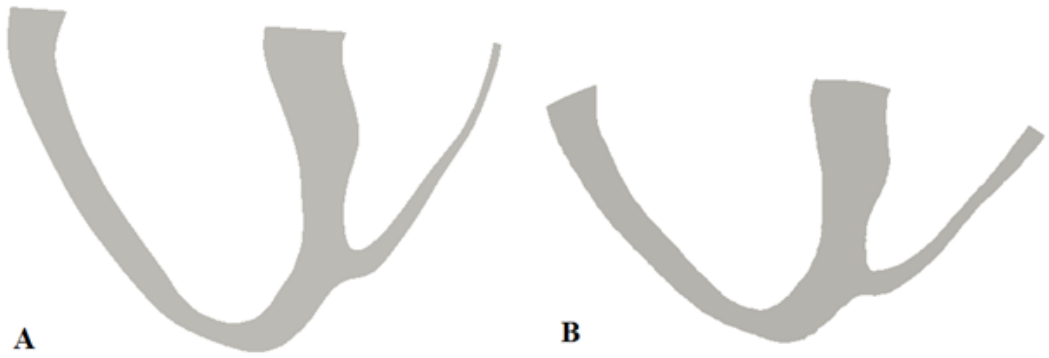

Figure 83: Longitudinal slice through the ventricles A) in diastole and B) in systole

The trick lies in finding boundary conditions that simulate the effect of atrial attachment to the base without increasing its stiffness. Sliding wall boundary conditions are currently being tested where the boundary nodes can be fixed in one or two directions and left to slide freely in the third, but it is facing graver stability issues. Since, Dirichlet boundary conditions are not the best option for biological soft tissue, Robin-like boundary conditions, where a spring-like and viscous effect is

applied at the desired surface, are also being investigated. Improving the boundary conditions is expected to primarily achieve significant improvements to the mechanical performance of the model in terms of ventricular volume reduction and ejection fraction, and further contribute to model stability to simulate multiple cardiac cycles.

Another problem that might be compromising the stability, is the selected mechanics solver time step. The problem was set to solve the mechanics every 10 ms as solving the mechanics problem for such a large mesh is computationally very expensive. The idea provided a significant speed-up, but seemed to experience difficulty near the end of the simulation, which eventually crashed. If the muscles are relaxing too quickly during repolarization, the mechanical changes in each time step might be too great for such a spaced out time-stepping scheme.

From the perspective of drugs, combining nanodrug effects is an important phenomenon to look into since some nanocomposites could contain more than one ion channel inhibiting component or even a single nanoparticle such as CuO mentioned in the introduction could be associated with both sodium and potassium channel blocking.

With the quick advances taking place in the field of nanomedicine and the excitement of the potential it holds, the side effects need to be considered and monitored. Computational models are an inexpensive way of doing that. Therefore, the more the data and information that can be obtained from the drug testing models, the more accurate and reliable they can become and the more widely used they will be. This could significantly reduce the need for animal testing and reduce the time and cost it takes to release a much-needed cure for a disease.

References

1. Iaizzo PA. Handbook of cardiac anatomy, physiology, and devices: Second edition. *Handb Card Anatomy, Physiol Devices Second Ed*. 2005:1-659. doi:10.1007/978-1-60327-372-5.
2. Grant AO. Cardiac ion channels. *Circ Arrhythmia Electrophysiol*. 2009;2(2):185-194. doi:10.1161/CIRCEP.108.789081.
3. Brennan T, Fink M, Rodriguez B. Multiscale modelling of drug-induced effects on cardiac electrophysiological activity. *Eur J Pharm Sci*. 2009;36(1):62-77. doi:10.1016/j.ejps.2008.09.013.
4. Oberdörster G. Safety assessment for nanotechnology and nanomedicine: Concepts of nanotoxicology. *J Intern Med*. 2010;267(1):89-105. doi:10.1111/j.1365-2796.2009.02187.x.
5. Duncan R, Gaspar R. Nanomedicine(s) under the microscope. *Mol Pharm*. 2011;8(6):2101-2141. doi:10.1021/mp200394t.
6. Ali I, Rahis-Uddin, Salim K, Rather M a, Wani W a, Haque A. Advances in nano drugs for cancer chemotherapy. *Curr Cancer Drug Targets*. 2011;11(2):135-146. doi:10.2174/156800911794328493.
7. Pan Y, Leifert A, Graf M, et al. High-sensitivity real-time analysis of nanoparticle toxicity in green fluorescent protein-expressing zebrafish. *Small*. 2013;9(6):863-869. doi:10.1002/smll.201201173.
8. Piccini JP, Whellan DJ, Berridge BR, et al. Current challenges in the evaluation of cardiac safety during drug development: Translational medicine meets the Critical Path Initiative. *Am Heart J*. 2009;158(3):317-326. doi:10.1016/j.ahj.2009.06.007.
9. Raschi E, Vasina V, Ursino MG, Boriani G, Martoni A, de Ponti F. Anticancer drugs and cardiotoxicity: Insights and perspectives in the era of targeted therapy. *Pharmacol Ther*. 2010;125(2):196-218. doi:10.1016/j.pharmthera.2009.10.002.
10. Leifert A, Pan Y, Kinkeldey A, et al. Differential hERG ion channel activity of ultrasmall gold nanoparticles. *Proc Natl Acad Sci U S A*. 2013;110(20):8004-8009. doi:10.1073/pnas.1220143110.
11. Sarazan RD, Mittelstadt S, Guth B, Koerner J, Zhang J, Pettit S. Cardiovascular function in nonclinical drug safety assessment: current issues and opportunities. *Int J Toxicol*. 2011;30(3):272-286. doi:10.1177/1091581811398963.
12. Zeng S, Yong K-T, Roy I, Dinh X-Q, Yu X, Luan F. A Review on Functionalized Gold Nanoparticles for Biosensing Applications. *Plasmonics*.

2011;6(3):491-506. doi:10.1007/s11468-011-9228-1.

13. Huo S, Jin S, Ma X, et al. Ultrasmall gold nanoparticles as carriers for nucleus-based gene therapy due to size-dependent nuclear entry. *ACS Nano*. 2014;8(6):5852-5862. doi:10.1021/nn5008572.

14. Ghosh P, Han G, De M, Kim CK, Rotello VM. Gold nanoparticles in delivery applications. *Adv Drug Deliv Rev*. 2008;60(11):1307-1315. doi:10.1016/j.addr.2008.03.016.

15. Kapse-Mistry S, Govender T, Srivastava R, Yergeri M. Nanodrug delivery in reversing multidrug resistance in cancer cells. *Front Pharmacol*. 2014;5 JUL(July):1-22. doi:10.3389/fphar.2014.00159.

16. Huang K, Ma H, Liu J, et al. Size-dependent localization and penetration of ultrasmall gold nanoparticles in cancer cells, multicellular spheroids, and tumors in vivo. *ACS Nano*. 2012;6(5):4483-4493. doi:10.1021/nn301282m.

17. Pan Y, Leifert A, Ruau D, et al. Gold nanoparticles of diameter 1.4 nm trigger necrosis by oxidative stress and mitochondrial damage. *Small*. 2009;5(18):2067-2076. doi:10.1002/smll.200900466.

18. Liu Z, Ren G, Zhang T, Yang Z. Action potential changes associated with the inhibitory effects on voltage-gated sodium current of hippocampal CA1 neurons by silver nanoparticles. *Toxicology*. 2009;264(3):179-184. doi:10.1016/j.tox.2009.08.005.

19. Tang M, Xing T, Zeng J, et al. Unmodified CdSe Quantum Dots Induce Elevation of Cytoplasmic Calcium Levels and Impairment of Functional Properties of Sodium Channels in Rat Primary Cultured Hippocampal Neurons. *Environ Health Perspect*. 2008;116(7):915-922. doi:10.1289/ehp.11225.

20. Jakubek LM, Marangoudakis S, Raingo J, Liu X, Lipscombe D, Hurt RH. The inhibition of neuronal calcium ion channels by trace levels of yttrium released from carbon nanotubes. *Biomaterials*. 2009;30(31):6351-6357. doi:10.1016/j.biomaterials.2009.08.009

21. Wang H-J, Growcock AC, Tang T, O'Hara J, Huang Y, Aronstam RS. Zinc oxide nanoparticle disruption of store-operated calcium entry in a muscarinic receptor signaling pathway. *Toxicol In Vitro*. 2010;24(7):1953-1961. doi:10.1016/j.tiv.2010.08.005.

22. Xu L-J, Zhao J-X, Zhang T, Ren G-G, Yang Z. In vitro study on influence of nano particles of CuO on CA1 pyramidal neurons of rat hippocampus potassium currents. *Environ Toxicol*. 2009;24(3):211-217. doi:10.1002/tox.20418.

23. Liu Z, Liu S, Ren G, Zhang T, Yang Z. Nano-CuO inhibited voltage-gated sodium current of hippocampal CA1 neurons via reactive oxygen species but

independent from G-proteins pathway. *J Appl Toxicol*. 2011;31(5):439-445. doi:10.1002/jat.1611.

24. Kumar SA, Chen S. Nanostructured Zinc Oxide Particles in Chemically Modified Electrodes for Biosensor Applications. *Anal Lett*. 2008;41(December 2013):141-158. doi:10.1080/00032710701792612.

25. Zhao J, Xu L, Zhang T, Ren G, Yang Z. Influences of nanoparticle zinc oxide on acutely isolated rat hippocampal CA3 pyramidal neurons. *Neurotoxicology*. 2009;30(2):220-230. doi:10.1016/j.neuro.2008.12.005.

26. Zemzemi N, Bernabeu MO, Saiz J, et al. Computational assessment of drug-induced effects on the electrocardiogram: From ion channel to body surface potentials. *Br J Pharmacol*. 2013;168(3):718-733. doi:10.1111/j.1476-5381.2012.02200.x.

27. Holbrook M, Malik M, Shah RR, Valentin JP. Drug induced shortening of the QT/QTc interval: An emerging safety issue warranting further modelling and evaluation in drug research and development? *J Pharmacol Toxicol Methods*. 2009;59(1):21-28. doi:10.1016/j.vascn.2008.09.001.

28. Collins T a, Bergenholm L, Abdulla T, et al. Modeling and Simulation Approaches for Cardiovascular Function and Their Role in Safety Assessment. 2015;(September 2014):1-14. doi:10.1002/psp4.18.

29. Xu YQ, Pickoff a S, Clarkson CW. Evidence for developmental changes in sodium channel inactivation gating and sodium channel block by phenytoin in rat cardiac myocytes. *Circ Res*. 1991;69(3):644-656. doi:10.1161/01.RES.69.3.644.

30. Ranjan AP, Mukerjee A, Helson L, Vishwanatha JK. Mitigating prolonged QT interval in cancer nanodrug development for accelerated clinical translation. *J Nanobiotechnology*. 2013;11:40. doi:10.1186/1477-3155-11-40.

31. Obiol-pardo C, Gomis-tena J, Sanz F, Saiz J, Pastor M. A Multiscale Simulation System for the Prediction of Drug-Induced Cardiotoxicity. 2011:483-492.

32. O'Hara T, Rudy Y. Quantitative comparison of cardiac ventricular myocyte electrophysiology and response to drugs in human and nonhuman species. *AJP Hear Circ Physiol*. 2012;302(5):H1023-H1030. doi:10.1152/ajpheart.00785.2011.

33. Trayanova N a, Constantino J, Gurev V. Electromechanical models of the ventricles. *Am J Physiol Heart Circ Physiol*. 2011;301(2):H279-H286. doi:10.1152/ajpheart.00324.2011.

34. Sanhai WR, Sakamoto JH, Canady R, Ferrari M. Seven challenges for nanomedicine. *Nat Nanotechnol*. 2008;3(5):242-244. doi:10.1038/nnano.2008.114.

35. ten Tusscher KHWJ, Noble D, Noble PJ, Panfilov a V. A model for human ventricular tissue. *Am J Physiol Heart Circ Physiol*. 2004;286(4):H1573-H1589. doi:10.1152/ajpheart.00794.2003.

36. Grandi E, Pasqualini FS, Bers DM. A novel computational model of the human ventricular action potential and Ca transient. *J Mol Cell Cardiol*. 2010;48(1):112-121. doi:10.1016/j.yjmcc.2009.09.019.

37. Luo CH, Rudy Y. A model of the ventricular cardiac action potential. Depolarization, repolarization, and their interaction. *Circ Res*. 1991;68(6):1501-1526. doi:10.1161/01.RES.68.6.1501.

38. Corrias A, Giles W, Rodriguez B. Ionic mechanisms of electrophysiological properties and repolarization abnormalities in rabbit Purkinje fibers. 2011:1806-1813. doi:10.1152/ajpheart.01170.2010.

39. Zemzemi N, Rodriguez JS, Rodriguez B, Sud-ouest IB, Valencia UP De. Role of L-type Calcium in Modulating Pro-Arrhythmic Effects of Dofetilide in Humans. :1-4.

40. Glinka A, Polak S. The effects of six antipsychotic agents on QTc-An attempt to mimic clinical trial through simulation including variability in the population. *Comput Biol Med*. 2014;47(1):20-26. doi:10.1016/j.compbiomed.2014.01.010.

41. Mishra H, Polak S, Jamei M, Rostami-Hodjegan a. Interaction Between Domperidone and Ketoconazole: Toward Prediction of Consequent QTc Prolongation Using Purely In Vitro Information. *CPT pharmacometrics Syst Pharmacol*. 2014;3(August):e130. doi:10.1038/psp.2014.26.

42. Zemzemi N, Rodriguez B. Effects of L-type calcium channel and human ether-a-go-go related gene blockers on the electrical activity of the human heart: a simulation study. *Europace*. 2014;17(2):326-333. doi:10.1093/europace/euu122.

43. Wilhelms M, Rombach C, Scholz EP, Dossel O, Seemann G. Impact of amiodarone and cisapride on simulated human ventricular electrophysiology and electrocardiograms. *Europace*. 2012;14(suppl 5):v90-v96. doi:10.1093/europace/eus281.

44. Zemzemi N, Bernabeu MO, Saiz J, Rodriguez B. Simulating drug-induced effects on the heart: From ion channel to body surface electrocardiogram. *Lect Notes Comput Sci (including Subser Lect Notes Artif Intell Lect Notes Bioinformatics)*. 2011;6666 LNCS:259-266. doi:10.1007/978-3-642-21028-0_32.

45. Trayanova N a., Rice JJ. Cardiac electromechanical models: From cell to organ. *Front Physiol*. 2011;2 AUG(August):1-19. doi:10.3389/fphys.2011.00043.

46. Evangelista a., Nardinocchi P, Puddu PE, Teresi L, Torromeo C, Varano V. Torsion of the human left ventricle: Experimental analysis and computational modeling. *Prog Biophys Mol Biol*. 2011;107(1):112-121. doi:10.1016/j.pbiomolbio.2011.07.008.

47. Rüssel IK, Götte MJW, Bronzwaer JG, Knaapen P, Paulus WJ, van Rossum AC. Left Ventricular Torsion. An Expanding Role in the Analysis of Myocardial Dysfunction. *JACC Cardiovasc Imaging*. 2009;2(5):648-655. doi:10.1016/j.jcmg.2009.03.001.

48. Bloechlinger S, Grander W, Bryner J, Dünser MW. Left ventricular rotation: A neglected aspect of the cardiac cycle. *Intensive Care Med*. 2011;37(1):156-163. doi:10.1007/s00134-010-2053-8.

49. Palit A, Bhudia SK, Arvanitis TN, Turley G a., Williams M a. Computational modelling of left-ventricular diastolic mechanics: Effect of fibre orientation and right-ventricle topology. *J Biomech*. 2015;48(4):604-612. doi:10.1016/j.jbiomech.2014.12.054.

50. Baillargeon B, Rebelo N, Fox DD, Taylor RL, Kuhl E. The Living Heart Project: A robust and integrative simulator for human heart function. *Eur J Mech A/Solids*. 2014;48:38-47. doi:10.1016/j.euromechsol.2014.04.001.

51. Baillargeon B, Costa I, Leach JR, et al. Human Cardiac Function Simulator for the Optimal Design of a Novel Annuloplasty Ring with a Sub-valvular Element for Correction of Ischemic Mitral Regurgitation. *Cardiovasc Eng Technol*. 2015. doi:10.1007/s13239-015-0216-z.

52. Nash MP, Hunter PJ. Computational Mechanics of the Heart. *J Elast*. 2001;61:113-141. doi:10.1023/A:1011084330767.

53. Holzapfel G a, Ogden RW. Constitutive modelling of passive myocardium: a structurally based framework for material characterization. *Philos Trans A Math Phys Eng Sci*. 2009;367(1902):3445-3475. doi:10.1098/rsta.2009.0091.

54. Kandel, Eric R., James H. Schwartz, and Thomas M. Jessell, eds. Principles of neural science. Vol. 4. New York: McGraw-Hill, 2000.

55. Ionasec R, Voigt I, Mihalef V, et al. Patient-specific modeling of the heart: Applications to cardiovascular disease management. *Lect Notes Comput Sci (including Subser Lect Notes Artif Intell Lect Notes Bioinformatics)*. 2010;6364 LNCS:14-24. doi:10.1007/978-3-642-15835-3_2.

56. Lee LC, Genet M, Dang AB, Ge L, Guccione JM, Ratcliffe MB. Applications of computational modeling in cardiac surgery. *J Card Surg*. 2014;29(3):293-302. doi:10.1111/jocs.12332.

57. Mirams GR, Arthurs CJ, Bernabeu MO, et al. Chaste: An Open Source C++ Library for Computational Physiology and Biology. *PLoS Comput Biol*. 2013;9(3). doi:10.1371/journal.pcbi.1002970.

58. Pathmanathan P, Whiteley JP. A numerical method for cardiac mechanoelectric simulations. *Ann Biomed Eng*. 2009;37(5):860-873. doi:10.1007/s10439-009-9663-8.

59. Pathmanathan P, Bernabeu MO, Niederer SA, Gavaghan DJ, Kay D. Computational modelling of cardiac electrophysiology: explanation of the variability of results from different numerical solvers. *Int j numer method biomed eng*. 2012;28(8):890-903. doi:10.1002/cnm.2467.

60. Pathmanathan P, Chapman SJ, Gavaghan DJ, Whiteley JP. Cardiac electromechanics: The effect of contraction model on the mathematical problem and accuracy of the numerical scheme. *Q J Mech Appl Math*. 2010;63(3):375-399. doi:10.1093/qjmam/hbq014.

61. a.L Hodgkin, a.F. Huxley. A quantitative description of membrane current and its application to conduction and excitation in nerve. J. *J Physiol*. 1952.

62. Priebe L, Beuckelmann DJ. Simulation study of cellular electric properties in heart failure. *CircRes*. 1998;82(0009-7330 SB - M):1206-1223.

63. Sundnes J, Lines G, Cai X, Nielsen B. *Computing the Electrical Activity in the Heart*.; 2007.

64. Bernabeu MO, Southern J, Wilson N, Strazdins P, Cooper J, Pitt-Francis J. Chaste: a case study of parallelisationof an open source finite-elementsolver with applications tocomputational cardiacelectrophysiology simulation. *Int J High Perform Comput Appl*. 2013;28(1):13-32. doi:10.1177/1094342012474997.

65. Heidenreich E a., Ferrero JM, Doblaré M, Rodríguez JF. Adaptive macro finite elements for the numerical solution of monodomain equations in cardiac electrophysiology. *Ann Biomed Eng*. 2010;38(7):2331-2345. doi:10.1007/s10439-010-9997-2.

66. Tusscher KHWJ Ten, Panfilov A V. Cell model for efficient simulation of wave propagation in human ventricular tissue under normal and pathological conditions. 2006;51:6141-6156. doi:10.1088/0031-9155/51/23/014.

67. Richardson ES, Xiao Y. Cardiac Electrophysiology Methods and Models. *Business*. 2010:329-348. doi:10.1007/978-1-4419-6658-2.

68. Cooper JP. Automatic validation and optimisation of biological models. *Computer (Long Beach Calif)*. 2008. http://ora.ouls.ox.ac.uk/objects/uuid:24b96d62-b47c-458d-9dff-79b27dbdc9f2/datastreams/THESIS01.

69. Pitt-Francis J, Pathmanathan P, Bernabeu MO, et al. Chaste: A test-driven approach to software development for biological modelling. *Comput Phys Commun*. 2009;180(12):2452-2471. doi:10.1016/j.cpc.2009.07.019.

70. Colli Franzone P, Pavarino LF, Taccardi B. Simulating patterns of excitation, repolarization and action potential duration with cardiac Bidomain and Monodomain models. *Math Biosci*. 2005;197(1):35-66. doi:10.1016/j.mbs.2005.04.003.

71. Tung L. A bi-domain model for describing ischemic myocardial d-c potentials. 1978. http://dspace.mit.edu/handle/1721.1/16177.

72. Potse M, Dube B, Richer J, Vinet A, Gulrajani RM. A Comparison of Monodomain and Bidomain Reaction-Diffusion Models for Action Potential Propagation in the Human Heart. *IEEE Trans Biomed Eng*. 2006;53(12):2425-2435. doi:10.1109/TBME.2006.880875.

73. Clayton RH, Panfilov a. V. A guide to modelling cardiac electrical activity in anatomically detailed ventricles. *Prog Biophys Mol Biol*. 2008;96(1-3):19-43. doi:10.1016/j.pbiomolbio.2007.07.004.

74. Dirichlet A, Pde C. Chaste : Finite Element Implementations. *Article*. 2011:1-22.

75. Dalen BM Van, Geleijnse ML. Left Ventricular Twist in Cardiomyopathy.

76. Wallman M, Smith NP, Rodriguez B. Computational methods to reduce uncertainty in the estimation of cardiac conduction properties from electroanatomical recordings. *Med Image Anal*. 2014;18(1):228-240. doi:10.1016/j.media.2013.10.006.

77. Sengupta PP, Tajik a. J, Chandrasekaran K, Khandheria BK. Twist Mechanics of the Left Ventricle. Principles and Application. *JACC Cardiovasc Imaging*. 2008;1(3):366-376. doi:10.1016/j.jcmg.2008.02.006.

78. Streeter DD, Spotnitz HM, Patel DP, Ross J, Sonnenblick EH. Fiber orientation in the canine left ventricle during diastole and systole. *Circ Res*. 1969;24(3):339-347. doi:10.1161/01.RES.24.3.339.

79. Lekadir K, Ghafaryasl B, Muñoz-Moreno E, Butakoff C, Hoogendoorn C, Frangi AF. Predictive modeling of cardiac fiber orientation using the knutsson mapping. *Lect Notes Comput Sci (including Subser Lect Notes Artif Intell Lect Notes Bioinformatics)*. 2011;6892 LNCS(PART 2):50-57. doi:10.1007/978-3-642-23629-7_7.

80. Carapella V, Bordas R, Pathmanathan P, et al. Quantitative study of the effect of tissue microstructure on contraction in a computational model of rat left ventricle. *PLoS One*. 2014;9(4):1-13. doi:10.1371/journal.pone.0092792.

81. Rice JJ, De Tombe PP. Approaches to modeling crossbridges and calcium-dependent activation in cardiac muscle. *Prog Biophys Mol Biol*. 2004;85(2-3):179-195. doi:10.1016/j.pbiomolbio.2004.01.011.

82. Kerckhoffs RCP, Bovendeerd PHM, Kotte JCS, Prinzen FW, Smits K, Arts T.

Homogeneity of cardiac contraction despite physiological asynchrony of depolarization: A model study. *Ann Biomed Eng*. 2003;31(5):536-547. doi:10.1114/1.1566447.

83. Rossi S, Ruiz-Baier R, Pavarino LF, Quarteroni A. Orthotropic active strain models for the numerical simulation of cardiac biomechanics. *Int j numer method biomed eng*. 2012;28(6-7):761-788. doi:10.1002/cnm.2473.

84. Göktepe S, Acharya SNS, Wong J, Kuhl E. Computational modeling of passive myocardium. *Int j numer method biomed eng*. 2011;27(1):1-12. doi:10.1002/cnm.1402.

85. Mooney M. A theory of large elastic deformation. *J Appl Phys*. 1940;11(9):582-592. doi:10.1063/1.1712836.

86. Rivlin RS. Large Elastic Deformations of Isotropic Materials . I. Fundamental Concepts. *Philos Trans R Soc London Ser A, Math Phys Sci*. 1948;240(822):459-490.

87. Nash MP, Panfilov A V. Electromechanical model of excitable tissue to study reentrant cardiac arrhythmias. *Prog Biophys Mol Biol*. 2004;85(2-3):501-522. doi:10.1016/j.pbiomolbio.2004.01.016.

88. Bernabeu MO, Wallman M, Rodr B. Shock-Induced Arrhythmogenesis in the Human Heart : a Computational Modelling Study. 2010:760-763.

89. Gartling DK, Dohrmann CR. Quadratic finite elements and incompressible viscous flows. *Comput Methods Appl Mech Eng*. 2006;195(13-16):1692-1708. doi:10.1016/j.cma.2005.05.046.

90. Gima K, Rudy Y. Ionic current basis of electrocardiographic waveforms: A model study. *Circ Res*. 2002;90(8):889-896. doi:10.1161/01.RES.0000016960.61087.86.

91. Dupraz M, Filippi S, Gizzi A, Quarteroni A, Ruiz-Baier R. Finite element and finite volume-element simulation of pseudo-ECGs and cardiac alternans. *Math Methods Appl Sci*. 2015;38(6):1046-1058. doi:10.1002/mma.3127.

92. Kovalova S, Necas J, Vespalec J. What is a “normal” right ventricle? *Eur J Echocardiogr*. 2006;7(4):293-297. doi:10.1016/j.euje.2005.06.010.

93. Eriksson T, Prassl A, Plank G, Holzapfel G. Influence of myocardial fiber/sheet orientations on left ventricular mechanical contraction. *Math Mech Solids*. 2013;18(6):592-606. doi:10.1177/1081286513485779.

94. Kleijn S a., Brouwer WP, Aly MF a, et al. Comparison between three-dimensional speckle-tracking echocardiography and cardiac magnetic resonance imaging for quantification of left ventricular volumes and function. *Eur Heart J Cardiovasc Imaging*. 2012;13(10):834-839. doi:10.1093/ehjci/jes030.

95. Ahmed MI, Desai R V., Gaddam KK, et al. Relation of torsion and myocardial strains to LV ejection fraction in hypertension. *JACC Cardiovasc Imaging*. 2012;5(3):273-281. doi:10.1016/j.jcmg.2011.11.013.

96. Notomi Y, Lysyansky P, Setser RM, et al. Measurement of ventricular torsion by two-dimensional ultrasound speckle tracking imaging. *J Am Coll Cardiol*. 2005;45(12):2034-2041. doi:10.1016/j.jacc.2005.02.082.

97. Harmer A, Valentin J-P, Pollard C. On the relationship between block of the cardiac Na + channel and drug-induced prolongation of the QRS complex. *Br J Pharmacol*. 2011;164(2):260-273. doi:10.1111/j.1476-5381.2011.01415.x.

98. Corrias a, Jie X, Romero L, et al. Arrhythmic risk biomarkers for the assessment of drug cardiotoxicity: from experiments to computer simulations. *Philos Trans A Math Phys Eng Sci*. 2010;368:3001-3025. doi:10.1098/rsta.2010.0083.

99. Wang R-X, Jiang W-P. Changes of action potential and L-type calcium channel current of Sprague-Dawley rat ventricular myocytes by different amlodipine isomers. *Can J Physiol Pharmacol*. 2008;86(9):620-625. doi:10.1139/y08-065.